



Copyright Undertaking

This thesis is protected by copyright, with all rights reserved.

By reading and using the thesis, the reader understands and agrees to the following terms:

1. The reader will abide by the rules and legal ordinances governing copyright regarding the use of the thesis.
2. The reader will use the thesis for the purpose of research or private study only and not for distribution or further reproduction or any other purpose.
3. The reader agrees to indemnify and hold the University harmless from and against any loss, damage, cost, liability or expenses arising from copyright infringement or unauthorized usage.

IMPORTANT

If you have reasons to believe that any materials in this thesis are deemed not suitable to be distributed in this form, or a copyright owner having difficulty with the material being included in our database, please contact lbsys@polyu.edu.hk providing details. The Library will look into your claim and consider taking remedial action upon receipt of the written requests.

**OPTOFLUIDIC CHIPS WITH DIRECTLY
PRINTED POLYMER OPTICAL
WAVEGUIDE SENSORS FOR LABEL-FREE
BIODETECTION**

WANG HAN

PhD

The Hong Kong Polytechnic University

2024

The Hong Kong Polytechnic University
Department of Electrical and Electronic Engineering

**Optofluidic chips with directly printed polymer
optical waveguide sensors for label-free
biodection**

WANG Han

*A thesis submitted in partial fulfilment of the requirements for
the degree of Doctor of Philosophy*

July 2024

CERTIFICATE OF ORIGINALITY

I hereby declare that this thesis is my own work and that, to the best of my knowledge and belief, it reproduces no material previously published or written, nor material that has been accepted for the award of any other degree or diploma, except where due acknowledgement has been made in the text.

_____ (Signed)

WANG Han _____ (Name of student)

Table of contents

Abstract	I
List of publications	V
Acknowledgements	VI
List of figures	VIII
List of acronyms	XV
Chapter 1. Introduction	1
1.1 Background.....	1
1.2 Motivation and objectives of the research.....	3
1.3 Outline of the thesis.....	4
Chapter 2. Overview of optofluidic chip technologies based on optical waveguide sensors	6
2.1 Introduction.....	6
2.2 Optofluidic chip technologies.....	6
2.3 Optical waveguide sensors for optofluidic chips.....	10
2.3.1 Optical waveguide Mach-Zehnder interferometer (MZI) sensors.....	12
2.3.2 Optical waveguide micro-ring resonator (MRR) sensors...	16
2.4 Fabrication technologies for optical waveguide.....	19
2.4.1 Typical fabrication techniques.....	19
2.4.2 DMD-based Maskless lithography technology.....	23
2.5 Summery.....	27

Chapter 3. Fabrication of polymer optical waveguides by digital ultraviolet lithography28

3.1 Introduction..... 28

3.2 Design of single-mode SU-8 optical waveguides..... 30

3.3 Fabrication and optimization of the designed SU-8 optical waveguides..... 32

3.4 Optimization of the fabricated SU-8 optical waveguides..... 34

 3.4.1 Proximity effect compensation..... 35

 3.4.2 Seamless stitching..... 38

3.5 Characterization of the fabricated SU-8 optical waveguides..... 41

 3.5.1 Bending loss measurement..... 41

 3.5.2 Propagation loss measurement..... 44

3.6 Characterization of MMI, Y-Branch Splitter and MRR..... 46

3.7 Summary 50

Chapter 4. Optofluidic chip with directly printed polymer optical waveguide Mach-Zehnder interferometer sensors52

4.1 Introduction..... 52

4.2 Fabrication of SU-8 optical waveguide and optofluidic chip..... 56

 4.2.1 Fabrication of SU-8 optical waveguide Mach-Zehnder interferometer sensors 56

 4.2.2 Fabrication of optofluidic chip by packaging the waveguide chip with microfluidic layer 63

4.3 Testing and characterization of the fabricated SU-8 waveguide and optofluidic chip	66
4.3.1 Transmission spectra of the fabricated MZI microsensors .	67
4.3.2 Measurement of the bulk sensitivity of the fabricated MZI sensors	74
4.4 Testing of the fabricated optofluidic chip in the detection of human Immunoglobulin G	76
4.5 Reusability Testing	78
4.6 Summary	80
Chapter 5. Optofluidic chip with high-Q polymer waveguide microring resonator sensors	81
5.1 Introduction	81
5.2 Design of high-Q ring sensors	83
5.3 Fabrication of SU-8 waveguide MRR sensor and optofluidic chip	86
5.3.1 Fabrication of SU-8 waveguide MRR sensors	86
5.3.2 Fabrication of the SU-8 MRR sensor integrated optofluidic chip	88
5.4 Testing and characterization of the fabricated SU-8 waveguide MRR sensor and optofluidic chip	89
5.4.1 Transmission spectra of the fabricated MRR sensors	89

5.4.2 Transmission spectra of the SU-8 waveguide MRRs with different loss and coupling coefficients.....	91
5.4.3 Testing of the bulky sensitivity of the fabricated SU-8 waveguide MRR sensors.....	92
<p>Glucose solutions of different concentrations were used to evaluate the bulk sensitivity of the manufactured MRR sensors. Injecting glucose solution into or out of the microfluidic channels is done with a motorized syringe pump. As the concentration of glucose increases, the observed wavelength moves to a longer wavelength, as seen in Fig. 5.8(a). The MRR sensors' wavelength shift on the external refractive indices is presented in Fig. 5.8(b). It reveals that the refractive index of the fabricated waveguide MRR sensor is about 22.55 nm/RIU, which is close to the numerical simulation value, i.e., 30.73 nm/RIU.</p>	
5.5 Summary.....	93
Chapter 6. Summary and outlook for future works.....	96
6.1 Summary.....	96
6.2 Future outlook.....	97
Reference.....	100

Abstract

Optofluidic chips fusing photonic and microfluidic technologies have attracted remarkable attention due to their tremendous promise in the development of small-size high-performance biochips for biomedical detection and diagnostics. The progress of affordable diagnostic tools for everyday testing and extensive applications is impeded by the intricate fabrication procedures and restricted functionalization flexibility inherent in conventional silicon-based photonic chips. In this thesis, optofluidic chips based on directly printed polymer optical waveguide sensors, including Mach-Zehnder interferometer (MZI) waveguide sensors and micro-ring resonator (MRR) waveguide sensors, are developed, and their performances in label-free detection have been numerically and experimentally investigated.

A new fabrication process for SU-8 optical waveguides was developed by using an in-house digital ultraviolet lithography (DUL) system. Compared to the photomask-based lithography technologies, DUL can save the cost for the fabrication of photomasks and shorten the lead time. On the other hand, it has the advantage of higher throughput over conventional electronic beam lithography (EBL) and direct laser writing (DLW) technologies. Some typical problems in digital lithography, such as proximity effect and stitching

error, have been well compensated through the numerical pretreatment of pattern data and process optimization.

Experimental results showed that at a wavelength of 1550 nm, the propagation loss of the manufactured straight waveguide is measured to be 0.238 dB/mm. The bending loss is below 0.1 dB/90°-arc if the bending radius is greater than 100 μm . Moreover, multi-mode interferometer (MMI) and Y-branch power splitters were experimentally fabricated to uniformly split the input power across a broad spectral range, spanning from 1500 nm to 1600 nm.

With the own-established waveguide fabrication processes, an integrated optofluidic biochip with directly printed polymer optical waveguide MZI sensors has been developed. An asymmetric MZI sensor embedded with width-tailored waveguide was designed and fabricated for high-sensitivity label-free biodetection. In order to get a high-contrast interference at the output, a specifically constructed Y splitter has been designed to compensate for the light propagation loss in the sensor arm and make the light powers from the two arms suitably balanced. After coming with the transmission spectra of the MZI sensors before and after fabrication of Ormoclاد cladding, it was verified that such a special designed MZI sensor can greatly enhance the extinction ratio (ER) of output spectrum to reach 13.48 dB when the sensor was finally packaged and immersed under water.

After precise printing of an Ormoclad layer via an overlay exposure process and vertical integration with a microfluidic layer, an integrated optofluidic chip was fabricated for on-chip label-free biodetection applications. The on-chip integrated MZI sensor devices exhibited a remarkable high bulk refractive index sensitivity, i.e., 1695.95 nm/RIU. The demonstration of optofluidic chip's ability to detect disease biomarkers was conducted by quantifying the concentration of Human immunoglobulin G (HIgG). HIgG, a main antibody present in both blood and extracellular fluids, acts as a vital defense mechanism against bacterial and viral infections within the human body. After being functionalized with capture molecules, these MZI biosensors were capable of detecting HIgG analytes down to a low concentration of 1.78 pM, which is far beyond the performance of current commercial ELISA tests.

Moreover, an optofluidic chip integrated with directly printed polymer optical waveguide MRR sensors has also been demonstrated. An all-pass MRR sensor that embedded with a width-tailored waveguide was designed and directly printed by using our own-built digital UV lithography processes. The Q factor of the fabricated MRR sensor is as high as 8604. An optofluidic chip has been fabricated, by vertically integrating the MRR sensors with a microfluidic layer, for on-chip label-free biodetection. Results showed that the bulk sensitivity of on-chip integrated MRR sensors is 22.55 nm/RIU. Considering that such MRR has a very narrow transmissive spectral dip (i.e.,

very high spectral resolution) because of high Q factor, it is believed that such an integrated optofluidic chips is also very promising for high-sensitivity biochemical applications, such as nucleic acid or virus testing.

The incorporation of polymer optical waveguide biosensors in these optofluidic chips presents a range of advantages, such as miniaturization, cost-effectiveness, heightened sensitivity, and simplified functionalization. As a result, this breakthrough has the potential to revolutionize the development of compact devices and instrumentation for point-of-care testing and diagnostics.

List of publications

1. Ding, Z.[†], **Wang, H.**[†], Li, T., Ouyang, X., Shi, Y., & Zhang, A. P. (2022). Fabrication of polymer optical waveguides by digital ultraviolet lithography. *Journal of Lightwave Technology*, 40(1), 163-169. ([†]**Co-first Author**)
2. Zhang, Y., Wu, H., **Wang, H.**, Yin, B., Wong, S. H. D., Zhang, A. P., & Tam, H. Y. (2022). Ultraminiature optical fiber-tip directly-printed plasmonic biosensors for label-free biodetection. *Biosensors and Bioelectronics*, 218, 114761.
3. **Wang, H.**, Chen, Z., Li, T., Shi, Y., & Zhang, A. P. (2023). Fabrication of polymer optical waveguide-based Mach-Zehnder interferometer microsensors for integrated optofluidic biodetection, *Optica Sensing Congress 2023*, ID: STu3C.4, Munich, Germany, Aug. 2023.
4. **Wang, H.**, Chen, Z., Li, T., Xie, H., Yin, B., Wong, S. H. D., Shi, Y. & Zhang, A. P. (2024). Optofluidic chip with directly printed polymer optical waveguide Mach-Zehnder interferometer sensors for label-free biodetection. *Biomedical Optics Express*, 15(5), 3240-3250. (highlighted as an **Editor's Pick**)
5. Xie, H. M., Zhang, Y. X., **Wang, H.**, Zhang, A. P., (2024). Lithography-assisted assembly of single-layer gold nanoparticle micropatterns for plasmonic biosensor applications, *IEEE Biosensors 2024*, ID: A02-007, Cambridge, UK, July 29-30, 2024.
6. Chen, Z., **Wang, H.**, Zhang, A. P., Dai, D., Shi, Y. (2024). Ultra-high sensitivity integrated photonic biosensors based on a feedback-coupled microring resonator. (under review)

Acknowledgements

First of all, I would like to express my deepest gratitude to my chief supervisor, Prof. A. Ping Zhang. Under his patient and caring guidance, I have grown from a student with no research experience into a capable scientific researcher. Prof. Zhang has provided me invaluable mentorship in every step of research - from literature review, designing experiments, to polishing written work. He has not only taught me research skills, but also instilled in me the right mindset and attitude for tackling challenges with diligence and passion. I am grateful for his unwavering support, which has been instrumental to my academic success. The knowledge and insights he had imparted will continue to guide me throughout my future life.

I also would like to thank Prof. Siu Hong Dexter Wong, my co-supervisor, for offering lot of help in sensor's biodetection. He is a young and talented scientific researcher who has already achieved impressive accomplishments in his field. I am impressed by his passion and enthusiasm for research which will influence me in the future.

I would like to thank Prof. Bohan Yin who helped me with the sensor regeneration. I am very grateful to Dr. Yangxi Zhang, Dr. Bin Zhou, Dr. Kummara Venkata Krishnaiah, Dr. Mohsin Raza, Dr. Zuoqin Ding, Dr. Jinhui Wang, Dr. Yisheng Gao, Dr. Xia Ouyang, Mr. Shengzeng Huo, Mr. Taige Li, Mr. Zhituo Chen, Mr. Hao Wu, Mr. Nan Wang, Mr. Nannan Zhou, Miss

Huimin Xie, Mr. Zhizheng Wang, Mr. Peng Wang, Mr. Shangming Liu for their help and useful discussions on my experiments.

Finally, I want to express my gratitude to my parents and my friends for their unwavering care and unconditional support. This thesis is dedicated to them to express my deepest love and gratitude!

List of figures

Figure 2.1 Optofluidic chips developed for different applications: (a) Drug development & disease modelling [15], (b) Point-of-care (POC) testing [16], (c) Imaging resolution enhancement in microscope [17], (d) Cell operation and analysis [18], (e) Environmental monitoring [19]..... 7

Figure 2.2 Optofluidic chips based on optical waveguides. (a) A silicon photonic MZI biosensor array integrated with microchannel. (b) Three-dimensional MZI sensor integrated microfluidic chip. (c) An MZI sensor-based point-of-care system. (d) A microring resonator-based optofluidic chip. (e) An optical microring resonator with on-chip microfluidic tuning. (f) An optofluidic chip consisting of arrayed optical slot-waveguide ring resonators.....9

Figure 2.3 Different types of optical waveguide sensors. (a) Planar waveguide sensor [9], (b) spiral waveguide sensor [31], (c) Y splitter sensor [32], (d) microring resonator sensor [33], (e) Mach-Zehnder interferometer (MZI) sensor [33], (f) grating waveguide sensor [34]..... 11

Figure 2.4 Basic structure of an optical waveguide MZI sensor. (a) Asymmetric MZI waveguide sensor. (b) Typical transmission spectrum of an MZI sensor..... 13

Figure 2.5 Two basic configurations of MRR: (a) All pass ring resonator; (b) Add-drop ring resonator. (c) The transmission spectrum of the first

configuration is a spectrum of periodic notch resonances. (d) The spectrum from the drop port of the second configuration is a complementary shape of the spectrum of throughput port. 17

Figure 2.6 Typical fabrication technologies: (a) optical lithography [42], (b) e-beam lithography [43], (c) direct laser writing [41]. 20

Figure 2.7 Flow chart of typical optical lithography processes [41]. 21

Figure 2.8 (a) Schematic diagram of dynamic optical projection stereolithography (DOPsL) [53]. (b) Two DMD pixels tilted into “ON” and “OFF” state respectively [52]. 25

Figure 3.1 (a) Cross-section structure of SU-8 optical waveguide. (b) Calculated electrical field distributions of TE_{11} and TM_{11} modes of the presented waveguides. 32

Figure 3.2 (a) Diagrammatic representation of the DUL system. (b) Grayscale bitmap depicting the engineered patterns functioning as a digital photomask. (c) Schematic illustration of waveguide structures with end-face termination. 34

Figure 3.3 (a) The line pattern with an initial width of 8 pixels before (i) and after (ii) being corrected using a Gaussian-like light pixel distribution. (b) SEM images of the fabricated waveguide with pattern of 2.4- μm wide line. (c) A 9-pixel wide line pattern with half-maximum grey edge before (i) and after (ii) corrected with Gaussian-like light pixel distribution. (d) SEM

images of the fabricated 2.4- μm wide line waveguide. (e) SEM images of the fabricated 45-degree angle patterns using different FWHM values. 37

Figure 3.4 (a) Grayscale distribution maps of the stitching transition zones between two patterns when their compensation coefficients are positive. (b) Grayscale distribution maps of the stitching transition zones between two patterns when their compensation coefficients are negative. (c) Transmission spectra of the fabricated waveguides with various compensation coefficients. (d-h) SEM images of the stitching transition zone of the fabricated waveguides with various compensation coefficients of -0.15, -0.1, -0.05, 0, and 0.05, respectively. 40

Figure 3.5 (a) SEM images of the fabricated waveguides with bending radius of 75 μm . (b) SEM images of the fabricated waveguides with bending radius of 100 μm . (c) Tested transmission spectra of the fabricated waveguides with varying bending radii. (d) Extracted dependence relation of the loss on bending radius at the wavelength of 1550 nm. 44

Figure 3.6 (a) SEM images of fabricated spiral waveguides with length of 12.2 mm. (b) SEM images of the fabricated spiral waveguides with length of 23.3 mm. (c) and (d) are the enlarged images of (a) and (b) at two different positions, respectively. (e) Tested transmission spectra of the fabricated waveguides with different lengths of 8.1 mm, 13.08 mm, 20.82 mm, 23.9 mm, respectively. (f) Dependence of propagation loss on waveguide length at the wavelength of 1550 nm. 45

Figure 3.7 (a) SEM photograph of the fabricated MMI power splitter. (b) Normalized transmission spectra of the fabricated MMI power splitter. 48

Figure 3.8 (a) SEM photograph of the fabricated Y-branch power splitter. (b) Normalized transmission spectra of the fabricated Y-branch power splitter. 49

Figure 3.9 (a) SEM image of a fabricated waveguide MRR. (b) Measured normalized transmission spectrum of the MRR. (c) and (d) enlarged part of transmission spectra at the wavelengths around 1551 nm and 1600 nm, respectively..... 50

Figure 4.1 The design of an optofluidic chip with several directly printed polymer optical waveguide MZ micro-interferometer sensors..... 56

Figure 4.2 Flow chart of the processes used in the fabrication of an integrated optofluidic chip.....57

Figure 4.3 (a) Optical microscope image of the fabricated waveguide MZI sensor. The inset is a cross-section of waveguide, (b) SEM image of waveguide partially covered by Ormoclاد. The inset is close-up of the tapered waveguide. (c) SEM image of the fabricated 1:2 waveguide splitter. (d) SEM image of the fabricated 1:1 waveguide combiner..... 59

Figure 4.4 (a) Structure of the cross-section of designed SU-8 waveguide. (b) Calculated electrical field distributions of fundamental mode of the designed waveguides. (c) Simulated electric field distributions of the waveguide..... 60

Figure 4.5 (a) A photograph of a red-lit SU8 optical waveguide MZI sensor. (b) Image of an optofluidic device vertically integrated with a PDMS microfluidic layer on top of an optical waveguide chip. 64

Figure 4.6 (a) Photograph of a fabricated SU-8 mold for preparation of microfluidic chips by casting method. (b)-(e) Photos of the different parts of the SU-8 mold taken by using a laser scanning confocal microscope. The length of scale bars is 500 μm 65

Figure 4.7 Transmission spectra of the fabricated SU-8 waveguide MZI sensor. (a) The MZI sensor's spectrum without Ormoclاد cladding. (b) The MZI sensor's spectrum following construction with Ormoclاد coating. (c) The MZI sensor's spectrum in an optofluidic device following a water injection.68

Figure 4.8 Three designs of polymer waveguide Y splitters with different power splitting ratios: 1:1, 1:2, 1:4 69

Figure 4.9. Transmission spectra of the fabricated polymer waveguide MZI sensors using these three Y splitters in the input por of MZIs.70

Figure 4.10. (a) Simulated electrical field distribution of mode of 2.7- μm waveguide in air cladding, (i) TE_{11} mode, (ii) TM_{11} mode, (iii) TE_{21} mode, (iv) TM_{12} mode. (b) Simulated electrical field distribution of mode of 2.7- μm waveguide in Ormoclاد, (i) TE_{11} mode, (2) TM_{11} mode. 71

Figure 4.11 Simulated electrical field distribution of light transmission in (a) Ormoclاد/air and (b) Ormoclاد/water interface. The simulated excess loss

for Ormoclad/air interface and Ormoclad/water interfaces are 0.329 dB and 0.066 dB respectively..... 72

Figure 4.12 Long-tim test of the peak wavelength stability of a fabricated polymer waveguide MZI sensor immersed in water. The standard deviation (SD) is 30 pm..... 73

Figure 4.13. Test bulk sensitivity of the fabricated optofluidic chip. (a) The wavelength shift corresponding to the concentration of glucose in a water solution; (b) The wavelength shift corresponding to the change in refractive index. The inset shows the tested varying transmission spectra. 75

Figure 4.14 (a) A schemaic representation of the surface functionalization process for the detection of HIgG. (b) The dynamic response of the biosensor when exposed to a 1 ng/mL target antibody solution. (c) The responses of the biosensor to various concentrations of the target antibody..... 77

Figure 4.15 A comparison of the sensor's reactions to a control protein HSA and the target analyte HIgG. 78

Figure 4.16 Measured interference peak wavelengths in five cycles of HIgG detection on a manufactured optical MZI biosensor. 80

Figure 5.1 Optofluidic chip featuring multiple polymer optical waveguide MRR sensors that are directly printed onto the chip. 83

Figure 5.2 (a) Schematic of simulated structure of gapless coupler. (b) simulated electric field of gapless coupler when the overlap distance is 1200 nm. 85

Figure 5.3 Calculated coupling coefficient as function of overlap distance. 86

Figure 5.4 SEM images of MRR waveguide sensor. (b) 2.7 μm straight waveguide. (c) 2.4 μm ring waveguide. (d) gapless coupler. 89

Figure 5.5 Photograph of an optical waveguide chip with a PDMS microfluidic layer vertically placed on top of an optofluidic chip 90

Figure 5.6 Measured transmission spectra of the fabricated polymer waveguide MRR sensor. (a) Spectrum of the MRR sensor with air cladding. (b) Spectrum of the MRR sensor after fabrication of Ormoclad cladding. (c) Spectrum of the MRR sensor in optofluidic chip after injecting with water. (d) Close-up spectrum of the MRR sensor in water near the wavelength of 1544 nm.92

Figure 5.7 Transmission spectra of the fabricated MRR with different loss and coupling coefficients. 94

Figure 5.8 (a) Measured transmission spectra towards varying refractive index of solution. (b) Dependence of wavelength shift on the external refractive index change.95

List of acronyms

Acronyms	Description
MZI	Mach-Zehnder interferometer
MRR	Microring resonator
POC	Point-of-care
Q factor	Quality factor
PMMA	Poly-(methacrylate)
PDMS	Poly-(dimethylsiloxane)
DMD	Digital micromirror device
DOPsL	Dynamic optical projection stereolithography
OMsL	Optical maskless stereolithography
PAA	Polyacrylic acid
PNIPAAm	Poly(N-isopropylacrylamide)
FPI	Fabry-Pérot interferometric
LCoS	liquid crystal on silicon
FDE	Finite difference eigenmode
ER	Extinction ratio
LOD	Limit of detection
FSR	Free spectrum range
FWHM	Full width at half maximum

EBL	Electron-beam lithography
DUL	Digital ultraviolet lithography
DLW	Direct laser writing
CAD	Computer-aided design
MEMS	Microelectromechanical systems
MMI	Multi-mode interferometer
EME	Eigenmode expansion propagation
SEM	Scanning electron microscope
PEGDA	Polyethylene glycol diacrylate
WGM	Whispering gallery mode
ELISA	Enzyme-linked immunosorbent assay
VEGF	Vascular endothelial growth factor
LFIA	Lateral flow immunoassay
LoC	Lab-on-a-chip
TE	Transverse electric
TM	Transverse magnetic
HIgG	Human immunoglobulin G
MIBK	Methyl isobutyl ketone
<i>S</i>	Sensitivity
ASE	Amplified spontaneous emission
SMF	Single-mode optical fibers
DI water	Deionized water

SD	Standard deviation
BSA	Bovine serum albumin
APTES	(3-aminopropyl)triethoxysilane
HSA	Human serum albumin
PBS	Phosphate buffered solution
RIU	Refractive index units
SiON	Silicon oxynitride
AFM1	AflatoxinM1
Fab'	Fragments
CEA	Carcinoembryonic antigen
Si ₃ N ₄	Silicon nitride
LiNbO ₃	Lithium niobate
AlN	Aluminium nitride
BaTiO ₃	Barium titanate
Y ₃ Al ₅ O ₁₂	Yttrium aluminium
OoCs	Organ-on-chips

Chapter 1. Introduction

1.1 Background

Efficient and accurate biodetection tools play vital roles in tackling the global challenges of epidemic diseases-caused health crises. To facilitate the development of new-generation of healthcare devices, there is also a strong need of biomedical tools for high specificity, high sensitivity, multiplexing and non-invasive label-free biodetection. Recently, the need for compact, portable, multi-scenario adaptability has aroused great interest in the miniaturization of biomedical tools towards chip-scale diagnostic technologies for disease detection and general health monitoring. They are promising for real-time biomedical tests and can facilitate clinical diagnosis at the point of care (POC), ensuring timely and accurate interventions in healthcare [1]. Thanks to advanced nano/micro-photonic and microfluidic technologies, optofluidic biosensors experienced rapid growth and development in integrating lightwave with microfluidic technologies to create compact devices for label-free detection of molecules with high sensitivity and specificity.

However, traditional fabrication technologies in optofluidic chips have some limitations. For instance, electron beam lithography (EBL) and direct laser writing (DLW) are high-resolution and highly reliable maskless technology. On the other hand, it has drawbacks of low speed and low throughput, which are suitable for fabrication of small-size devices in low-volume applications. Although photolithography is a fast

and high throughput fabrication process, the photomask is expensive and its patterning flexibility is low [2]. Therefore, development of low cost, high throughput fabrication platform with high flexibility is a matter of urgency in the development of optofluidic chips.

Optofluidic chips can be achieved by integrating different types of photonics sensors, such as optical fibre, surface plasmonic resonance sensors, photonic crystal sensors, interferometer-based sensors, optical waveguide sensors, optical resonator sensors, within microfluidic channels. Planar optical waveguide sensors possess advantages such as compact size, high integration density, compatibility with fiber optics, and tailored optical properties. Typically, Mach-Zehnder interferometers (MZI) and micro-ring resonator (MRR) are the most common sensors used in integrated photonic biochips. In an MZI, input light is split into two paths by a beam splitter. These two beams of light pass through two waveguides of different lengths and then recombine at the output waveguide. The two recombined light waves interfere with each other, resulting in an interference due to phase difference after propagating different optical paths. In an MRR, light coupled to the micro ring from a straight waveguide via e.g. evanescent coupling or contact coupling [3]. The light then circulates inside the ring when the resonance condition is fulfilled, and then a resonant spectral dip will appear in the transmission optical spectrum. Indeed, MZI and MRR are widely used in integrated photonics for various applications, such as including filtering [4], switching [5], modulation [6], and sensing [7].

Because of its great potential, optical waveguide-based optofluidic chips have become one of the most promising technologies for many different applications, such as temperature sensing [8], refractive index sensing [9], volatile organic compounds gas sensing [10], water contaminants detection [11], protein detection [12], parasite detection [13], etc. They offer great many new opportunities in the development of small-size high-performance microdevices for environmental monitoring and human health evaluation.

1.2 Motivation and objectives of the research

Small size and high-performance optofluidic chips are highly desired in many applications due to the advantages of miniaturization, high sensitivity, high specificity, and rapid response. For instance, in some limited resources settings, especially for those with poor health service or laboratory, it is unrealistic to use advanced medical facilities, which need highly trained personnel and specialized facilities [14]. In such a case, optofluidic biochip provides a feasible solution for patient-centred diseases primary diagnosis. Although optical waveguide-based optofluidic biosensors have been widely studied in the past few years, most of the previous works focus on silicon-based waveguide devices and rely on time-consuming and high-cost fabrication techniques. By using an own-built DMD-based digital ultraviolet lithography (DUL) system, cost-effective polymer waveguide-based integrated optofluidic biochips can be developed

In this thesis, we developed a new fabrication process for polymer optical waveguide devices by using a DUL system, and then used it to further develop two kinds of optical waveguide biosensors for integrated optofluidic chips. To fabricate high-quality optical waveguides, we systematically optimize the processing techniques and their parameters. After process optimization, we developed polymer waveguide MZI sensors and integrate them with microfluidic layer to make optofluidic chips for human IgG detection. Moreover, an optofluidic chip based on microring resonators has also been fabricated. The Q value of the fabricated MRR sensor is quite high, which indicates that it is promising platform for low-limit detection of disease biomarkers in biomedical applications.

1.3 Outline of the thesis

The chapters of the thesis are organized as below:

Chapter 1: Introduction. This chapter provides an overview of the optofluidic biochip, discussing the background and research motivation. The research project's objectives are outlined, and the structure of the thesis is presented.

Chapter 2: Overview of optofluidic chip technologies based on optical waveguide sensors. In this chapter, optofluidic chips based on different types of optical sensors and its applications are review. Typical sensing mechanisms and application of optical waveguide sensors, especially MZI and MRR sensors, are described. The conventional optical printing technologies and maskless lithography are also introduced and discussed.

Chapter 3: Fabrication of polymer optical waveguides by digital ultraviolet lithography. In this chapter, we present a digital ultraviolet lithography technology for fabricating polymer optical waveguides. The fabrication processes and parameter optimization are described in detail. The optical characteristics of the fabricated polymer optical waveguides are also presented.

Chapter 4: Optofluidic chip with directly printed polymer optical waveguide Mach-Zehnder interferometer sensors. In this chapter, polymer waveguide MZ micro-interferometer sensors are demonstrated by using DUL technology. The fabricated waveguide chips were then packaged with a microfluidic layer to make an optofluidic chip for label-free biodetection. The use of the fabricated optofluidic chip for high-sensitivity detection of human IgG was demonstrated in experiments.

Chapter 5: Optofluidic chip with high-Q polymer waveguide microring resonator sensors. In this chapter, polymer optical waveguide micro-ring resonator sensors were demonstrated by using DUL technology. The fabricated optical waveguide chips were packaged with a microfluidic layer to make an optofluidic chip for label-free biodetection.

Chapter 6: Conclusions and future outlook. This chapter presents a concise summary of the thesis and outlines the future prospects for optofluidic chips with directly printed polymer optical waveguide sensors in biodetection applications.

Chapter 2. Overview of optofluidic chip technologies based on optical waveguide sensors

2.1 Introduction

In this chapter, fundamental principles and recent progress of optofluidic chip technologies, particularly optical waveguide sensor-based optofluidic chips, are reviewed. Different types of optical waveguide sensors, especially waveguide MZI and MRR sensors, for on-chip optofluidic biodetection are summarized. Sensing mechanisms of the two waveguide sensors are described. Typical lithography technologies for fabricating optical waveguides are also reviewed.

2.2 Optofluidic chip technologies

With increasing demands on point of care (POC) testing and diagnostics, many problems have arisen in traditional methods involving complex sample pretreatment and analysis, such as labour-intensive and costly. Therefore, there is an urgent need to develop miniature and affordable biochips to alleviate this situation. Optofluidic chips integrate optical and microfluidic components on a single chip-scale platform. The quantity testing result can be obtained rapidly because of the fast response of optical sensors. Because of the small size, highly integration, less analyte consumption, rapid turnaround times, optofluidic chips have become an ideal solution for many applications, such as drug development & disease modelling [15], point-of-care (POC) testing [16], imaging resolution enhancement in microscope [17], cell operation and

analysis [18], environmental sensing [19], as shown in the **Fig. 2.1**. Many optical sensing techniques have been adopted into optofluidic chips such as optical fibres [20], fluorescence [21], waveguides [22], surface plasmon resonance [1] and microarrays [23].

Among these technologies, optical waveguide sensor-based optofluidic chips provide universal and robust transduction platforms for sensitive and efficient detection for diseases in an early stage. Optical waveguides include a higher refractive index layer in the middle for light propagation, and two lower refractive index layers in the two side for mode confinement. Although most of light confined within the

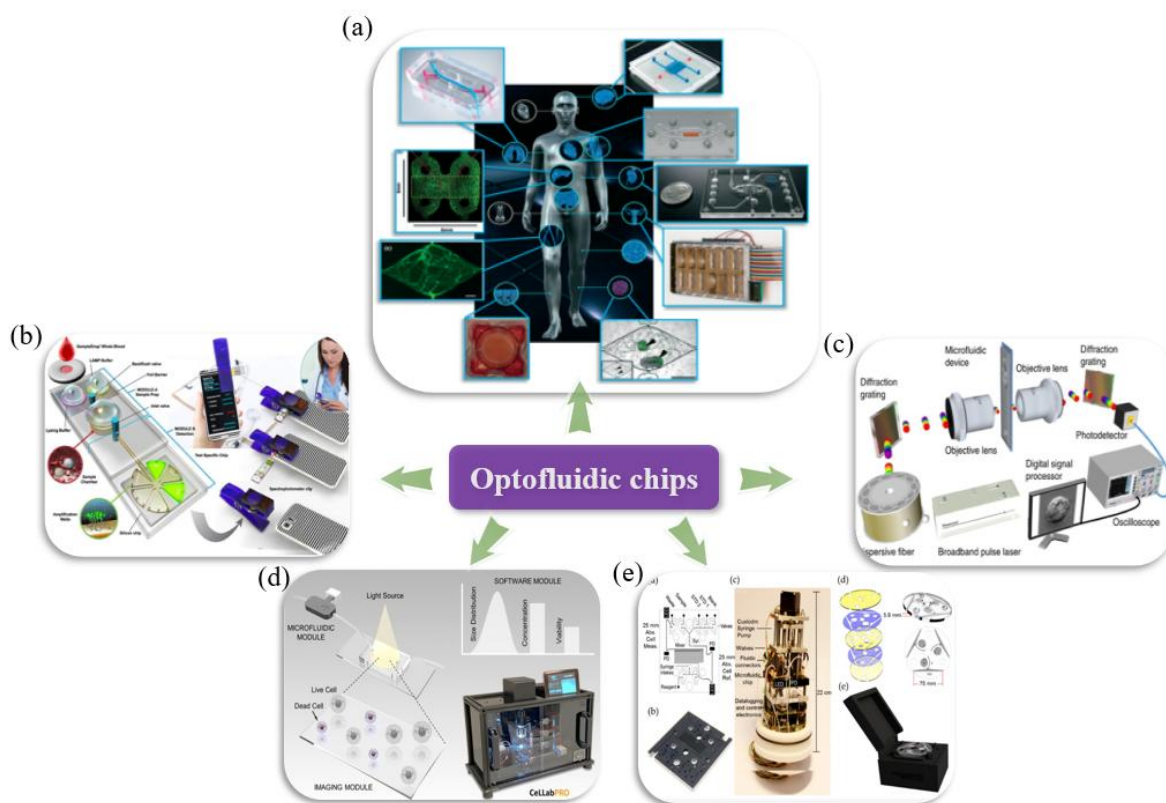


Figure 2.1 Optofluidic chips developed for different applications: (a) Drug development & disease modelling [15], (b) Point-of-care (POC) testing [16], (c) Imaging resolution enhancement in microscope [17], (d) Cell operation and analysis [18], (e) Environmental monitoring [19].

guiding layer, small portion of the light extends to the surface of waveguide and contact with analyte, which is called as evanescent wave. Both refractive indexes changing and surface biomolecular binding activity affect the speed of the light transmitted in the waveguide via evanescent wave and thus can be utilized for biosensing [24]. A stronger evanescent field is beneficial to the sensor's sensitivity, but meanwhile the propagation loss will increase. As a result, appropriate balance of propagation loss and sensitivity is very necessary.

For instance, Densmore *et al.* demonstrated a silicon photonic MZI biosensor array for simultaneous detection of two biomarkers (Fig. 2.2(a)) [12]. Their results showed that the biochip was able to detect goat and rabbit IgG at the same time, with a detection limit of about 1.2 ng/mm². Andrea *et al.* presented a three-dimensional MZI in a microfluidic chip, as shown in Fig. 2.2(b). They inscribed an MZI into a commercial microfluidic chip by ultrafast laser writing [25]. Sensing arm of the MZI orthogonally crossed the micro-channel, and the reference arm passed over it. As for the limit of detection, the device can test the induced refractive index change of a glucose solution concentration of 1×10^{-4} RIU. Qing *et al.* presented a MZI-miRNA detection system for multiple biomarkers detection in label free manner, as shown in Fig. 2.2(c) [26]. It can detect two types of miRNAs in urine samples of bladder cancer patients in a single test.

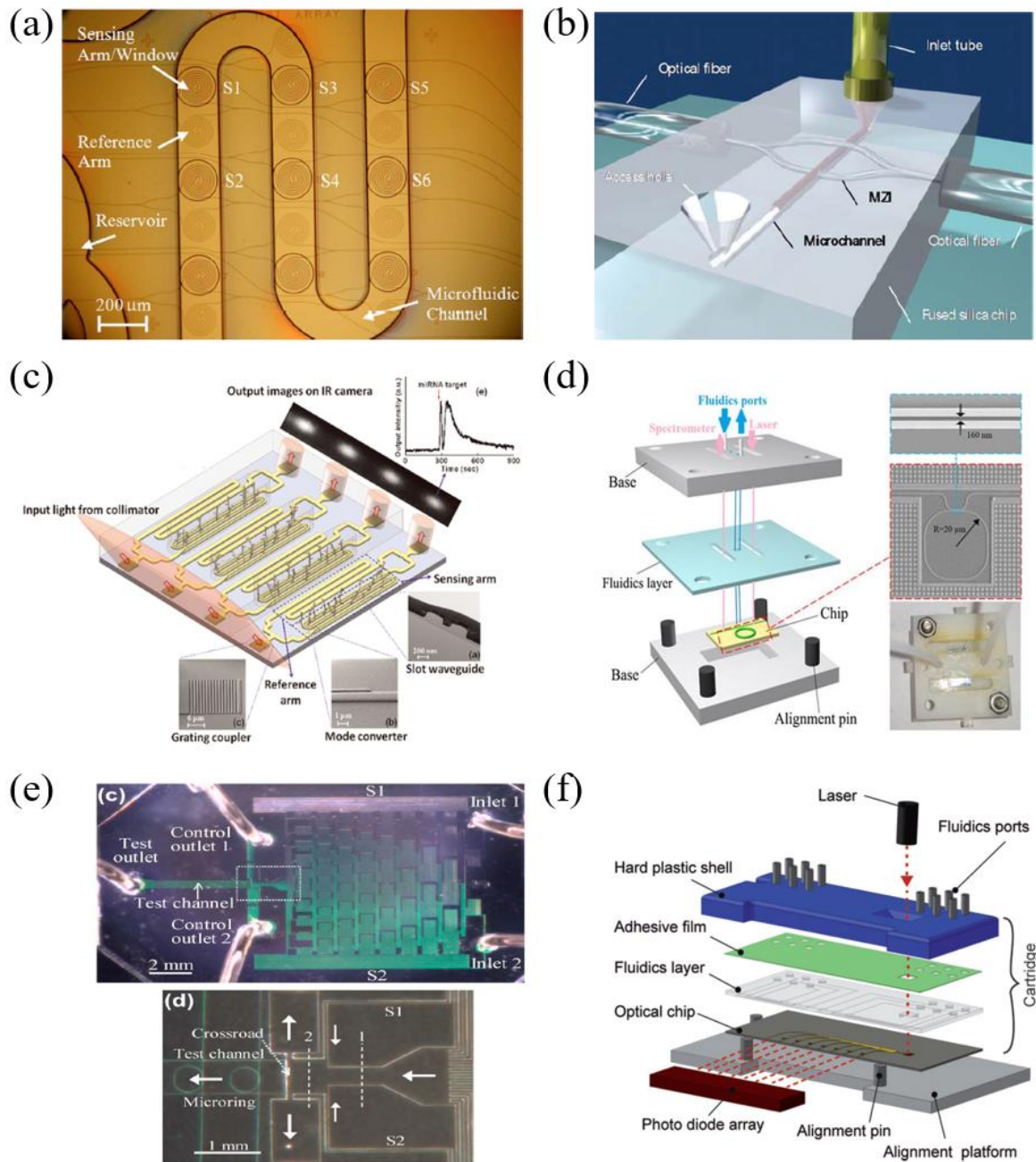


Figure 2.2 Optofluidic chips based on optical waveguides. (a) A silicon photonic MZI biosensor array integrated with microchannel. (b) Three-dimensional MZI sensor integrated microfluidic chip. (c) An MZI sensor-based point-of-care system. (d) A microring resonator-based optofluidic chip. (e) An optical microring resonator with on-chip microfluidic tuning. (f) An optofluidic chip consisting of arrayed optical slot-waveguide ring resonators.

Wu. *et al.* demonstrated a label-free MRR biosensor-based microfluidic device, which consist of two poly-(methylmethacrylate) (PMMA) base and poly-(dimethylsiloxane) (PDMS) microchannel, see Fig. 2.2(d) [27]. The alignment was carried out with the assistance of four pins. The results revealed that the chip can detect human immunoglobulin G with detection limit of 0.5 $\mu\text{g/mL}$. Notably, the optofluidic chip consumed only 30 μL sample solution in a test. Uriel *et al.* designed an optofluidic chip based on a micro-ring resonator that located inside a microfluidic channel, as shown in Fig. 2.2(e) [28]. The upper cladding of the waveguide sensor is flowing liquid in the channels. The resonance wavelength and the coupling coefficient can then be tuned by changing the refractive index of flowing liquid. The resonant wavelength can be tuned by 2 nm, and its extinction ratio was achieved to be 37 dB. Carlborg *et al.* presented an optofluidic biochip based an array of slot waveguide MRR sensors, which were incorporated within the microfluidic layer embedded in a compact cartridge, for multi-biomarkers parallel testing, as shown in Fig. 2.2(f) [29]. A dual surface-energy adhesive was applied to ensure a tight binding of plastic shell and PDMS microfluidic network. The LOD of the sensor is 5×10^{-6} RIU, and the detection limit of surface mass density is 0.9 pg/mm.

2.3 Optical waveguide sensors for optofluidic chips

According to different working principles, optical waveguide sensors can be classified into planar waveguide sensor [9], spiral waveguide sensor [30], Y splitter

sensor [31], micro-ring resonator sensor [32], Mach-Zehnder interferometer (MZI) sensor as well as grating waveguide sensor [33], as shown in Fig. 2.3.

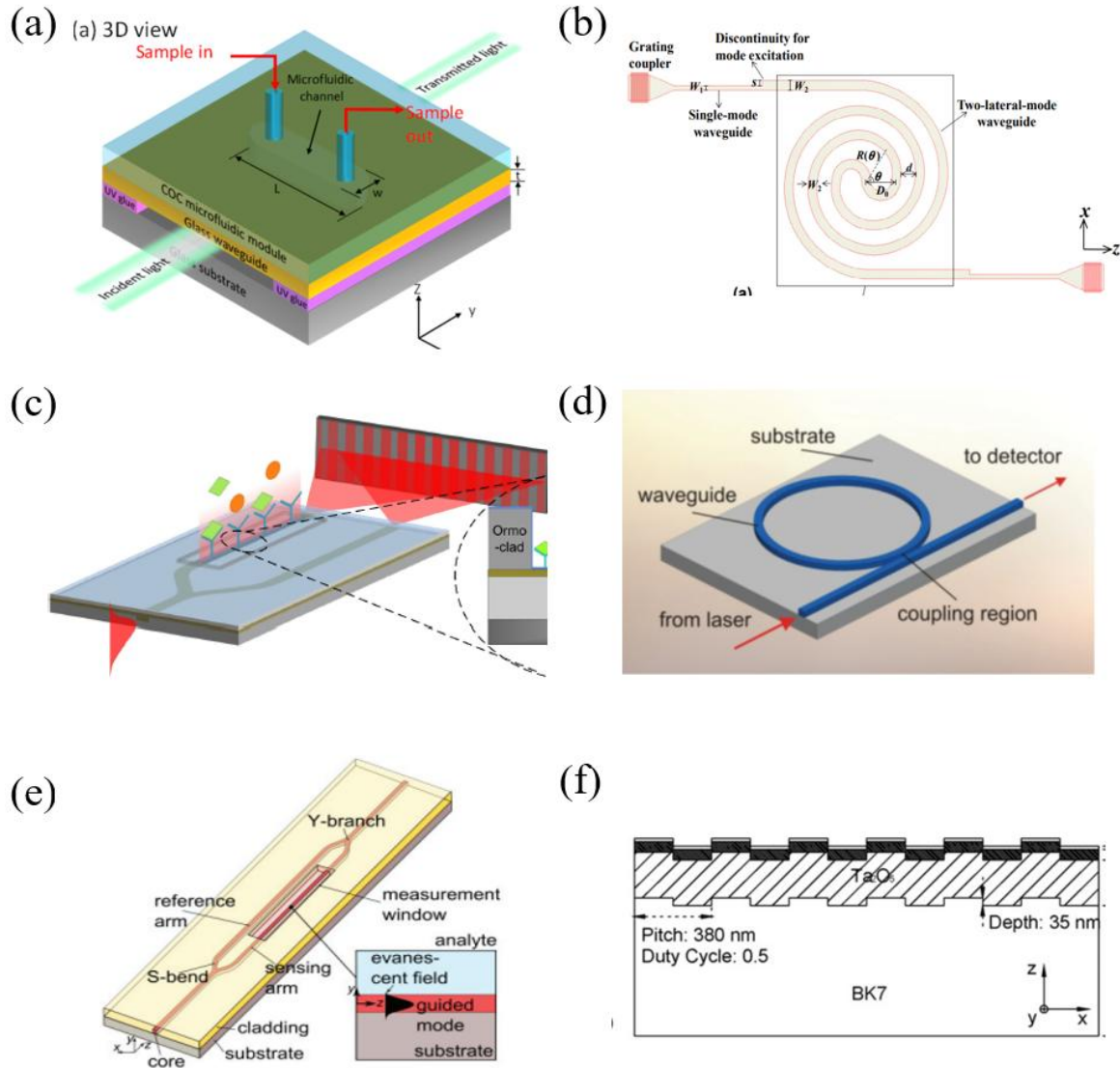


Figure 2.3 Different types of optical waveguide sensors. (a) Planar waveguide sensor [9], (b) spiral waveguide sensor [31], (c) Y splitter sensor [32], (d) microring resonator sensor [33], (e) Mach-Zehnder interferometer (MZI) sensor [33], (f) grating waveguide sensor [34].

Among these sensor schemes, optical waveguide MZI and MRR sensors have been widely considered as the most promising approach for integration with microfluidics

to develop optofluidic chips. In the following section, the sensing mechanisms of MZI and MRR sensors are summarized.

2.3.1 Optical waveguide Mach-Zehnder interferometer (MZI) sensors

An MZI sensor consists of an input waveguide, an output waveguide, a Y-shaped beam splitter, a Y-shaped combiner, a sensing arm, and a reference arm. In an asymmetric MZI, as depicted in Fig. 2.4(a), the input light is coupled to the input waveguide and then split into two beams along with two arms by the waveguide splitter. The two beams travel a specific distance following recombining at the coupler. The sensing arm is a bare core waveguide for detecting analytes, while the reference arm is protected with polymer cladding and does not contact with the liquid analytes in a test. Consequently, the output optical power for a specific wavelength varies as a result of the phase difference change between the light waves after propagating through the two arms.

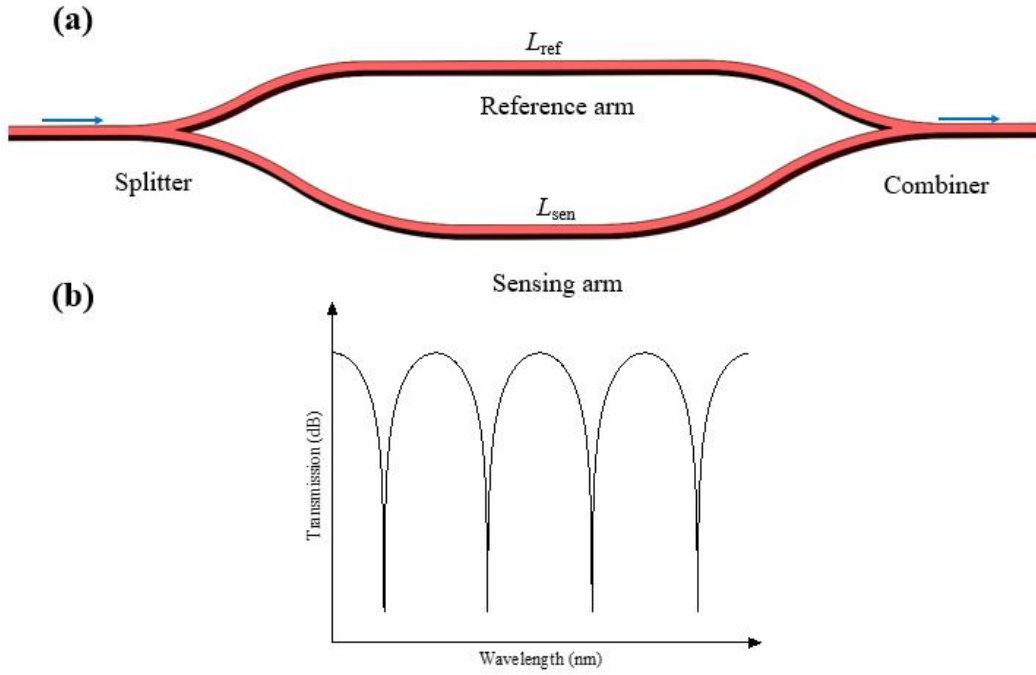


Figure 2.4 Basic structure of an optical waveguide MZI sensor. (a) Asymmetric MZI waveguide sensor. (b) Typical transmission spectrum of an MZI sensor.

According to the mechanism of evanescent field sensing, variations in the environment affect the effective refractive index of the mode transmitted in the sensing arm. This alteration in refractive index leads to phase modulation affecting the interference of the two arms, resulting in the generation of a phase difference change. A transmission peak occurs when the phase difference between the reference arm and the sensing arm is an integer multiple of 2π . Mathematically, this can be expressed as follows:

$$m \cdot 2\pi = 2\pi \frac{n_{e1}}{\lambda} L_1 - 2\pi \frac{n_{e2}}{\lambda} L_2, \quad (2.1)$$

where m is an integer, and n_{e1} , n_{e2} , L_1 , L_2 are the effective indexes and the lengths of sensing arm and reference arm, respectively. λ refers to lightwave wavelength.

If the refractive index of the medium surrounding sensing arm has a change, a shift of resonance wavelength will happen. If assume that the resonance wavelength changes from λ_1 to λ_2 , the equation under two states can be written:

$$m\lambda_1 = n_{e1}L_1 - n_{e2}L_2, \quad (2.2)$$

$$m\lambda_2 = n_{e3}L_1 - n_{e2}L_2, \quad (2.3)$$

where n_{e3} is the effective index of sensing arm after changing the upper cladding. Then, we make Eqn. (2.2) - Eqn. (2.2) to obtain:

$$m\Delta\lambda = \Delta n_e L_1. \quad (2.4)$$

As the effective index of an optical waveguide mode depends on the refractive index of external medium and the lightwave wavelength, Δn_e could be approximated as:

$$\Delta n_e = \frac{\partial \Delta n_e}{\partial n_c} \Delta n_c + \frac{\partial \Delta n_e}{\partial \lambda} \Delta \lambda, \quad (2.5)$$

where n_c is the refractive index of surrounding medium. If assume $L_1=L_2$, the wavelength shift induced by a variation of external refractive index can be found by substitute Eqn. (2.5) into Eqn (2.4) as:

$$\Delta\lambda = \frac{\lambda \cdot \frac{\partial n_e}{\partial n_c} \cdot \Delta n_c}{\Delta n_e - \lambda \left. \frac{\partial \Delta n_e}{\partial \lambda} \right|_{\lambda=\lambda_m}}. \quad (2.6)$$

To simplify the equation, we can define n_g as group index as [34]:

$$n_g = n_e - \lambda \left. \frac{\partial n_e}{\partial \lambda} \right|_{\lambda=\lambda_m}. \quad (2.7)$$

Furthermore, we define $\partial n_e / \partial n_c$ as waveguide sensitivity S_w . Then the induced change of group index, i.e., Δn_g , is:

$$\Delta n_g = \Delta n_e - \lambda \left. \frac{\partial \Delta n_e}{\partial \lambda} \right|_{\lambda=\lambda_m} . \quad (2.8)$$

With Eqn. (2.8), Eqn. (2.6) can be rewritten to:

$$\Delta \lambda = \frac{\lambda \cdot S_w \cdot \Delta n_c}{\Delta n_g} . \quad (2.9)$$

The important parameters for describing the spectral characteristics and sensing performances of an MZI sensor include:

- 1) Free spectra range (FSR), i.e., the wavelength spacing between two resonance dips, which determines the sensing range of a MZI sensor, is:

$$FSR = \frac{\lambda^2}{n_{g1}L_1 - n_{g2}L_2} . \quad (2.10)$$

- 2) Bulk sensitivity. It describes the sensitivity of an MZI sensor's spectrum to a small change of surrounding refractive index. For a symmetric MZI, its bulk sensitivity is mainly determined by the waveguide sensitivity rather than arm length.

$$S = \frac{\Delta \lambda}{\Delta n_c} = \frac{\lambda}{\Delta n_g} \cdot \frac{\partial n_e}{\partial n_c} . \quad (2.11)$$

- 3) Limit of detection (LOD), known as smallest change in surrounding medium that a sensor can detect. 3σ method refers to a value estimated by using three times sigma of the measured background noise to their average. If a

measurement result exceeds this value, then the signal from a sample can be detected.

$$\text{LOD} = \frac{3\sigma}{S}. \quad (2.12)$$

2.3.2 Optical waveguide micro-ring resonator (MRR) sensors

Optical waveguide MRRs exhibit advantages such as a compact size, high quality (Q) factor and excellent wavelength selectivity. The ring cavity of MRRs enables optical feedback, making them suitable for integration with various optoelectronic devices. Therefore, they find extensive applications in integrated optoelectronics, optical communications, and other related areas [35].

MRR devices typically comprise a microring waveguide coupled to a strip waveguide, as shown in Fig. 2.5 (a). Light is coupled into the strip waveguide and propagates to the coupling region. In this coupling region, a part of the light in the strip waveguide coupled into the ring, the remaining continue to propagate. The light coupled into the microring interferes with the light in the strip waveguide after circulating around the ring. For the light waves satisfying the resonant condition, a resonance enhancement effect will be generated in the low-loss microring waveguide, resulting in a relatively strong optical field confined within the ring waveguide. Resonances are generated when the optical path of microring is an integer multiple of the wavelength of the incident light. The MRR resonance equation can be written:

$$2\pi Rn_e = m\lambda, \quad (2.13)$$

where R represents the radius of the microring, λ refers to the resonance wavelength. Notably, the shape of ring is not necessary to be a circle. For example, racetrack [36] or spiral [37] also can also be used for increasing interaction length.

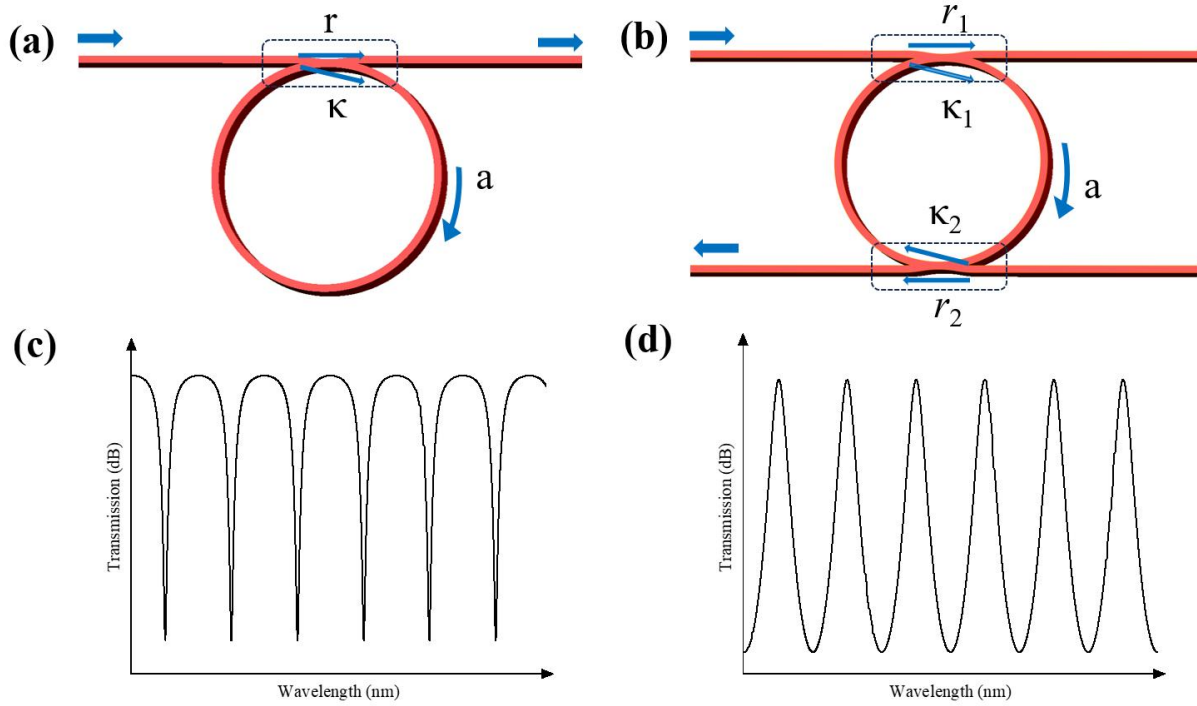


Figure 2.5 Two basic configurations of MRR: (a) All pass ring resonator; (b) Add-drop ring resonator. (c) The transmission spectrum of the first configuration is a spectrum of periodic notch resonances. (d) The spectrum from the drop port of the second configuration is a complementary shape of the spectrum of throughput port.

The most common ring resonators include all-pass ring resonator and add-drop ring resonator, as shown in Fig. 2.5. As for an all-pass ring resonator, as shown in Fig. 2.5 (a), the ratio of transmitted and incident field in the bus waveguide can be written as:

$$\frac{E_{pass}}{E_{input}} = e^{i(\pi+\phi)} \frac{a - re^{-i\phi}}{1 - rae^{i\phi}}, \quad (2.14)$$

where $\phi=\beta L$ refers to the single-pass phase shift, and L, β, a are the round-trip length, propagation constant of optical mode, single-pass amplitude transmission, respectively.

By squaring Eqn. (2.14) we obtain the intensity T_n :

$$T_n = \frac{I_{\text{pass}}}{I_{\text{input}}} = \frac{a^2 - 2ra \cos \phi + r^2}{1 - 2ar \cos \phi + (ra)^2}, \quad (2.15)$$

where r is self-coupling coefficient, and k is cross-coupling coefficient. r and k are the splitting ratios of the coupler. If assume that there is no loss in coupling area, they satisfy [3]:

$$r^2 + k^2 = 1. \quad (2.16)$$

The full width at half maximum (FWHM) for an all-pass ring resonator can be derived to be:

$$\text{FWHM} = \frac{(1 - ra)\lambda_{\text{res}}^2}{\pi n_g L \sqrt{ra}}. \quad (2.17)$$

For an add-drop ring resonator, it is:

$$\text{FWHM} = \frac{(1 - r_1 r_2 a)\lambda_{\text{res}}^2}{\pi n_g L \sqrt{r_1 r_2 a}}. \quad (2.18)$$

Spectral peak sharpness is measured using the quality factor (Q -factor), which is correlated with the FWHM and resonance wavelength as

$$Q = \frac{\lambda_{\text{res}}}{\text{FWHM}}. \quad (2.19)$$

For an all-pass ring resonator, it is

$$Q = \frac{\pi n_g L \sqrt{ra}}{(1 - ra) \lambda_{res}}. \quad (2.20)$$

On the other hand, for an add-drop ring resonator, which shown in Fig. 2.5 (d), it is

$$Q = \frac{\pi n_g L \sqrt{ar_1 r_2}}{(1 - ar_1 r_2) \lambda_{res}}, \quad (2.21)$$

where r_1 and r_2 refers to the coupling ratios of two couplers of add-drop ring resonator, whose values range from 0 to 1.0. From Eqn. (2.20) and Eqn. (2.21), one can understand that Q factor of all-pass ring resonators can be higher than that of add-drop ring resonators, when the effective indexes and the length of waveguides are same [38]. So, in this thesis we choose all-pass ring resonators in our research experiments.

From Eqn. (2.20), we can find that the Q factor depends on the waveguide loss and coupling ratio, when the group index and the perimeter of ring waveguide is fixed. In the Chapter 5, we will further discuss the impact of waveguide loss and coupling ratio on MRR Q factors.

2.4 Fabrication technologies for optical waveguide

As we know, typical fabrication technologies for optical waveguides include optical lithography [39], e-beam lithography [40], laser direct writing [41], as shown in Fig. 2.6. They are all well-established technologies with high resolution, but all of them have their own shortages.

2.4.1 Typical fabrication techniques

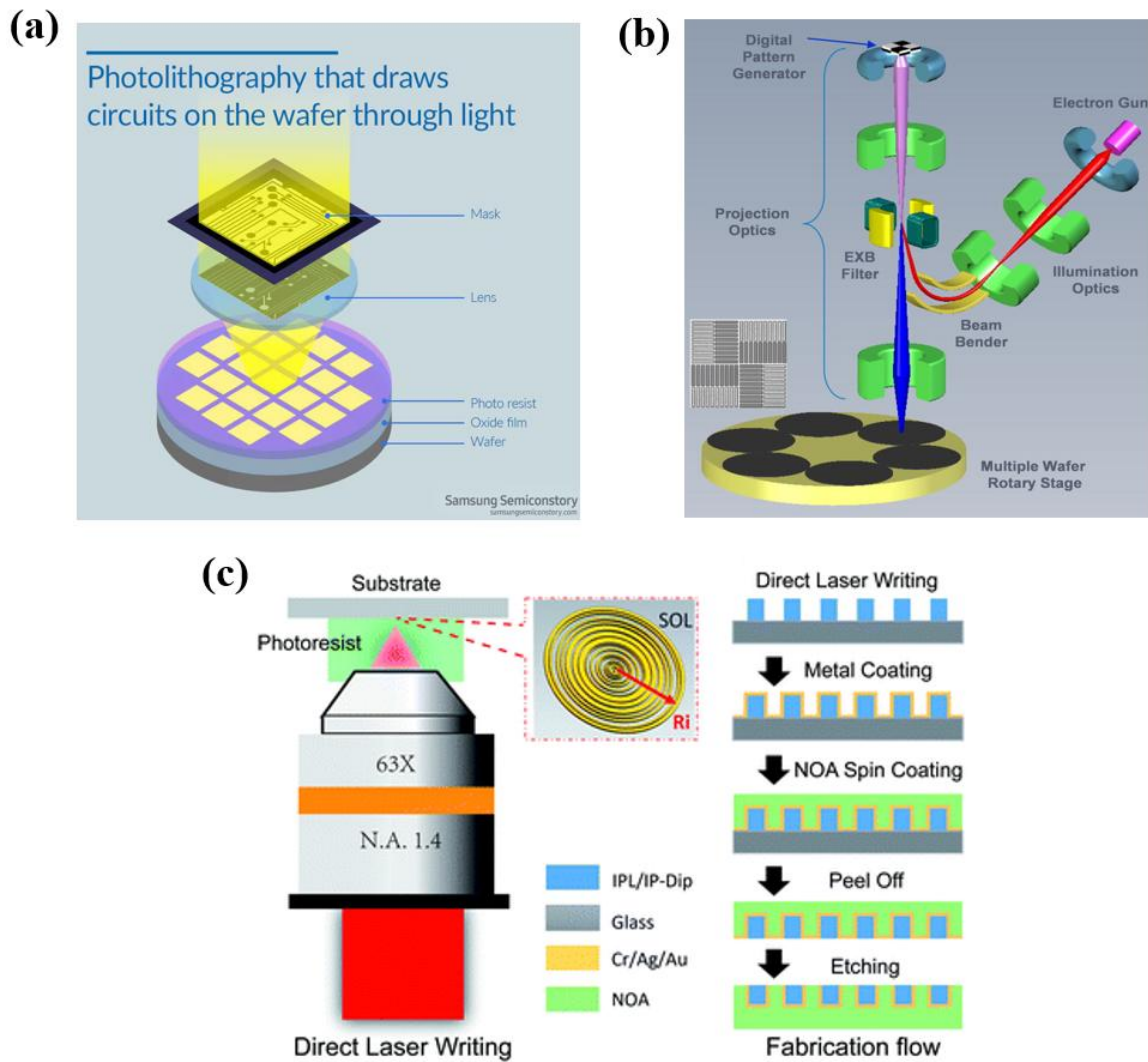


Figure 2.6 Typical fabrication technologies: (a) optical lithography [42], (b) e-beam lithography [43], (c) direct laser writing [41].

A crucial step in the production of semiconductors is optical lithography, which transfers a pattern from a photomask to a photosensitive substance using light [44,45]. The typical fabrication processing is shown in Fig. 2.7 [40]. During exposure, light passes through the mask and irradiates the photoresist-coated substrate. After baking and development, the patterned resist layer can serve as a mask for subsequent fabrication steps such as etching and deposition. Optical lithography enables the precise replication of patterns, playing a crucial role in the production of advanced

microelectronics devices. Its ability to create intricate patterns plays a crucial role in the miniaturization and integration of complex circuitry in modern integrated circuits. However, the optical lithography technique lacks flexibility in vertical dimensions. Besides, a photomask needs to be fabricated in advance, which is high-cost and time-consuming, and minor change of photomask is not allowed.

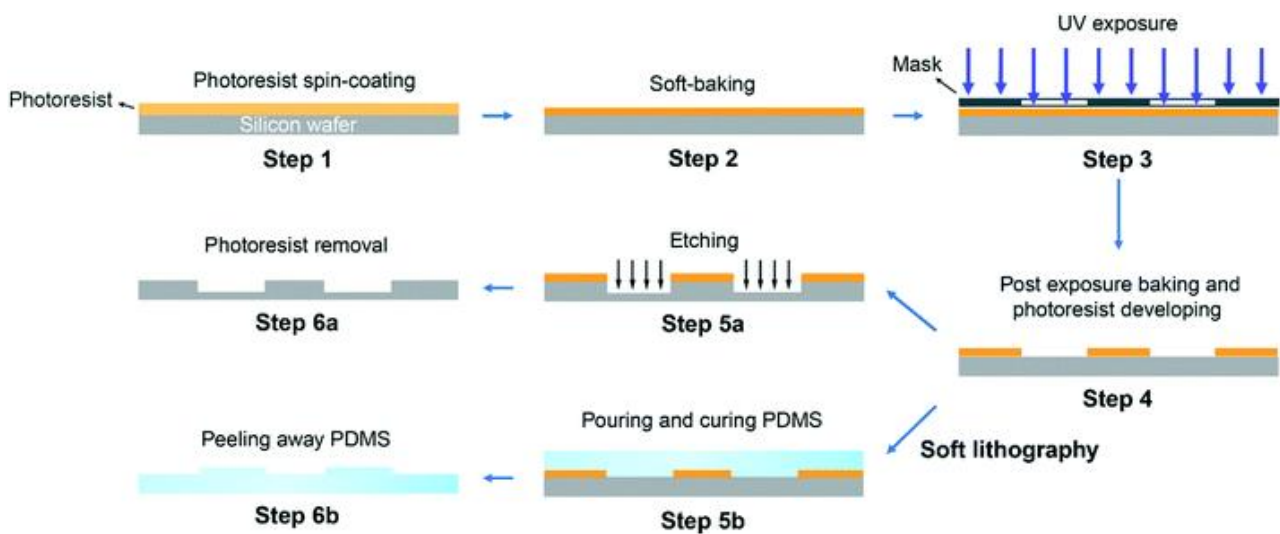


Figure 2.7 Flow chart of typical optical lithography processes [41].

EBL acts an important role in the development and fabrication of nanoelectronics, photonics, and nanoscale devices [46–48]. In EBL, a beam of electrons is emitted from an electron source, typically a field emission gun. The electron beam is then focused using electromagnetic lenses and directed onto a substrate coated with a thin layer of electron-sensitive resist material. The resist material will undergo a chemical or physical change upon exposure to the high-energy electrons, which enables the selective removal or protection of specific regions. The patterning process in EBL is achieved by scanning the focused electron beam across the resist-coated substrate, following a pattern predefined by a computer-generated mask. The mask, often created

using a specialized software, directs the beam's movement to form the desired nanostructures. The electron beam can be precisely controlled, allowing for sub-10 nanometer resolution and the creation of complex patterns. After exposure, the resist-coated substrate undergoes a series of post-exposure processes, including development, rinsing, and drying. The development step selectively removes either the exposed or unexposed regions of the resist, resulting in the formation of a patterned resist mask, which can then be used as a template for subsequent fabrication processes such as etching, deposition, or implantation to create the desired nanoscale structures on the substrate.

EBL offers several advantages over other lithographic techniques. Its high resolution and flexibility make it suitable for fabricating intricate nanoscale patterns. Additionally, EBL allows for direct writing of patterns, enabling rapid prototyping and quick iteration in research and development. However, EBL also has its own drawbacks. It is very time-consuming and requires specialized equipment and expertise. The throughput of EBL is much lower than optical lithography techniques, limiting its scalability for large-scale production. Moreover, the proximity effects caused by electron scattering can lead to distortions in final patterns, requiring additional correction techniques.

Direct laser writing (DLW) is an advanced nanofabrication technique that enables the precise and rapid fabrication of not only two-dimensional but also three-dimensional nanostructures with submicron resolution [49–51]. It utilizes a focused laser beam to directly pattern materials, enabling the creation of complex and

customizable nanostructures in a single-step process. DLW has gained significant attention in various fields, including photonics, plasmonics, and metamaterials.

In DLW, a photosensitive substance or photoresist is subjected to a closely focused high-power laser beam. The intense light energy induces various photochemical or photophysical processes in the photoresist, resulting in either polymerization or ablation. Polymerization occurs when the photoresist undergoes a chemical reaction and solidifies in the exposed regions, while ablation involves the removal of material through vaporization or melting. The patterning process in DLW is achieved by scanning the focused laser beam across the photoresist surface while precisely controlling its position and intensity. This enables the creation of intricate 3D structures by stacking multiple 2D patterns layer by layer. The scanning is typically controlled by computer-aided design (CAD) software, providing the necessary instructions for the laser beam's movement to produce the desired nanostructures.

DLW offers several advantages compared to traditional optical lithographic techniques. It allows for rapid prototyping and quick iteration, as it doesn't require for photomasks. This direct-writing capability enables the fabrication of highly customized and complex nanostructures relatively easier. Additionally, DLW offers high resolution and the ability to create arbitrary patterns, empowering researchers to explore novel designs and functionalities.

However, DLW also faces their own challenges. Its achievable throughput is limited due to the nature of the single-spot scanning process, making it less suitable for large-scale production. Additionally, the resolution and speed of DLW are

influenced by many factors such as laser power, focusing optics, and material properties, requiring careful optimization for specific applications.

2.4.2 DMD-based Maskless lithography technology

Maskless lithography technology based on digital micromirror devices (DMDs) has emerged as a versatile approach for micro/nano-fabrication. In this technique, a DMD acts as a programmable, dynamic mask, replacing the traditional static photomask used in conventional photolithography.

A DMD chip is a high-speed spatial light modulator, which consists of a two-dimensional array of tiny mirrors that can be individually tilted to either one of two positions. A typical example is 0.7" 1024 × 768 eXtended Graphics Array (XGA) DMDs, which have a micromirror tilt angle of 12°, with micromirror pitch of 13.68 μm, and the packaged chip size is 40.64 mm × 31.75 mm [52]. Fig. 2.8 (b) shows two DMD pixels that tilted into two opposite states. These mirrors are controlled digitally, allowing precise manipulation of the reflected light beam. The device's mirrors are all able to be slanted, enabling the presentation of "ON" and "OFF" states. When it is in the "ON" state, light is reflected by the micromirrors and enters the optical projection system. On the other hand, the light is diverted from the intended course when it is in the "OFF" state. By rapidly modulating the mirrors' positions, a series of light and dark pixels can form the desired images.

A. Ping *et al.* developed a dynamic optical projection stereolithography (DOPsL), establishing a new stereo-biofabrication method in 2012 [53]. As shown in Fig. 2.8(a), the system includes 1) a UV light source, 2) a computer for uploading sliced image, 3)

a DMD chip, 4) a series of projection optics, 5) a position control stage. It is capable of fabricate complex 3D extracellular microenvironments rapidly with customized geometry. The *in vitro* results revealed that the scaffolds have promising capability to guide and manipulate cell-cell interactions and multicellular organizations. However, it still had some limitations on fabrication of hydrogel-based devices. In 2016, they presented an optical maskless stereolithography (OMsL) technology by introducing an optical imaging technology, which improved features of *in-situ* micro-fabrication and large-scale patterning [54]. The Polyacrylic acid (PAA) ionic hydrogel can be accurately printed on the surface of a tapered optical microfiber to develop an ultrasensitive fiber-optic pH sensor. After that, by using the OMsL technique, an on-chip *in-situ* patterning poly(N-isopropylacrylamide)(PNIPAAm) microvalves [55] and micropatterned elastic gold-nanowire/polyacrylamide composite hydrogels for wearable pressure sensors [56] were developed in 2016 and 2018 respectively.

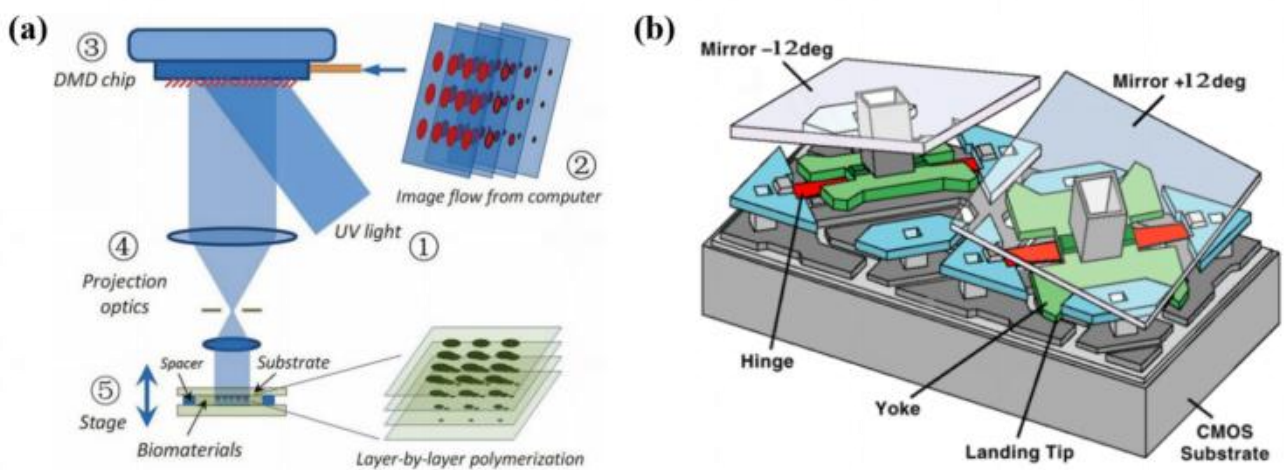


Figure 2.8 (a) Schematic diagram of dynamic optical projection stereolithography (DOPsL) [53]. (b) Two DMD pixels tilted into "ON" and "OFF" state respectively [52].

Besides, various kinds of ultrasmall optical fiber-tip sensor also fabricated with an in-house optical 3D μ -printing setup. SU-8 polymer micro-structures were precisely printed onto the end face of fibers, from which the Fabry-Pérot interferometric (FPI) sensors [57,58] and miniaturized suspended structure sensors [59–62] have been demonstrated for gas detection, pressure sensing as well as acoustic sensing. On-chip nano/micro-structure device, such as polymer optical WGM microcavity [63], also been presented. With the well-developed maskless optical lithography technology, on-chip optofluidic chip that integrated with optical components can be fabricated rapidly and further used for point for care analysis [20,64–66].

This kind of DMD-based maskless lithography technology offers several advantages in comparison with traditional photomask-based lithography. Firstly, it eliminates the need for physical photomasks, which are typically high-cost and time-consuming to fabricate, particularly for low-volume or prototyping applications. The programmable nature of the DMD allows for rapid, flexible, and cost-effective changes to the exposure pattern, enabling quick design iterations and reduced time-to-market.

Moreover, DMD-based maskless lithography can provide enhanced resolution and accuracy compared to conventional projection lithography systems. The high-density mirror array of DMD and projection control algorithms may enable the creation of intricate and high-resolution patterns on a photosensitive substrate.

Furthermore, it offers the ability to perform multiple exposures or grayscale exposures within a single lithography step, expanding the design flexibility and

enabling the fabrication of three-dimensional complex structures. This capability is particularly beneficial for various applications such as microelectromechanical systems (MEMS), microfluidics, and photonic integrated circuits, where intricate patterns and 3D structures are widely required.

When compared to other spatial light modulators such as liquid crystal on silicon (LCoS-SLM) [67] and microelectromechanical systems (MEMS) based deformable mirrors [68], DMDs chips exhibit superior capabilities in terms of speed and resolution. DMD chips can achieve high-speed and high-resolution light modulation, with the latest chips capable of modulating light at a speed of 5 kHz. In contrast, LCoS-SLM devices have a limited light modulating speed of only 200 Hz. While MEMS-based deformable mirrors can have a very high frame rate of 60 kHz, they typically have fewer light modulating pixels ranging from a hundred to a thousand. In terms of spatial resolutions, both DMDs and LCoS-SLM offer a significantly larger number of light modulating pixels [69].

2.5 Summery

In summary, optical waveguide-based optofluidic chip technologies have been reviewed in detail in this chapter. Firstly, optofluidic chips and their applications, including point-of-care testing, drug development & disease modelling, improve imaging resolution in microscope, cell operation and analysis, environmental monitoring etc., are introduced. Then, optical waveguide sensor-based optofluidic chip, i.e., a variety of devices combining optical waveguide sensor and microfluidic chips,

are introduced. Particularly, the most common optical waveguide sensors, i.e., MZI and MRR sensors, are described and their sensing mechanisms are discussed in details. Moreover, some typical fabrication techniques for optical waveguides have also been reviewed. DMD-based maskless lithography has been briefly introduced.

Chapter 3. Fabrication of polymer optical waveguides by digital ultraviolet lithography

3.1 Introduction

Because of its advantages of low cost, simple production, wide transparent window, polymer optical waveguides have attracted a lot of interest and have been widely employed in numerous fields, including photonic integrated circuits and optical label-free biosensors [70–77]. Polymer waveguides demonstrate remarkable vertical flexibility, offering exciting opportunities for effective refractive index modulation in the vertical direction and the advancement of 2.5D or 3D structures, such as multimode crossings based on Maxwell fisheye lenses [72–75]. Compatibility of polymer waveguides with different substrates and materials render them very appealing for hybrid integration of photonic devices, which can greatly expand their versatility and potential applications [76–78]. In the context of biosensors, polymer waveguides offer the capability of direct protein absorption and immobilization through covalent bonding on their surfaces. This unique feature enables optical waveguide structures to be easily modified for specific detection of biomolecules [31,77].

The most commonly used polymer materials for waveguide fabrication can be classified into: 1) non-photosensitive polymers (e.g., most polyimides [79] and polycarbonates [80]) and 2) photosensitive polymers (e.g., SU-8 [81]).

Various fabrication techniques have been employed for polymer waveguide production, including photolithography [36,82], LDW [83], and EBL [84]. Although conventional mask-based photolithography provides an efficient solution for fabrication of polymer waveguides in massive production, it lacks the flexibility in the fabrication of grayscale features and the ability of vertical integration. LDW and EBL offer greater flexibility, but they have low throughput resulting from their inherent single-spot scanning exposure nature. We will tackle these technological bottlenecks by developing a digital ultraviolet lithography (DUL) technology.

The DUL system utilized a high-speed spatial light modulator, i.e., DMD, with millions of pixels acting as a virtual dynamic mask, as explained in Chapter 2. It permits high-throughput all-digital production of intricately designed optical waveguides [60,69,85]. Each micro-mirror's state can be rapidly flipped by computer control using the pattern data generated from the designed 2D/3D structure. With this digital light processing technology, 3D microfabrication and grayscale exposure can be carried out [60,85].

To fabricate polymer optical waveguides that operate in a single mode, a maskless lithography system's resolution must be less than 2 μm . Researchers have made many efforts to raise the resolution of DMD-based lithography system. For instance, D. H. Lee presented an integrated maskless lithography optical system that consists of self-designed illumination part and projection lens part. It is verified that the system can reduce the resolution from 13.68 μm to 4 μm line width [86]. T. L. Laidig *et al.* improve resolution by introducing a 180-degree phase shift between adjacent

micro-mirrors [87]. K. Kim *et al.* presented flow lithography by using wobulation technique. An additional subpattern that shifted by half-pixel in diagonal direction of original pattern was generated. During exposure, the two patterns switched repeatedly for a short interval, accompanied by half-pixel shift of the motorized stage. By this way, the resolution of pattern can be increased and the edge of fabricated pattern will be smoothly [88].

This chapter presents the fabrication processes for high-quality polymer optical waveguides using a DUL system with high-resolution capabilities. The DUL system is based on a UV light-source (at the wavelength of 365 nm) and use a reduction projection optics with high magnification and a DMD with micromirror pitch of 7.6 μm . It indicates that the side length of mirrors is 7.6 μm . Methods for proximity effect compensation and stitching loss elimination are established. Experimental evaluations are conducted to fabricate various SU-8 optical waveguides, such as MMI splitters, Y-branch power splitters, and MRRs, to demonstrate the performance of the own-established DUL system.

3.2 Design of single-mode SU-8 optical waveguides

The structure of the SU-8 waveguide discussed in this chapter is depicted in Figure 3.1(a). To achieve strong light confinement with a small bending radius, a ridge waveguide structure is utilized. It consists of an air cladding and a 4- μm SiO₂ insulator on a silicon wafer, creating a significant refractive index contrast. The waveguide structure is designed and analysed using the finite difference eigenmode (FDE) solver

provided by the MODE Solutions of Lumerical Solutions Inc. The SU-8 waveguide has dimensions of 2.0 μm in height and 2.4 μm in width, enabling it to operate in

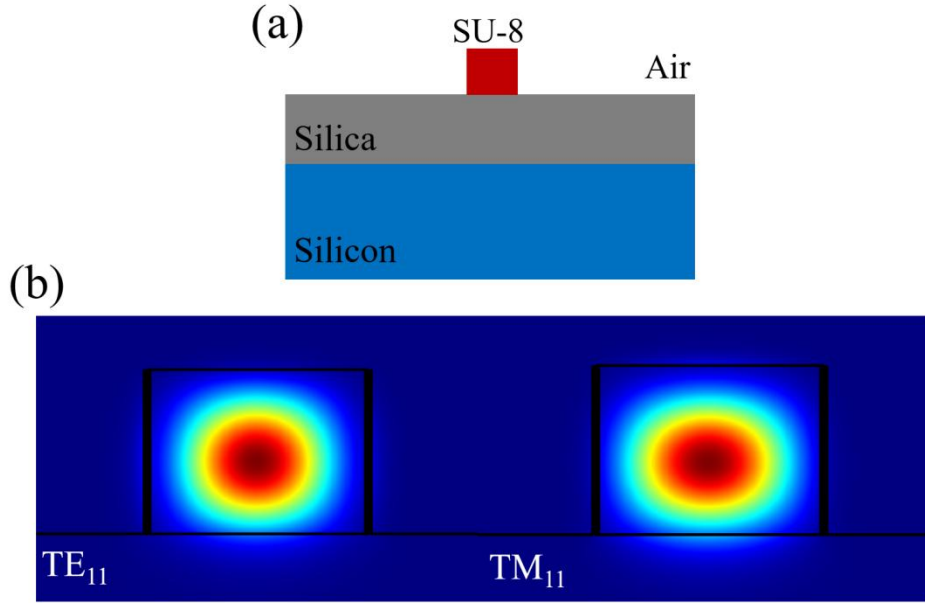


Figure 3.1 (a) Cross-section structure of SU-8 optical waveguide. (b) Calculated electrical field distributions of TE₁₁ and TM₁₁ modes of the presented waveguides.

single-mode conditions with low polarization dependence. Fig. 3.1(b) shows the calculated mode profiles, indicating support exclusively for the fundamental transverse electric (TE₁₁) and transverse magnetic (TM₁₁) modes.

Several types of polymer waveguide components based on SU-8 materials, including the MMI coupler, Y splitter, and MRR, are designed. The MMI was designed based on the self-image theory [89]. In the case of a 1 × N MMI splitter, the length of the core section (L_{MMI}) can be written [89]:

$$L_{MMI} = 3L_{\pi} / 4N = 3\pi / 4N(\beta_0 - \beta_1), \quad (3.1)$$

where L_π represents the beat length of the two lowest-order modes. N denotes the number of output waveguides, and β_0 and β_1 represent the propagation constants of the first and second order modes, respectively. And the separation between two output waveguides (W_{sp}) is determined by the equation [89]:

$$W_{sp} = (W + (\frac{\lambda}{\pi})(\frac{1}{n_r})^{2\sigma} (n_r^2 - 1^2)^{-1/2}) / N, \quad (3.2)$$

where W is the width of the MMI core. λ and n_r are wavelength and the refractive index of the waveguide, respectively. For TE mode, $\sigma = 0$ and for TM mode $\sigma = 1$. In our case, the width of the multimode interference (MMI) core is selected as $40 \mu\text{m}$ to ensure the excitation of an adequate number of modes and to achieve sufficient distance to separate two beams of power between the two output waveguides. An eigenmode expansion propagation (EME) solver provided by Lumerical Solutions Inc was applied to optimize the MMI coupler. Besides, the length of the MMI is $774.2 \mu\text{m}$, and the distance between the two output waveguides is $20.1 \mu\text{m}$. The 1×2 Y splitter consists of one input waveguide, two S-bends, and two output waveguides. To minimize bending loss and ensure sufficient separation between the two output waveguides, we choose the radius of the S-bends as $300 \mu\text{m}$.

To design a high performance MRR, we incorporate an MMI-like gapless coupler to reduce coupling length and increase fabrication tolerance [8,90]. Considering the bending loss, we choose a radius of $150 \mu\text{m}$ for the MRR.

3.3 Fabrication and optimization of the designed SU-8 optical waveguides

In the fabrication process of the designed waveguides, an own-built digital UV lithography system was employed. The system, as depicted in Fig 3.2(a), comprises a nano-precision motorized stage (ANT130-XY, Aerotech), projection optics, a high-power UV light-emitting diode (L10561-215, Hamamatsu Photonics), and a high-speed digital micromirror device (DMD) (DLP6500, Digital Light Innovations) [57,58,61]. The projection optics utilized in the system consist of two

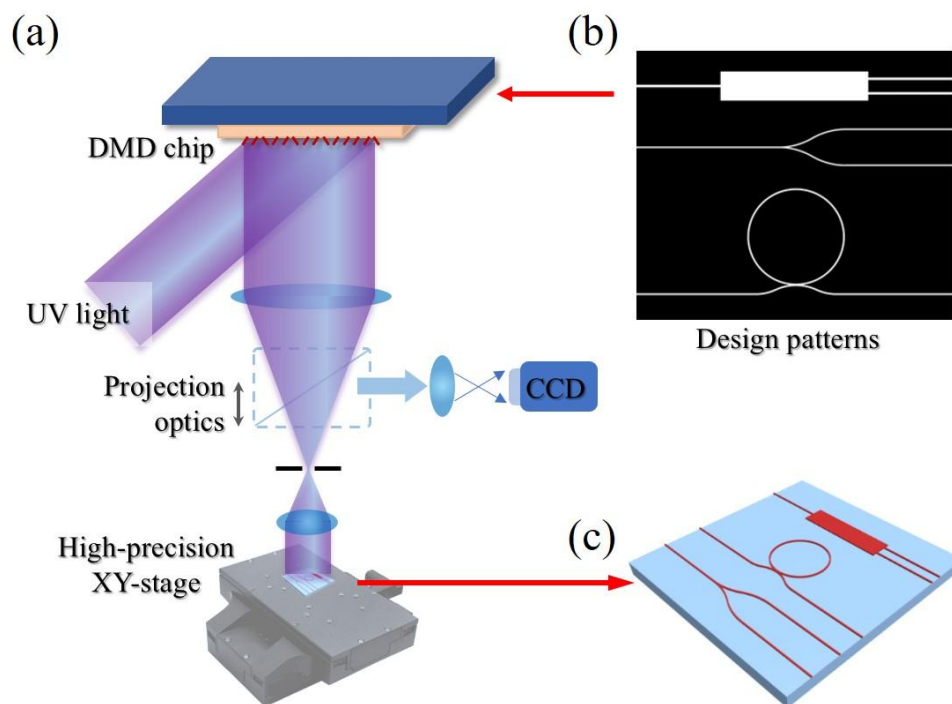


Figure 3.2 (a) Diagrammatic representation of the DUL system. (b) Grayscale bitmap depicting the engineered patterns functioning as a digital photomask. (c) Schematic illustration of waveguide structures with end-face termination.

lenses obtained from Thorlabs Inc. The lenses effectively reduce the separation

between two light pixels by approximately 300 nm . Additionally, a digital camera is integrated into the system to accurately determine the Z-position.

The waveguide patterns designed were transferred into 8-bit grayscale bitmaps and then uploaded to the DMD, which serves as a virtual mask (Figure 3.2(b)), during the optical exposure process. If assume that a grey value g can approximately represent the depth of light penetration in SU-8 during exposure, the overall exposure time t can be calculated according to the Beer Lambert law as [80]:

$$t = t_0 \exp(g / c_r), \quad (3.3)$$

where t_0 is the threshold of exposure time. The constant c_r depends on the ratio of the contents of photoinitiator to that of UV light absorber as well as the light intensity.

During the fabrication, a silicon wafer coated with a 4- μm SiO_2 oxide layer was utilized as the substrate. Prior to SU-8 coating, an adhesion promoter Omnicoat (Kayaku Advanced Materials, Inc.) was spun onto the wafer at the speed of 3000 rpm for 30s. The epoxy-based SU-8 2005 (Kayaku Advanced Materials, Inc.) was then spin coated for one minute at a speed of 4000 rpm. The thickness of the SU-8 layer was measured to be approximately 2.1 μm . A soft bake process at 65°C for 5 min and 95°C for 10 min was carried out. To transfer the designed patterns into the SU-8 layer, optical exposure was conducted with light intensity of 36.38 mW/cm². Then the samples were post-baked at 65°C for 15 min and 95°C for 30 min. Subsequently, the samples were developed in 1-Methoxy-2-propyl acetate (J&K Scientific Ltd.) for 2 min. Finally, hard baked the samples on a hotplate at 120 °C for 1 hour.

3.4 Optimization of the fabricated SU-8 optical waveguides

To fabricate high-quality low-loss SU-8 waveguide, the typical problems presenting in conventional lithography, such as proximity effect and stitching error, need carefully handled in the experiments. Here, we numerically pretreat pattern data and then tackle these problems by using a dynamic exposure scheme in exposure process.

3.4.1 Proximity effect compensation

Proximity effect during optical exposure will cause geometry deformation, leading to bad performance of the fabricated waveguides. For mitigating the consequences of the proximity effect, we employ a Gaussian-inspired distribution function to mathematically represent the scattered light intensity pattern emanating from individual pixels:

$$P(r)=P_0 e^{-2.773r^2/w^2}, \quad (3.4)$$

where P_0 is the peak intensity of the central position of the light pixel. P is the scattered light intensity of adjacent pixels, whose distance to the central pixel is r . Besides, w represents the full width at half maximum (FWHM) of the scattered light distribution, characterizing the spatial extent of the scattered light profile. Under the assumption of a uniform scattered distribution for each light pixel, the light intensity distribution of an entire pattern can be obtained by superposing the intensities of all neighbouring pixels. By changing the parameters of this distribution, one can adjust the intensities of pixels that were affected by increased scattering from neighbouring

light pixels to control the dynamic exposure for effectively compensating the proximity effect.

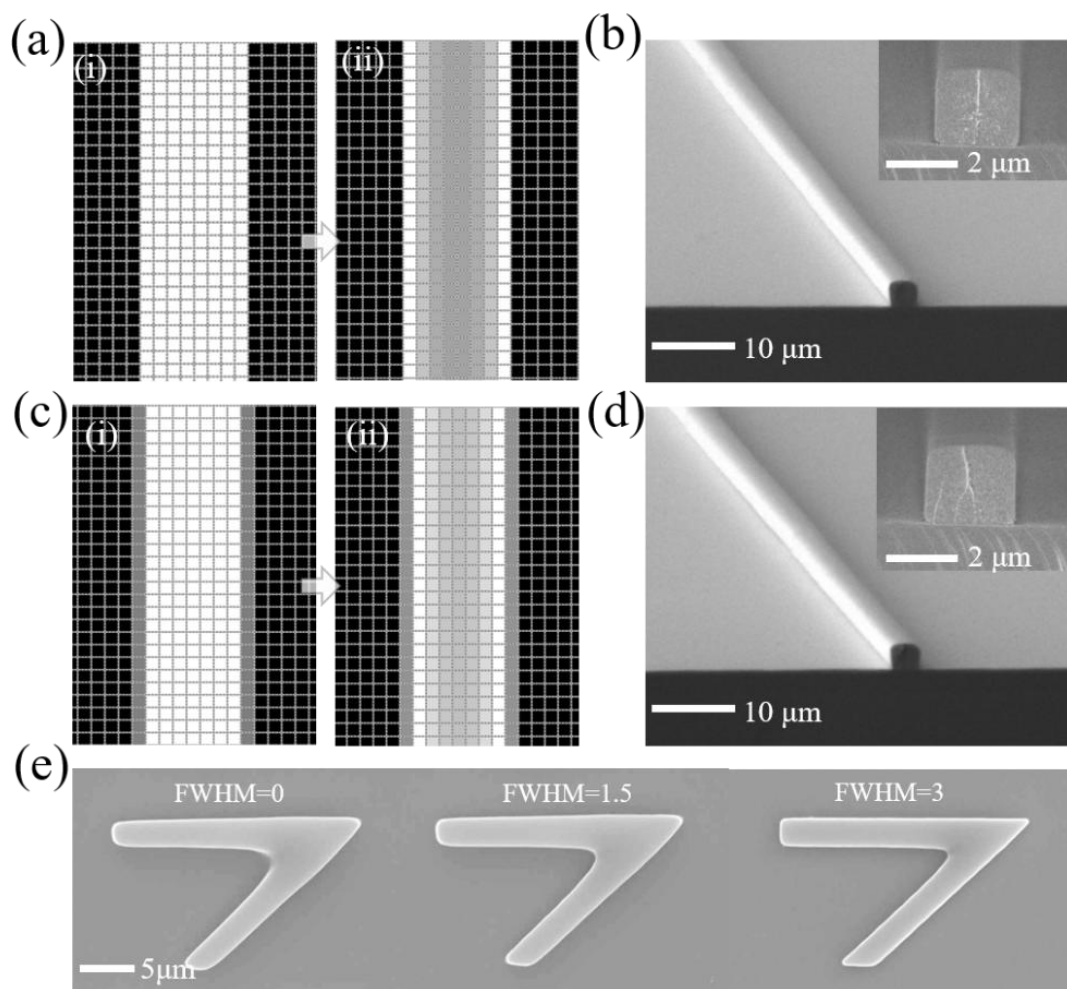


Figure 3.3 (a) The line pattern with an initial width of 8 pixels before (i) and after (ii) being corrected using a Gaussian-like light pixel distribution. (b) SEM images of the fabricated waveguide with pattern of 2.4- μm wide line. (c) A 9-pixel wide line pattern with half-maximum grey edge before (i) and after (ii) corrected with Gaussian-like light pixel distribution. (d) SEM images of the fabricated 2.4- μm wide line waveguide. (e) SEM images of the fabricated 45-degree angle patterns using different FWHM values.

Fig. 3.3(a) illustrates a line pattern that pretreated by proximity effect compensation function. It can be observed that the pixels at the edges of the waveguides possess higher grayscale values, while the pixels in the centre of the waveguides exhibit lower grayscale values for compensating the increased light intensity due to scattering. To optimize both the exposure time and the parameters of the exposure time threshold (t_0) and the full width at half maximum (FWHM, w) in Eqn. (3.4), exposure tests were conducted using a line pattern with a half-maximum grey edge (Figure 3.3(c)) and an angled line pattern. This approach aims to achieve optimal results in terms of exposure characteristics.

Fig. 3.3(b) and (d) present the SEM images of the fabricated line patterns, obtained with specific settings for the exposure time, threshold time (t_0), and full width at half maximum (FWHM). In the experiments, the exposure time was set to 18 s, the threshold time (t_0) was 1.8 s, and the full width at half maximum

(FWHM) was 3.0. These optimized parameters enabled the successful fabrication of line waveguides with a width of 2.4 μm for both the all-white 8-pixel wide line pattern and the 9-pixel wide line pattern with a half-maximum gray edge. In Fig. 3.3(e), the effects of different FWHM values (w) on the fabricated patterns are depicted. It can be observed that when the FWHM is set to 0, some residue resulting from the proximity effect is visible in inner corner. However, by increasing the FWHM to 3.0, a better result was achieved without obvious residue in inner corner, indicating successful compensation of the proximity effect. Notably if there are changes in the fabrication conditions, such as variations in chemical constituents,

photoresist thickness, or UV light intensity, these parameters including the total exposure time (t), threshold time (t_0) in Eqn. (3.3), and FWHM (w) in Eqn (3.4) need to be re-optimized to fabricate structures with minimized proximity effect.

3.4.2 Seamless stitching

Even though a DMD chip consists of millions of pixels, typically 1920×1080 pixels, the size of its optical image projected onto the substrate is approximately $572 \times 322 \mu\text{m}^2$ resulted from the utilization of reduction projection optics. Consequently, it is required to stitch multiple subpatterns together to fabricate practical optical waveguide devices with input/output elements. To reduce optical loss caused by stitching misalignment, transition zones were introduced between neighbouring subpatterns. In these transition zones, the grayscale values of the pixels were adjusted in a quadratic form to compensate for potential width differences resulting from separate exposures. Specifically, for a transition zone defined by the pixel positions from x_0 to x_1 , the grayscale values of the transition zone in two successive subpatterns are:

$$\begin{cases} g_f(x_l) = g_0(x_l)[1 - x_l + 4c(x_l - x_l^2)], \\ g_b(x_l) = g_0(x_l)[x_l + 4c(x_l - x_l^2)], \end{cases} \quad (3.5)$$

where g_f and g_b are the modified grayscale values of the first and the second subpatterns, respectively, g_0 is the original grayscale value of the designed pattern. The local pixel position is $x_l = (x - x_0) / (x_1 - x_0)$, c is compensation coefficient.

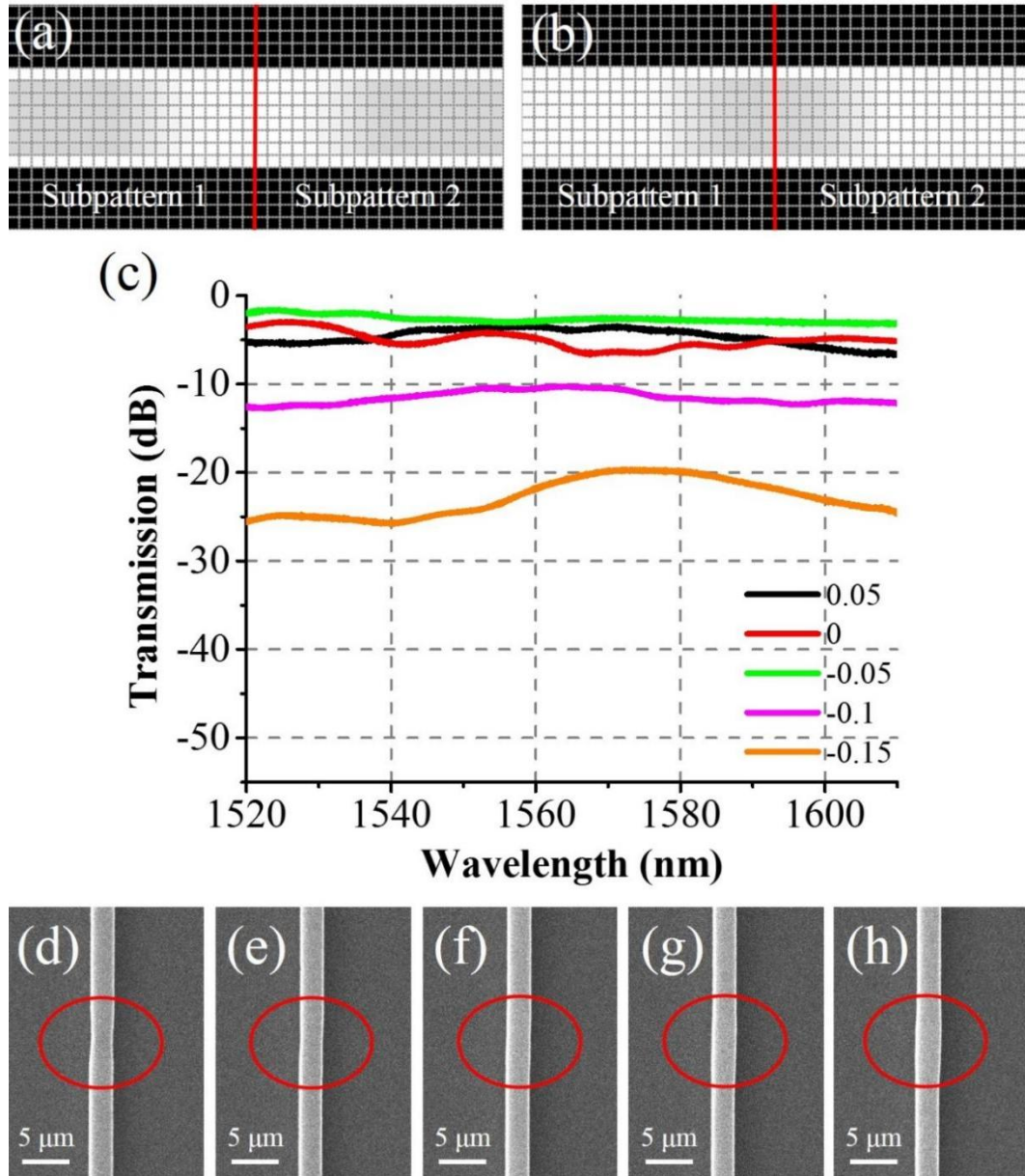


Figure 3.4 (a) Grayscale distribution maps of the stitching transition zones between two patterns when their compensation coefficients are positive. (b) Grayscale distribution maps of the stitching transition zones between two patterns when their compensation coefficients are negative. (c) Transmission spectra of the fabricated waveguides with various compensation coefficients. (d-h) SEM images of the stitching transition zone of the fabricated waveguides with various compensation coefficients of -0.15, -0.1, -0.05, 0, and 0.05, respectively.

Fig. 3.4(a) and (b) illustrate the grayscale images of the transition zone, showcasing the effects of compensation coefficients of 0.1 and -0.1, respectively. A positive compensation coefficient results in slightly brighter grayscale values around the abutting centre line, indicating an increased exposure dose through a longer exposure time. Conversely, a negative compensation coefficient produces smaller grayscale values around the abutting centre line, indicating a decreased exposure dose through a shorter exposure time. The grayscale values of the image have been normalized to a maximum of 255, enabling the creation of 8-bit bitmaps for the grayscale exposure process.

Fig. 3.4(c) displays the tested transmission spectra of the fabricated spliced waveguides, with varying compensation coefficients, i.e., -0.15, -0.1, -0.05, 0, and 0.05. The SEM images of the stitched transition zones can be observed in Fig. 4(d)-(h), corresponding to each compensation coefficient, respectively. The experimental results demonstrate that a negative compensation coefficient leads to a thinner waveguide at the stitching region, resulting in increased waveguide loss. Conversely, when the compensation coefficient is 0.05 or higher, the waveguide at the stitching region slightly widens, also leading to increased waveguide loss. In the range between -0.05 and 0, no observable stitching trace is present, and the fabricated waveguide exhibits relatively low loss.

It is worth noting that the optimal fabrication parameters mentioned above are reliant on the specific configuration of the DUL system, which encompasses factors such as the types of UV source, DMD, and projection optics, as well as the chemical

composition and thickness of the SU-8 layer. Therefore, in the event of any modifications to the system configuration or the SU-8 layer, it is necessary to repeat the optimization procedure outlined earlier to determine new optimal parameters.

3.5 Characterization of the fabricated SU-8 optical waveguides

To characterize the fabricated waveguides, the waveguide chip was tested by using edge coupling by cutting it on both sides, as shown in Fig. 3.2(c). The transmission spectra of the fabricated waveguides were measured using a broadband light source covering the range of 1480-1600 nm, along with an optical spectrum analyser (OSA) model Yokogawa AQ6370D.

3.5.1 Bending loss measurement

To determine suitable radii for bend waveguides like MRRs, we fabricated and characterized S-bends with different radii. The waveguide dimensions, including height and width, were maintained at 2.1 μm and 2.4 μm , respectively. Every waveguide had eighteen parts that formed a 90° arc and had a predetermined bending radius. Figs. 3.5(a) and (b) display bend waveguides that have been built with radii of 75 μm and 100 μm , respectively. Fig. 3.5(c) displays the tested transmission spectra of the bent waveguides with varying radii, i.e., 75 μm , 100 μm , 125 μm , 150 μm , and 175 μm . To eliminate the impact of coupling loss and propagation loss, the transmission spectra underwent normalization in relation to a similar-length straight waveguide. Minor ripples in the measured transmission spectra may be caused by surface

reflections between the constructed waveguide and the lensed optical fibre [92], or by reflections from micro-particles incorporated into the construction process.

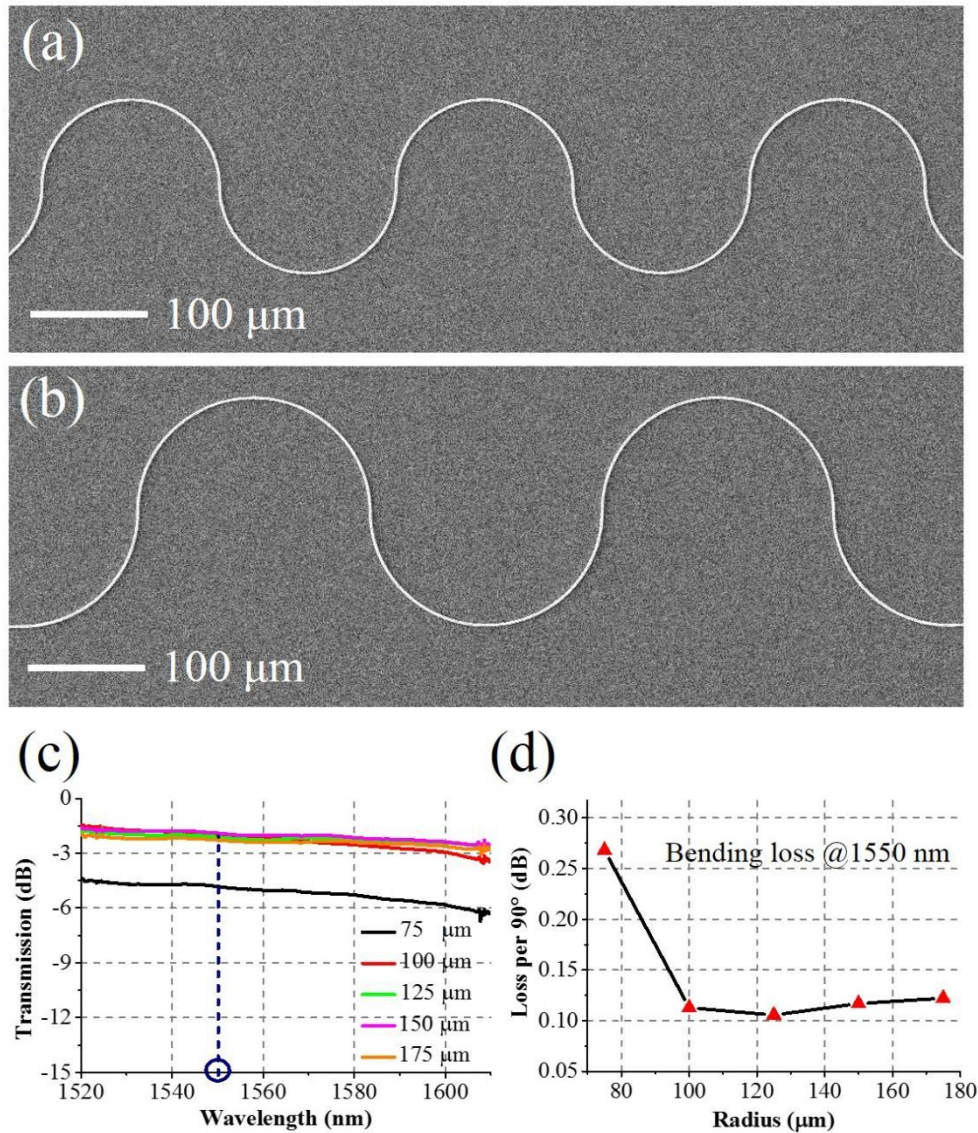


Figure 3.5 (a) SEM images of the fabricated waveguides with bending radius of 75 μm. (b) SEM images of the fabricated waveguides with bending radius of 100 μm. (c) Tested transmission spectra of the fabricated waveguides with varying bending radii. (d) Extracted dependence relation of the loss on bending radius at the wavelength of 1550 nm.

The appearance of these modest spectral peaks or ripples at different wavelengths can be explained to minor differences in the relative locations and light reflection routes between the optical fibre and the waveguide facet during various tests. Furthermore, the light reflection routes can differ amongst the particles inserted during the production process. Fig. 3.5(d) shows the normalized bending loss for each 90°-arc waveguide section at 1550 nm. When the radius exceeds 100 μm , the results show a minimal bending loss (~ 0.1 dB/90°). This degree of bending loss is comparable to what can be obtained using classic photolithography processes [93]. Based on these findings, a radius of 150 μm was chosen for bend waveguides such as MRR or spiral waveguides in order to minimize bending loss during the experiments.

3.5.2 Propagation loss measurement

The relatively high propagation loss observed is primarily attributed to scattering caused by minute particles or impurities that adhere to or are mixed within the waveguides. It is important to note that the fabrication processes were not carried out in a cleanroom environment, rather than due to sidewall roughness. With an optical resolution of approximately 298 nm, our DUL system allows for the fabrication of waveguides with a width of 2.4 μm . To achieve this, the designed waveguide patterns have a width of 8 pixels, which ensures the generation of smooth boundaries through the utilization of an 8-bit grayscale exposure technique.

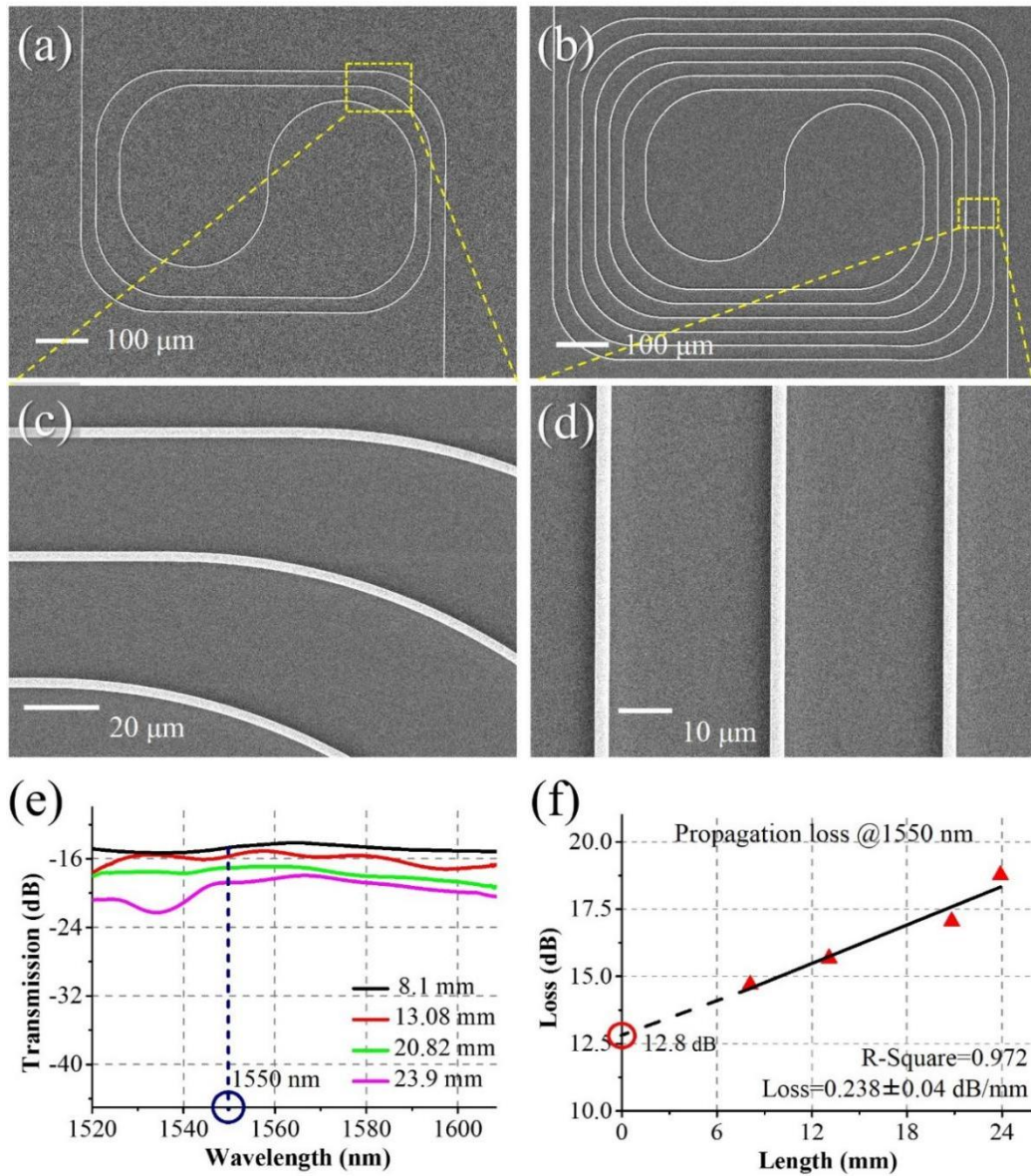


Figure 3.6 (a) SEM images of fabricated spiral waveguides with length of 12.2 mm. (b) SEM images of the fabricated spiral waveguides with length of 23.3 mm. (c) and (d) are the enlarged images of (a) and (b) at two different positions, respectively. (e) Tested transmission spectra of the fabricated waveguides with different lengths of 8.1 mm, 13.08 mm, 20.82 mm, 23.9 mm, respectively. (f) Dependence of propagation loss on waveguide length at the wavelength of 1550 nm.

Fig. 3.6(a) and (b) display the SEM images of the fabricated spiral waveguides with varying lengths. Enlarged images at different positions can be seen in Fig. 3.6(c) and (d), respectively. The measured transmission spectra of the waveguides with varying lengths of 8.1 mm, 13.1 mm, 20.8 mm, and 23.9 mm are presented in Fig. 3.6(e). Extracted from Fig. 3.6(e), Fig. 3.6(f) shows the measured losses at the wavelength of 1550 nm. It can be observed that the measured loss increases linearly with the length of the waveguide. From this linear relationship, the propagation loss at the wavelength of 1550 nm can be deduced to be approximately 0.238 dB/mm. In addition to the transmission loss, other factors such as edge coupling loss contribute to the overall loss. By setting the waveguide length to 0 on the linear regression line, the calculated edge coupling loss was determined to be 12.8 dB. The propagation loss observed in our fabricated waveguides is comparable to that of SU-8 waveguides produced through conventional lithography techniques [93–95]. The relatively high propagation loss in our fabricated waveguides can be primarily attributed to scattering loss caused by small particles or impurities that adhere to or are present within the waveguides. It is important to note that all fabrication processes were not conducted in a cleanroom environment. The sidewall roughness does not significantly contribute to the observed propagation loss.

In our DUL system, the optical resolution is approximately 298 nm. Consequently, to fabricate 2.4- μm waveguides, the designed patterns should have a width of 8 pixels. Such a number of pixels is sufficient to achieve a smooth boundary using the 8-bit grayscale exposure technique.

3.6 Characterization of MMI, Y-Branch Splitter and MRR

To validate the capabilities of the DUL system in fabricating SU-8 waveguide devices, various waveguide components were manufactured and tested. Among these components, two types of power splitters, namely MMI coupler and Y-branch, were

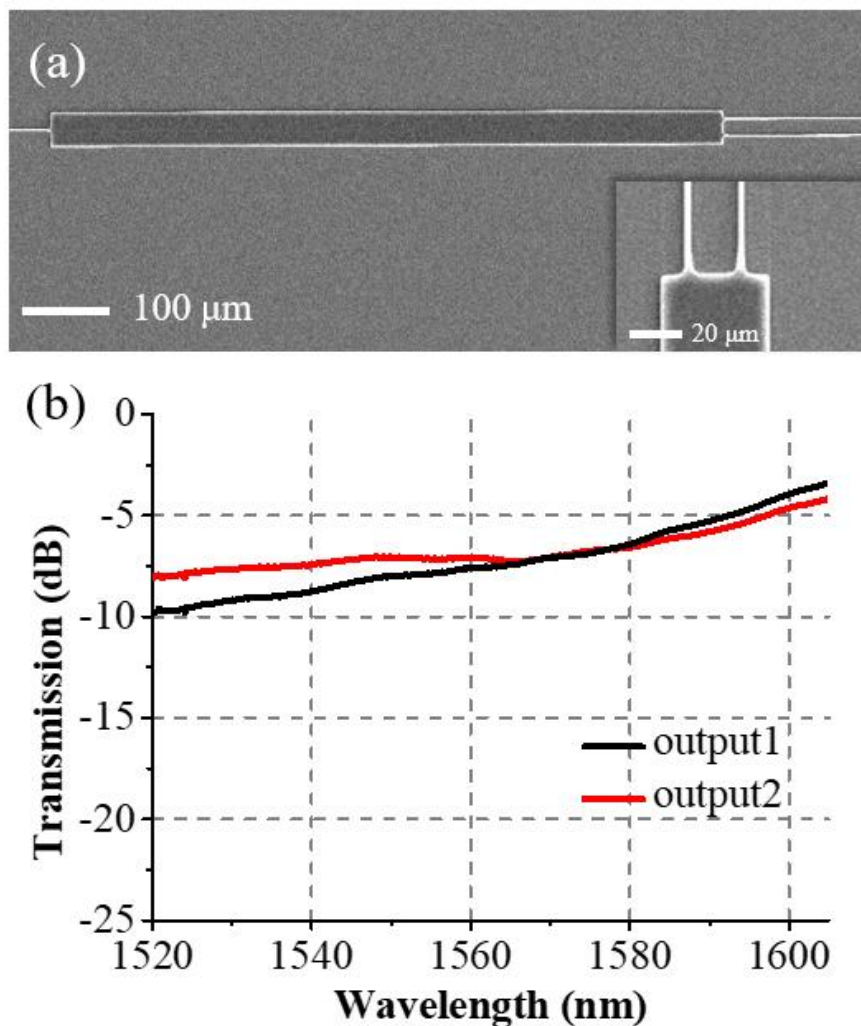


Figure 3.7 (a) SEM photograph of the fabricated MMI power splitter. (b) Normalized transmission spectra of the fabricated MMI power splitter.

fabricated and subjected to characterization.

Fig. 3.7(a) shows an SEM image of a manufactured MMI coupler. Fig. 7(b) shows the measured transmission spectra, which were normalized and acquired from the two output ports. The symmetrical MMI power splitter provides effective power distribution over a wide wavelength range of 1520 nm to 1610 nm. The transmission spectra show power fluctuations of 6.5 and 4.0 dB, respectively. The additional loss found in the manufactured MMI coupler is mostly due to scattering at the connections

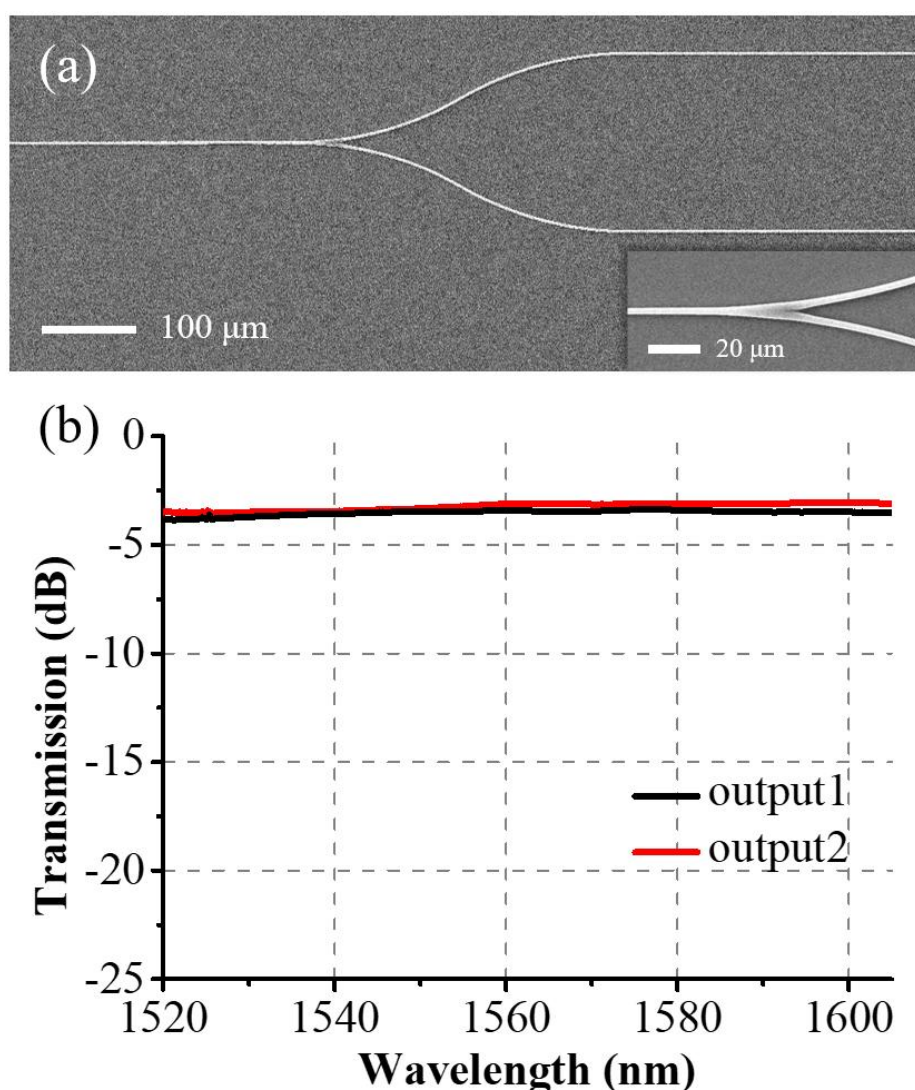


Figure 3.8 (a) SEM photograph of the fabricated Y-branch power splitter. (b) Normalized transmission spectra of the fabricated Y-branch power splitter.

of the MMI core area and the access waveguides. Additionally, shallow ripples appearing in the transmission spectra may result from the interference of light waves reflected by the end surfaces of the coupling fibre and waveguide.

A fabricated 1×2 Y-branch power splitter with one input waveguide and two output waveguides with S-bends is depicted in the SEM picture in Fig. 3.7(c). A 300 μm radius was used in the design of the S-bends to reduce bending loss and give enough room between the two branching waveguides. The Y-branch junction may be seen in greater detail in the inset of Fig. 3.7(c). Fig. 3.7(d) shows the measured normalized transmission spectra of the Y-branch power splitter. Within the measurement range, the two output ports' spectra are quite similar to one another and barely depend on the waveguide. Over the wavelength range of 1520 nm to 1610 nm, the output power differential is 0.15 dB at 1550 nm and does not exceed 0.36 dB. A manufactured 1×2 Y-branch power splitter with one input waveguide and two output waveguides with S-bends is depicted in the SEM picture in Fig. 3.7(c). A 300 μm radius was used in the design of the S-bends to reduce bending loss and give enough room between the two branching waveguides. The Y-branch junction may be seen in greater detail in the inset of Fig. 3.7(c). Fig. 3.7(d) shows the measured normalized transmission spectra of the Y-branch power splitter. Within the measurement range, the two output ports' spectra are quite similar to one another and barely depend on the waveguide. Over the wavelength range of 1520 nm to 1610 nm, the output power differential is 0.15 dB at 1550 nm and does not exceed 0.36 dB.

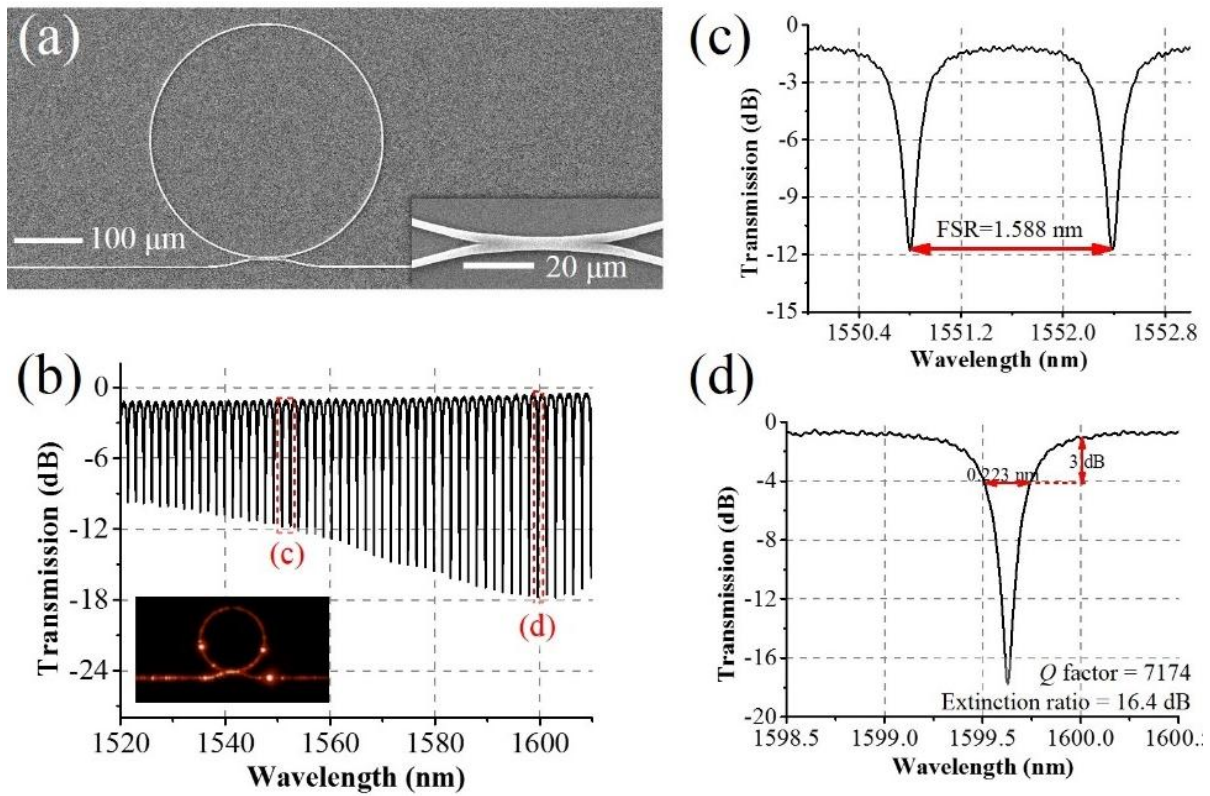


Figure 3.9 (a) SEM image of a fabricated waveguide MRR. (b) Measured normalized transmission spectrum of the MRR. (c) and (d) enlarged part of transmission spectra at the wavelengths around 1551 nm and 1600 nm, respectively.

Furthermore, an MRR with a gapless coupling part was fabricated, as depicted in Fig. 3.9(a). The MRR ring had a radius of $150\ \mu\text{m}$. The measured transmission spectrum of the MRR, spanning from 1520 nm to 1610 nm, is shown in Fig. 3.9(b). The enlarged figures of the spectra at wavelengths near 1551 nm and 1600 nm are provided in Fig. 3.9(c) and (d), respectively. Fig. 3.9(c) illustrates that the free spectral range (FSR) near 1551 nm is approximately 1.588 nm, closely matching the simulated value of 1.575 nm. The MRR exhibits a high Q factor, with the highest value of 7174

corresponding to the transmission dip at a wavelength of 1600 nm. Additionally, the extinction ratio at this wavelength is 16.4 dB.

3.7 Summary

In summary, we have presented a new fabrication process utilizing a DMD-based DUL system for the fabrication of SU-8 optical waveguides. This process offers improved flexibility compared to traditional optical lithography, while it provides higher productivity compared to E-beam lithography and laser direct writing technologies. A numerical pre-estimation of light scattering effects was employed to harness grey-scale exposure for mitigating light scattering and reducing proximity effects. Additionally, a grayscale exposure method was demonstrated to seamlessly stitch patterns together, enabling the creation of large-area, high-quality waveguide devices.

According to the experimental findings, when the bending radius was greater than 100 μm , the manufactured waveguides displayed bending loss < 0.1 dB/90°-arc. At a wavelength of 1550 nm, the propagation loss was measured at 0.238 dB/mm. Moreover, uniform power splitting was shown by the manufactured MMI and Y-branch power splitters throughout a wide wavelength range of 1500 nm to 1600 nm. The fabricated MRR demonstrated an extinction ratio of roughly 16 dB and a high Q factor that was more than 7100.

It is anticipated that the technique of grayscale and dynamic optical exposure will be very beneficial for creating waveguides with 2.5D and even 3D features, like multimode crossings based on Maxwell fisheye. The development of intelligent

adaptive lithography technology could be further enabled by integration with machine vision technologies, which would facilitate the fabrication of innovative waveguide devices.

Chapter 4. Optofluidic chip with directly printed polymer optical waveguide Mach-Zehnder interferometer sensors

4.1 Introduction

Improvement of healthcare services for patient-centred outcomes has become increasingly important nowadays [14,96–98]. There is an increasing demand to develop low-cost biomedical diagnostic devices that may be utilized on daily basis and have a wide range of uses, particularly in response to public health emergencies. Lateral flow immunoassay (LFIA) approaches are currently one of the most used technologies for point-of-care diagnostics. LFIA procedures are popular because they are simple to implement and require little time to analyse [99–102]. Nonetheless, when compared to laboratory-based immunochemical approaches, LFIA techniques have limitations in terms of sensitivity and specificity, yielding primarily qualitative data. To address these restrictions, lab-on-a-chip (LoC) devices have emerged as a promising solution. These devices combine numerous microscale components to enable multiple processes on a chip. Among the various types of LoC devices, integrated optofluidic chips have received a lot of attention mainly due to their high sensitivity in biodetection.

Integrated optofluidic chips are devices fusing microfluidic and photonic microsensors. First, they take advantage of the multiplicity of interactions between

light and matter to improve detection powers. The application of lightwave technology in these chips improves biodetection efficacy by increasing sensitivity and signal-to-noise ratio. Thus, integrated optofluidic chips are seen as a very promising way to achieve biodetection with great sensitivity [9,22,103,104]. An example of the potential of integrated optofluidic chips for biodetection was demonstrated in a study by Q. Liu *et al.* They developed a two-procedure sample-to-answer device that incorporated silicon MZI sensors and a sample pretreatment unit. This device was specifically designed for the detection of malaria parasites [13]. In another notable study, X. Ouyang *et al.* fabricated an optofluidic chip that includes polymer whispering gallery mode (WGM) microlaser sensors for enzyme-linked immunosorbent assay (ELISA). This new chip showed extraordinary sensitivity, capable of detecting vascular endothelial growth factor (VEGF) at 17.8 fg/mL [66].

In particular, because of their flexible on-chip integration, optical waveguide-based photonic sensors have significant promise for integrated optofluidic systems [9,105]. They can provide low propagation loss and effective confinement of light waves within a strip or rib. This feature allows for the integration of micro-interferometers or micro-resonators, which use lightwave technology to provide highly sensitive biosensing capabilities. The well-defined structures within the waveguide allow for interference or resonance, while the evanescent field of the light wave facilitates interaction with target molecules in the surrounding medium [106–108]. MZI micro-sensors are extensively employed in bio-detection applications. Patricia *et al.* introduced a POC device for tuberculosis detection based

on MZI sensors. They developed a photonic device with several Si₄N₃ MZI sensors incorporated inside a disposable microfluidic cartridge. This approach permitted the simultaneous detection of several disease biomarkers. The device successfully detected tuberculosis in undiluted urine samples at a concentration level as low as 0.475 µg/mL, and the turnaround time was within 15 minutes [109]. Densmore *et al.* displayed a Si photonic MZI biosensor array for detecting of two biomarkers simultaneously. Their findings revealed that the fabricated MZI sensor-device can successfully detect two proteins, i.e., rabbit IgG and goat IgG, in parallel. The detection ability that measured upon surface coverage was impressively below 0.3 pg/mm². This highlights the high sensitivity and potential of the MZI biosensor array for multiplexed biomarker detection [101]. Angelopoulou *et al.* presented an advanced optofluidic chip based on ten Si MZI sensors and a sophisticated microfluidic unit. This chip enabled the measurement of four allergens simultaneously. They are bovine milk protein, peanut protein, soy protein, and gliadin. The analysis process was remarkably fast, with a completion time of only 6.5 minutes. The chip exhibited exceptional sensitivity, with limits of detection measured at 0.04 µg/mL, 1.0 µg/mL, 0.80 µg/mL, and 0.10 µg/mL for the respective allergens [110].

Polymer materials offer numerous advantages, including ease of manufacturing, excellent biocompatibility, and the ability to be easily modified. These characteristics make them highly attractive for the development of biomedical instruments and sensors. Bruck *et al.* presented a polymer MZI waveguide biochip as a notable example. The biochip employed polyimide and Ormoclاد materials for the core and

cladding of the polymer optical waveguide. Remarkably, this MZI waveguide sensor demonstrated the ability to accurately measure streptavidin at a concentration as low as 100 pg/mL [111]. AZUELOS *et al.* demonstrated a highly sensitive MZI biosensor based on SU-8 epoxy. To enhance its sensitivity, they introduced an additional ring resonator, leveraging the vernier effect. This innovative biosensor achieved a remarkable bulk sensitivity of 17558 nm/RIU and showed an impressive limit of detection down to 1.1×10^{-6} RIU [112].

To construct high-quality optical waveguide sensors, many fabrication methods can be employed, such as optical lithography [81], LDW [83], or EBL technologies [84]. While conventional optical lithography is efficient for polymer optical waveguide fabrication, it relies on beforehand photomasks and is short of grey-scale exposure capability. LDW and EBL can partially overcome these limitations but are generally less efficient because of their single-spot scanning

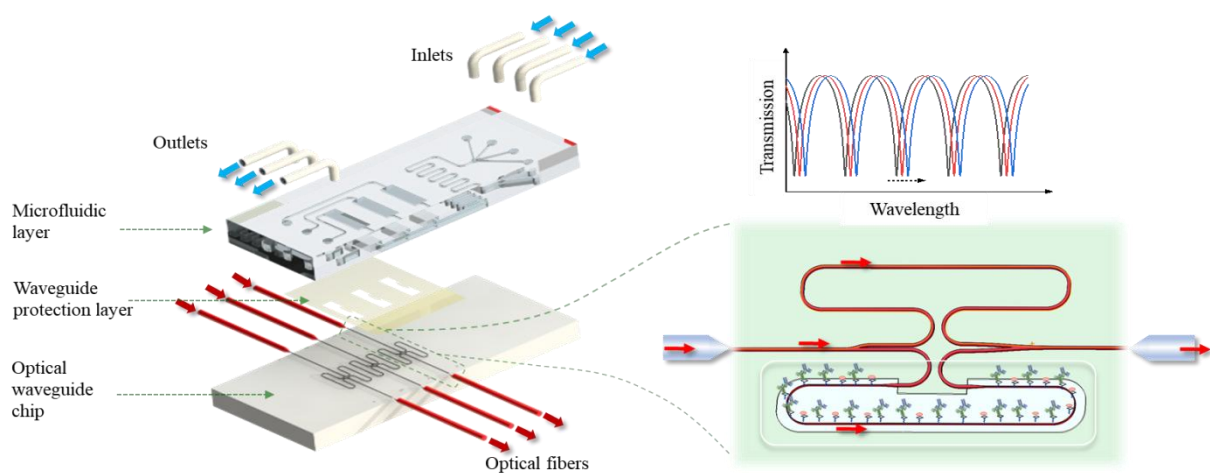


Figure 4.1 The design of an optofluidic chip with several directly printed polymer optical waveguide MZ micro-interferometer sensors.

methodology.

In this chapter, we develop an optofluidic biochip that embedded with polymer optical waveguide MZI sensors for the label-free detection of disease biomarkers, which is critical in modern medical diagnostics for determining health, sickness, or vaccination status. As shown in Fig. 4.1, we use our unique DUL technology [63,66,113] to directly print an asymmetric MZI microsensor imbedded with a width-tailored optical waveguide onto a SiO₂/Si wafer, allowing for on-chip biosensing. In addition, a PDMS-based microfluidic layer is produced utilizing DUL-based technology to package the optical waveguide chip into an optofluidic chip. The experimental results show that the manufactured optofluidic biochips have outstanding bulk sensitivity, detecting human immunoglobulin G (HIgG) at concentrations as low as 1.78 pM. Furthermore, the results demonstrate the optofluidic chip's reusability, allowing for multiple biomarker detections.

4.2 Fabrication of SU-8 optical waveguide and optofluidic chip

The fabrication of the polymer optical waveguide sensors was accomplished using a self-developed digital ultraviolet lithography (DUL) system. This system was constructed with key components, including a high-power UV light-emitting diode (L10561-215, Hamamatsu Photonics, Japan), a high-speed digital micromirror device (DMD; DLP6500, Digital Light Innovations, USA), a nano-precision motorized stage (ANT130-XY, Aerotech Inc., USA), and a set of projection optics.

4.2.1 Fabrication of SU-8 optical waveguide Mach-Zehnder interferometer sensors

The fabrication of the designed waveguide involved using a commercial SU-8 photoresist on a SiO₂/Si wafer. Fig. 4.2 shows the flow chart of fabrication procedure. The adhesion promoter Omnicoat was applied before coating the SU-8. Then SU-8 was then spun onto the silicon wafer at a speed of 5000 rpm for 30 seconds. To get rid of the solvent, a gentle bake was done for five minutes at 65 °C and ten minutes at 95 °C. After prebaking, a grayscale pattern was dynamically projected onto the photoresist using the DUL system. In less than twenty minutes, a MZI pattern with dimensions of 22 mm by 4 mm was exposed. A post-bake was then done for five minutes at 65 °C and for thirty minutes at 95 °C. After that, the sample was developed for two minutes using PGMEA. To further increase the crosslinking degree of SU-8 waveguide structure, a hard bake was finally performed at 120 °C for 60 minutes. Both the post-bake and hard bake were ended by gradual cooling for relieving the internal residual tension.

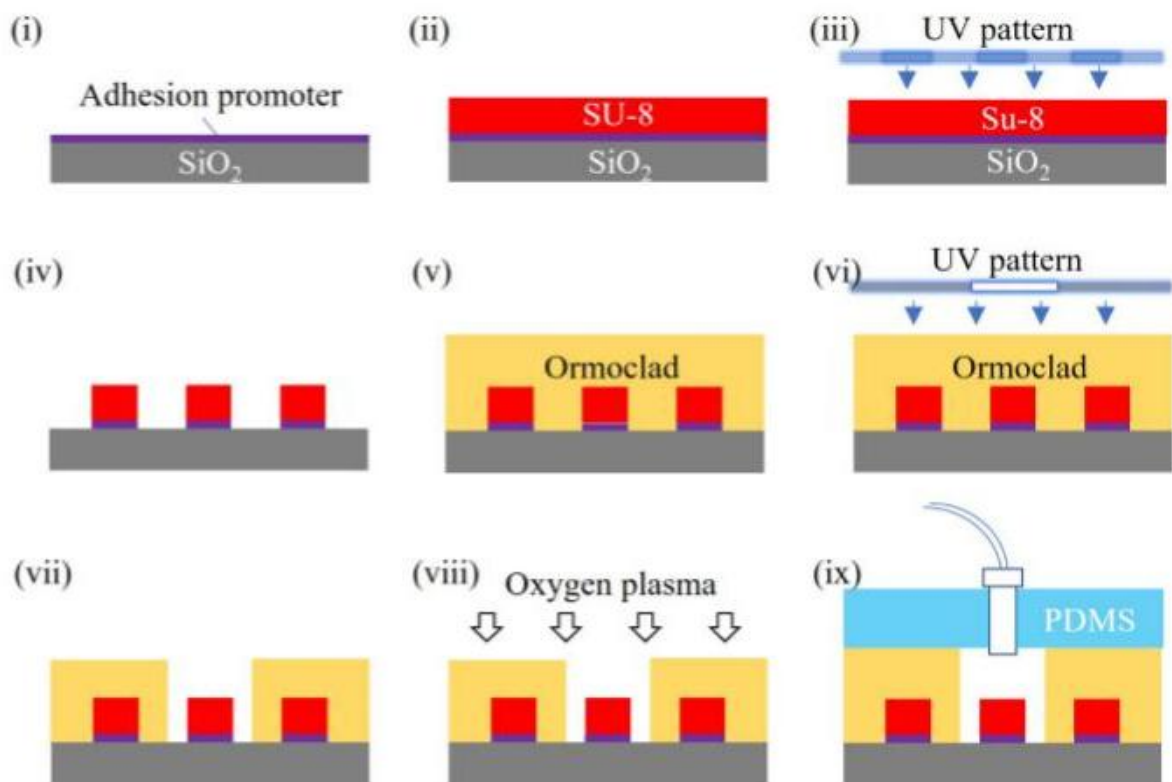


Figure 4.2 Flow chart of the processes used in the fabrication of an integrated optofluidic chip

Another commercial photoresist known as Ormoclad was used to build a cladding layer. A PLUTO-T Plasma Cleaner (PLUTOVAC, Shanghai, China) powered by 200 W was used for the five-minute plasma treatment. The flow rate was kept at 100 mL/min and the air pressure was adjusted to 24.4 Pa. Ormoclad was then spun onto the prototype SU-8 waveguide sample. The cladding layer was formed by carefully exposing the Ormoclad over the optical waveguide using the overlay exposure function of the DUL system. On purpose, a window was left open on the optofluidic

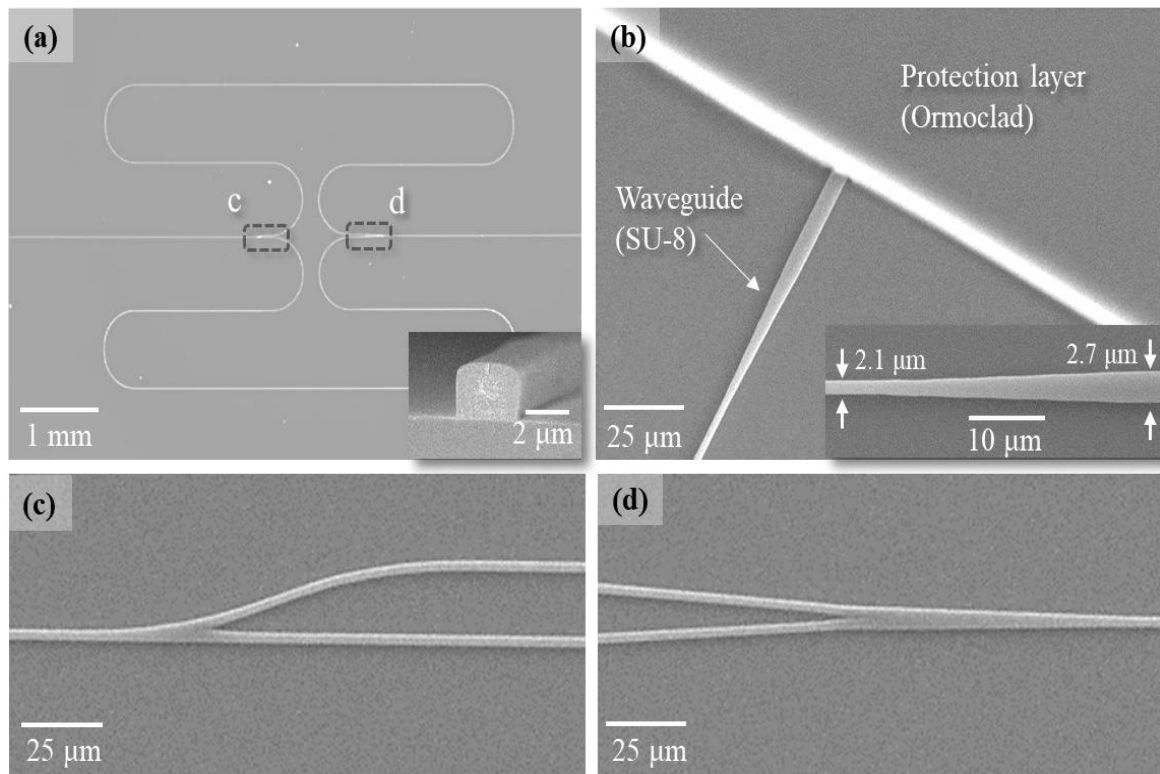


Figure 4.3 (a) Optical microscope image of the fabricated waveguide MZI sensor. The inset is a cross-section of waveguide, (b) SEM image of waveguide partially covered by Ormoclad. The inset is close-up of the tapered waveguide. (c) SEM image of the fabricated 1:2 waveguide splitter. (d) SEM image of the fabricated 1:1 waveguide combiner.

biosensing arm.

A 90- μm transition zone was inserted during the exposure of each sub-pattern in order to lessen the problem ofOrmoclad shrinking. After a 15-minute post-bake at 130 °C, the sample was developed for 90 seconds with methyl isobutyl ketone (MIBK). Ultimately, the optical waveguide chip underwent 180 minutes of rigorous baking at 150 °C.

The SU-8 waveguide MZI sensors, depicted in Fig. 4.3(a)-(d), were fabricated using carefully selected materials. The core and the upper cladding of the optical waveguide were made from SU-8 and Ormoclad, whose refractive index are 1.573 [114] and 1.52 [115] respectively. The substrate material was SiO_2 ($n=1.45$). To achieve optimal performance, the dimensions of the SU-8 waveguide, excluding the sensing part, were chosen as 2 μm in height and 2.7 μm in width, which showed in the inset of Fig. 4.3(a). This dimension selection allowed the waveguide to operate in a single-mode condition while keeping the evanescent field relatively weak, effectively minimizing optical loss caused by the direct printing processes used to fabricate the Ormoclad cladding. The Ormoclad cladding layer is controlled to be about 10 μm , which is thick enough to protect the SU-8 waveguide from changes in upper environment.

To improve sensitivity, the width of the sensing arm in the optical waveguide was reduced to 2.1 μm , as depicted in the inset of Fig. 4.3(b). This narrower width enhanced the evanescent field of the waveguide, leading to better sensitivity.

Numerical simulation results, as shown in Fig. 4.4, indicate that the evanescent field of the fundamental guided mode in the SU-8 waveguide design can extend approximately 744 nm into the surrounding water environment. This range is adequate for capturing a majority of biomarkers in various biological detection applications.

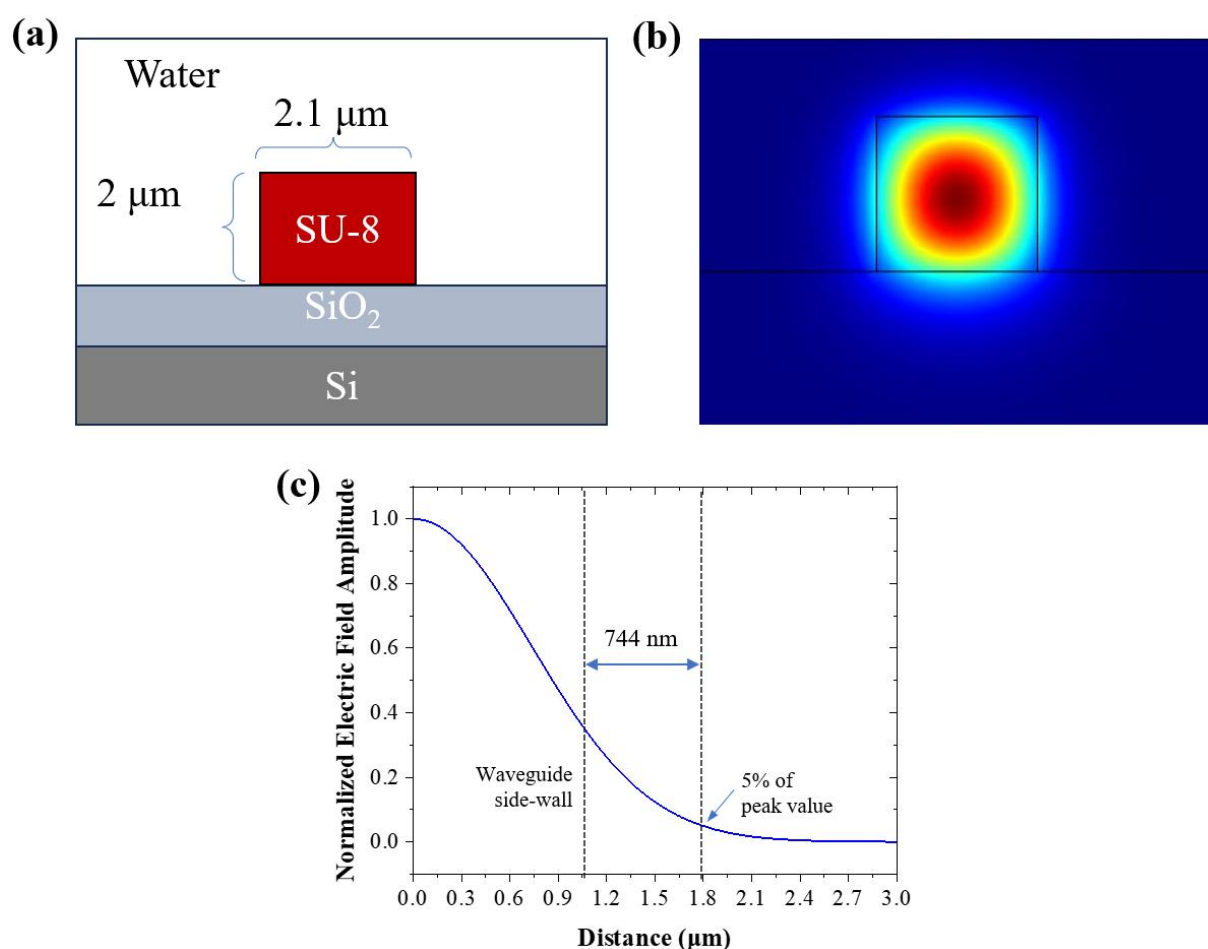


Figure 4.4 (a) Structure of the cross-section of designed SU-8 waveguide. (b) Calculated electrical field distributions of fundamental mode of the designed waveguides. (c) Simulated electric field distributions of the waveguide.

To minimize optical propagation losses caused by mode-mismatch, a 50-μm adiabatic taper (Fig. 4.3(b)) is introduced between the waveguides of different widths.

This adiabatic taper ensures a smooth transition of light waves, reducing losses in the system. Considering a narrower waveguide in the sensing arm, optical losses will be higher compared with reference arms. The first Y-splitter of the optical waveguide MZI is specifically designed with an asymmetric output. This design compensates for the power difference between the light waves transmitted through the sensing and reference arms. Consequently, the light waves propagate through their respective arms and converge at the output Y combiner, where they interfere with each other to produce the desired output signal.

In the presence of analytes, the effective refractive index of the optical modes within the sensing arm varies depending on their concentration. This variation in refractive index leads to a corresponding change in the optical phase of the light wave passing through the sensing arm. Using a spectral dip in the transmission spectrum as the output signal, the wavelength shift ($\Delta\lambda$) may reliably quantify the change in refractive index within the sensor arm's working section. This optical phase modulation technique enables precise detection and quantification of analyte concentration in the surrounding liquid medium [112,116]:

$$\Delta\lambda = \frac{\lambda\tilde{L}_1\Delta n_{e1}}{n_{g2}\tilde{L}_1 + n_{g1}\tilde{L}_1 - n_{g2}L_2} \quad (4.1)$$

where \tilde{L}_1 , Δn_{e1} , and n_{g1} represent the length, the induced variation of effective refractive index, and the group refractive index of the sensing arm with 2.1- μm width, respectively; n_{g2} corresponds to the group refractive index of the waveguide with 2.7- μm width, which includes the embedded part of the sensing arm and the reference

arm; Additionally, \bar{L}_1 and L_2 represent the lengths of the embedded part of the sensing arm and the reference arm, respectively.

The measurement range of the waveguide MZI sensor is determined by the FSR:

$$FSR = \frac{\lambda^2}{|n_{g2}\bar{L}_1 + n_{g1}\tilde{L}_1 - n_{g2}L_2|} \quad (4.2)$$

Considering influences of the surrounding medium's refractive index on the effective refractive index of the working part of the sensing arm, denoted as $\partial n_{e1}/\partial n_{ext}$, the bulk sensitivity (S) of the device can be expressed as:

$$S = \frac{FSR \cdot \tilde{L}_1}{\lambda} \cdot \frac{\partial n_{e1}}{\partial n_{ext}}, \quad (4.3)$$

where n_{ext} is the refractive index of the surrounding medium of the sensor arm's working portion. The working section, embedded section (L_1 and ΔL_2), and reference arm (L_2) lengths of our MZI sensor design are precisely selected to be 10.636 mm, 3.410 mm, and 13.918 mm, respectively. Theoretical calculation shows that the narrow sensing waveguide (2.1- μm width) in water (n_{g1}) and the wide waveguide (2.7- μm width) embedded in Ormoclاد have the group refractive indices (n_{g2}) of 1.6028 and 1.5805, respectively. Calculations showed that a 6×10^{-4} change in the external refractive index increases the effective refractive index of the 2.1- μm wide sensing waveguide by 2.5×10^{-5} . Using Eqn. (4.1), the spectral dip shifts 0.936 nm. As a result, the sensitivity of the MZI sensor can be calculated using Eqn. (4.3) to be 1560 nm/RIU (refractive index unit) at the wavelength of 1550 nm.

4.2.2 Fabrication of optofluidic chip by packaging the waveguide chip

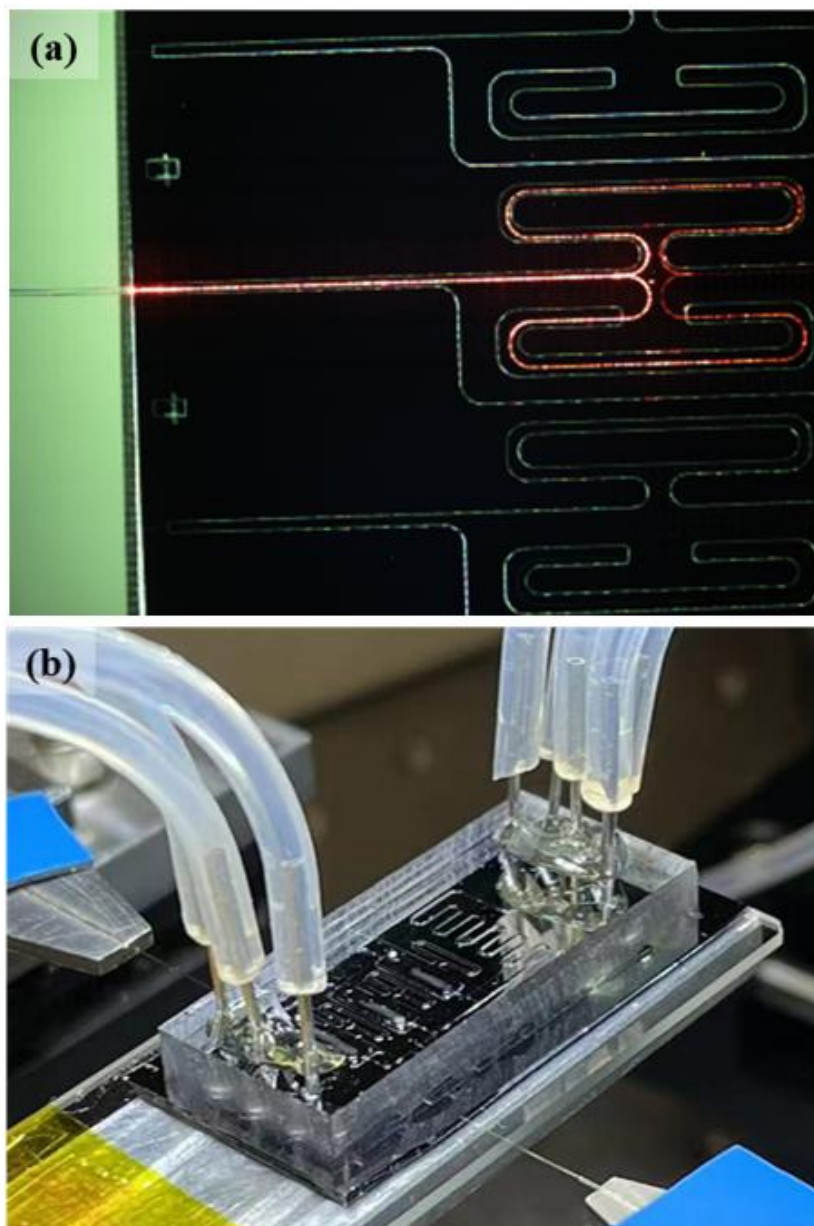


Figure 4.5 (a) A photograph of a red-lit SU8 optical waveguide MZI sensor. (b) Image of an optofluidic device vertically integrated with a PDMS microfluidic layer on top of an optical waveguide chip.

with microfluidic layer

The upper microfluidic chip was fabricated by using casting method. First, an SU-8 mold containing microchannels was prepared. A mixture of PDMS monomer and a

cross-linking agent (in a 10:1 ratio) was degassed for 30 minutes. Subsequently, the PDMS mixture was poured onto the SU-8 mold and subjected to a 2-hour baking process at 70 °C to ensure complete cross-linking. The cured PDMS layer was eventually removed from the SU-8 mold. The layer and waveguide chip underwent a 30-second plasma treatment at 200 W. To prevent leaks, the liquid PDMS mixture was put all the way around the Ormoclad layer's edge. Using a homemade alignment device, the PDMS layer was positioned and joined to the waveguide chip. In order to create a strong link between the waveguide chip and the PDMS microfluidic channel layer, the optofluidic chip was clamped and baked at 70 °C for three hours.

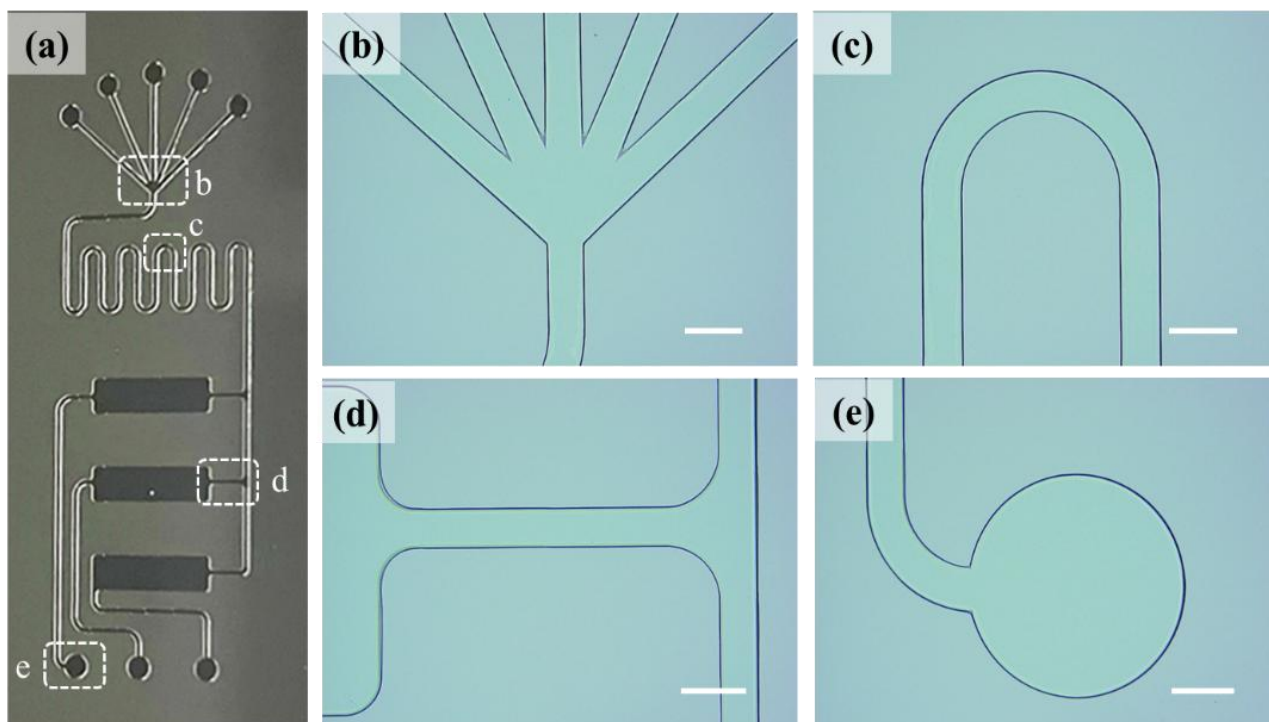


Figure 4.6 (a) Photograph of a fabricated SU-8 mold for preparation of microfluidic chips by casting method. (b)-(e) Photos of the different parts of the SU-8 mold taken by using a laser scanning confocal microscope. The length of scale bars is 500 μm .

The optical waveguide chips before and after vertical integration with the microfluidic layer are depicted in Fig. 4.5. A picture of the artificial SU-8 optical waveguide under red light is shown in Fig. 4.5(a). It can be clearly seen that a sensing window has been made to enable the vertical integration of the microfluidic layer for analyte detection in liquid samples, and that a cladding layer has been printed next to the optical waveguide. A fully packaged optofluidic device with four inlets, one serpentine mixer, and three outputs is shown in Fig. 4.5(b). These parts are intended for waste liquid injection, mixing, and collecting waste liquids. Figure 4.6 shows the completed SU-8 mold.

During testing, the four inlets are used for injecting four solutions, i.e., APTES solution, human IgG, PBS, and antibody strip buffer, respectively.

During the packaging process with the microfluidic layer, oxygen plasma was applied to activated sensor surface to a hydrophilic state [81]. First, the optofluidic chip's microchannel was filled with an aqueous solution containing 4% APTES (aminopropyltriethoxysilane) to salinate the sensing arm for 20 minutes. This step helped prepare the surface for subsequent functionalization. Phosphate-buffered saline (PBS) buffer solution was then used to flush the sensing window, ensuring that the sensor was in a stable and clean environment. Subsequently, the sensor arm of the chip was incubated at room temperature for approximately half an hour using a solution that included 100 $\mu\text{g}/\text{mL}$ goat anti-human IgG. This step facilitated the binding of the specific antibodies to the sensing surface, enabling target molecule detection. Following the incubation, the unbound detection antibody was washed out, leaving

only the specifically bound molecules on the sensor surface. A 1% BSA (bovine serum albumin) solution was introduced into the chip to prevent nonspecific binding sites, which significantly reduced background noise and improved the sensor's specificity. To finish the functionalization process, a PBS buffer solution was administered to remove any molecules that were loosely attached. At this stage, the MZI biosensor was ready for the detection of HIgG (Human Immunoglobulin G) or other target molecules.

4.3 Testing and characterization of the fabricated SU-8 waveguide and optofluidic chip

Using an end-fire coupling configuration, the spectrum responses of the polymer optical waveguide device were assessed. Light was launched into the optical waveguide device using an ASE (Amplified spontaneous emission) light source that operated in the C band wavelength region (1530 ~ 1560 nm). This was accomplished by coupling the light into and out of the chip using lensed single-mode optical fibers (SMF). The spectra of the transmitted light were measured using an optical spectrum analyzer (AQ6374, Yokogawa Company, Japan).

4.3.1 Transmission spectra of the fabricated MZI microsensors

Fig. 4.7(a) depicts the transmission spectra of the SU-8 optical waveguide MZI sensors before and after packaging with a microfluidic layer. The spectrum of the MZI sensor before packing is shown in Fig. 4.7(a). The spectrum from 1530 nm to 1560 nm

is not uniformly flat. This non-uniformity can be attributed to the activation of higher-order optical modes, as the optical waveguide is designed for single-mode operation with an Ormoclاد cladding. For the SiO₂/SU-8/air waveguide configuration, the essential width for single-mode operation is around 2.4 μm.

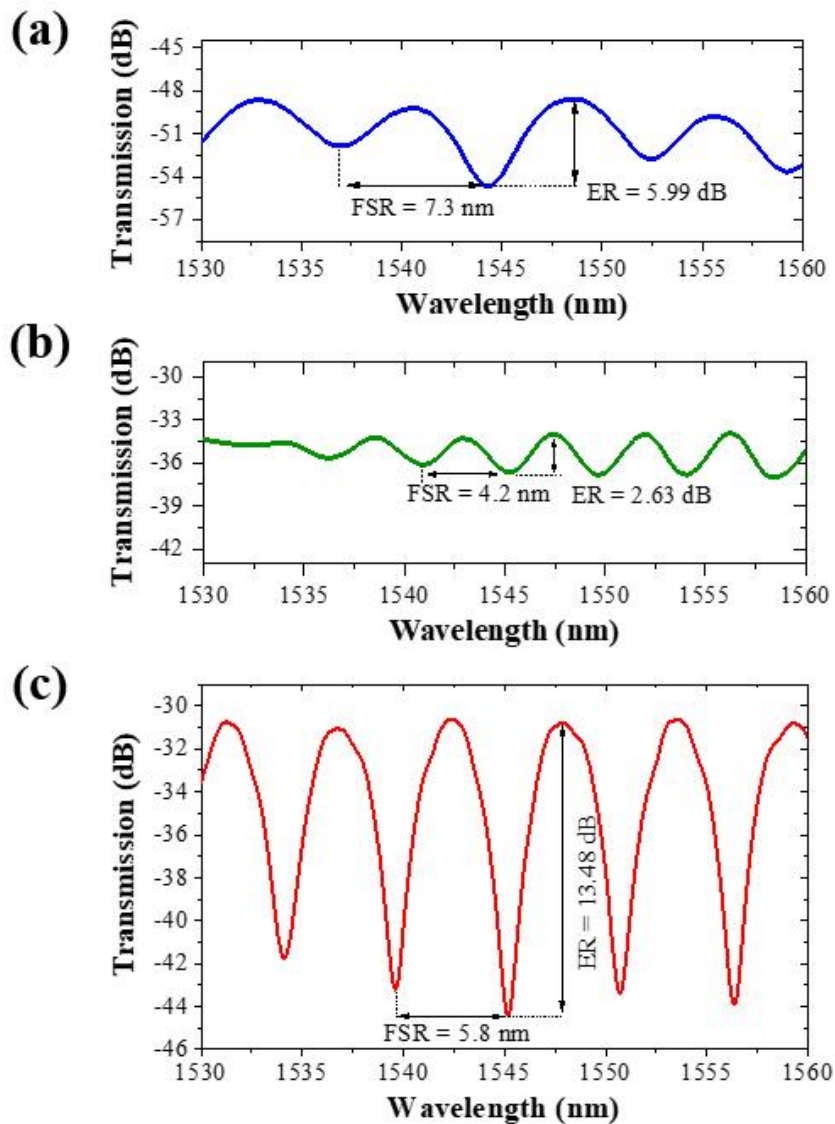


Figure 4.7 Transmission spectra of the fabricated SU-8 waveguide MZI sensor. (a) The MZI sensor's spectrum without OrmoClad cladding. (b) The MZI sensor's spectrum following construction with OrmoClad coating. (c) The MZI sensor's spectrum in an optofluidic device following a water injection.

The MZI sensor's transmission spectrum becomes more uniform and regular after applying an OrmoClad cladding layer, as seen in Fig. 4.7(b). Using Eqn. (4.2) and numerically calculated values of the group refractive indexes, it is possible to conclude

that this decrease is caused by a change in n_{g2} from 1.6090 to 1.5805 as the cladding layer transitions from air ($n = 1.0$) to Ormoclad ($n = 1.52$).

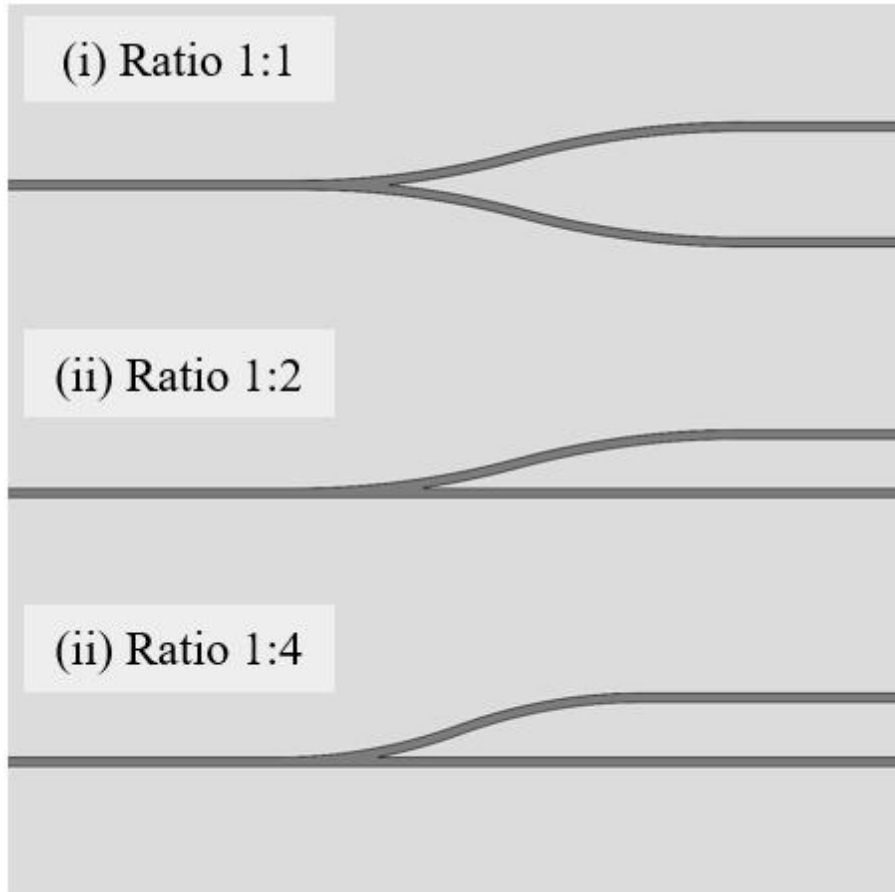


Figure 4.8 Three designs of polymer waveguide Y splitters with different power splitting ratios: 1:1, 1:2, 1:4

Fig. 4.7(c) displays the observed transmission spectrum of the MZI sensor, which includes a PDMS microfluidic layer and water injection into the optofluidic chip. An increase of 5.8 nm in FSR was observed upon the injection of water into the sensor window. Eqn. (4.2) and the numerically obtained refractive indexes were used to calculate n_{g1} , the group refractive index of the waveguide in 2.1 μm width, which decreased from 1.6143 to 1.6028. This decrease is responsible for the observed rise.

Of particular interest is the significant improvement in the extinction ratio (ER) of the transmission spectrum, which increased from 2.63 dB to 13.48 dB. This enhancement is due to the particularly built Y splitter used in the MZI sensor. The Y splitter compensates for light propagation losses in the sensing arm, balancing light power from both arms and achieving regulated interference at the output. This enhancement is due

In Fig. 4.8(a), the 1:1 Y splitter represents a symmetric design, while the 1:4 Y splitter features a smaller arc radius compared to the 1:2 Y splitter. The reduced arc radius of the 1:4 Y splitter results in higher bending losses and a higher splitting ratio. However, it is observed that the MZI sensor employing the 1:2 Y splitter achieves the deepest extinction ratio when compared to the results obtained with the 1:1 and 1:4 Y splitters.

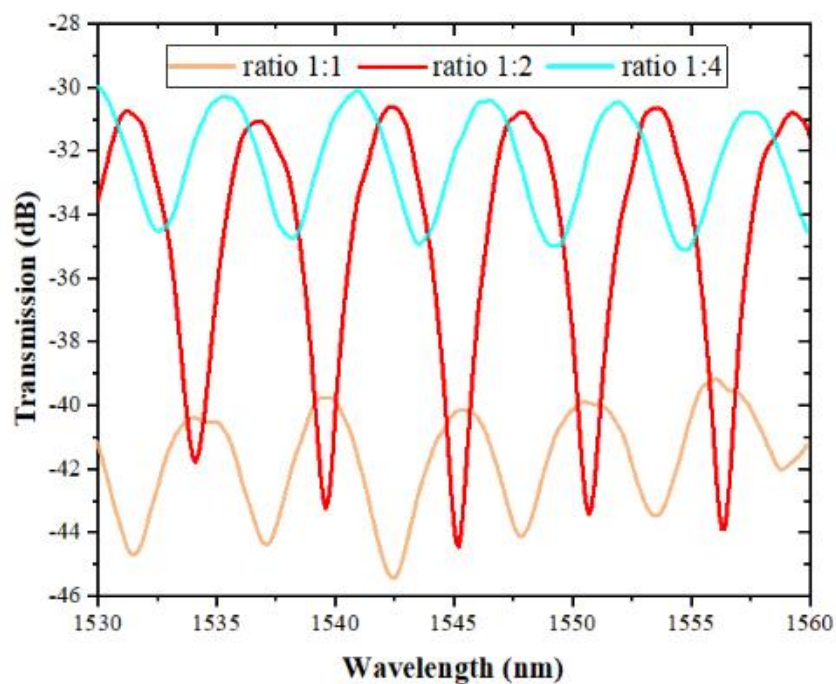


Figure 4.9. Transmission spectra of the fabricated polymer waveguide MZI sensors using these three Y splitters in the input port of MZIs.

Upon comparison of the transmission spectra of the MZI sensor before and after the cladding fabrication, it is evident that the optical power level of the transmission spectrum has increased when the sensor is immersed in water. This increase can be attributed to the following reasons:

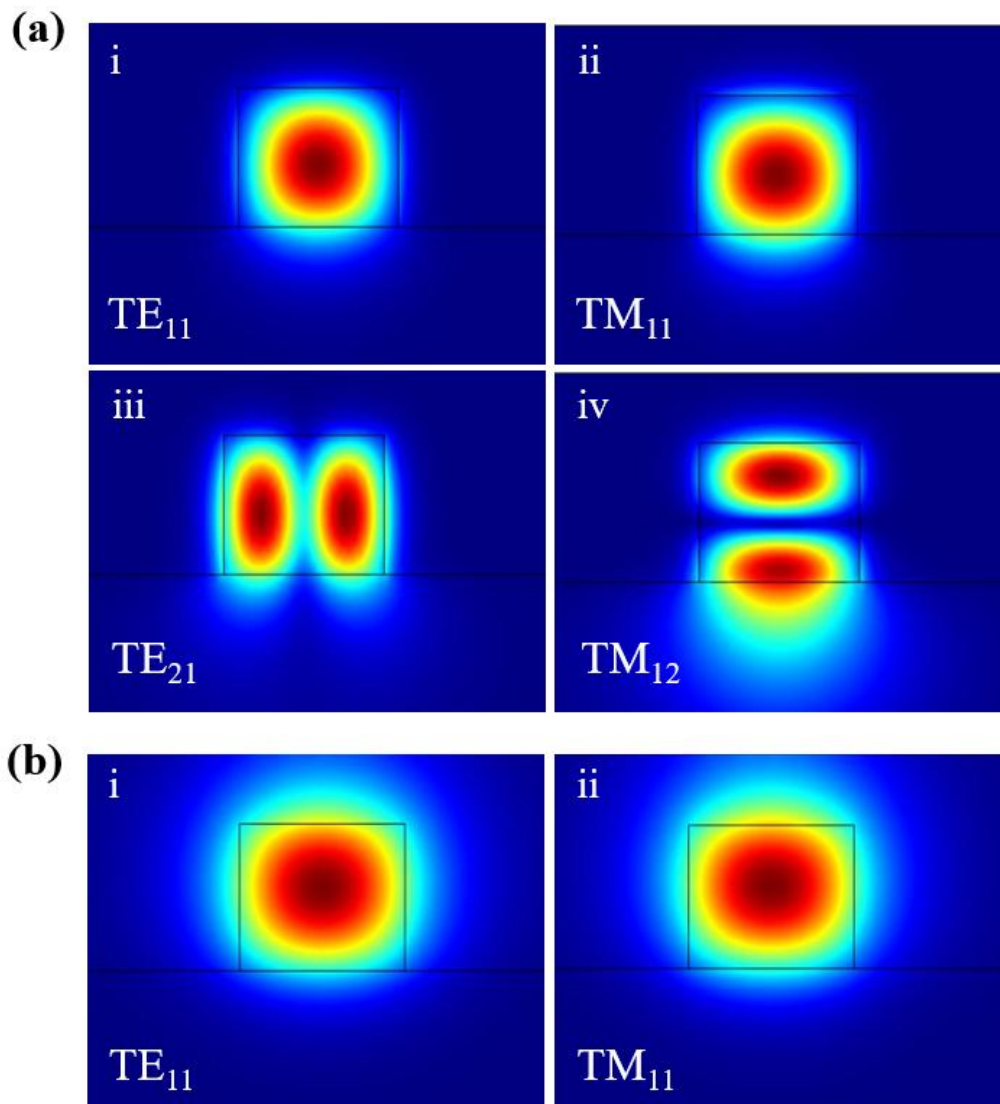


Figure 4.10. (a) Simulated electrical field distribution of mode of 2.7- μm waveguide in air cladding, (i) TE_{11} mode, (ii) TM_{11} mode, (iii) TE_{21} mode, (iv) TM_{12} mode. (b) Simulated electrical field distribution of mode of 2.7- μm waveguide in Ormoclad, (i) TE_{11} mode, (2) TM_{11} mode.

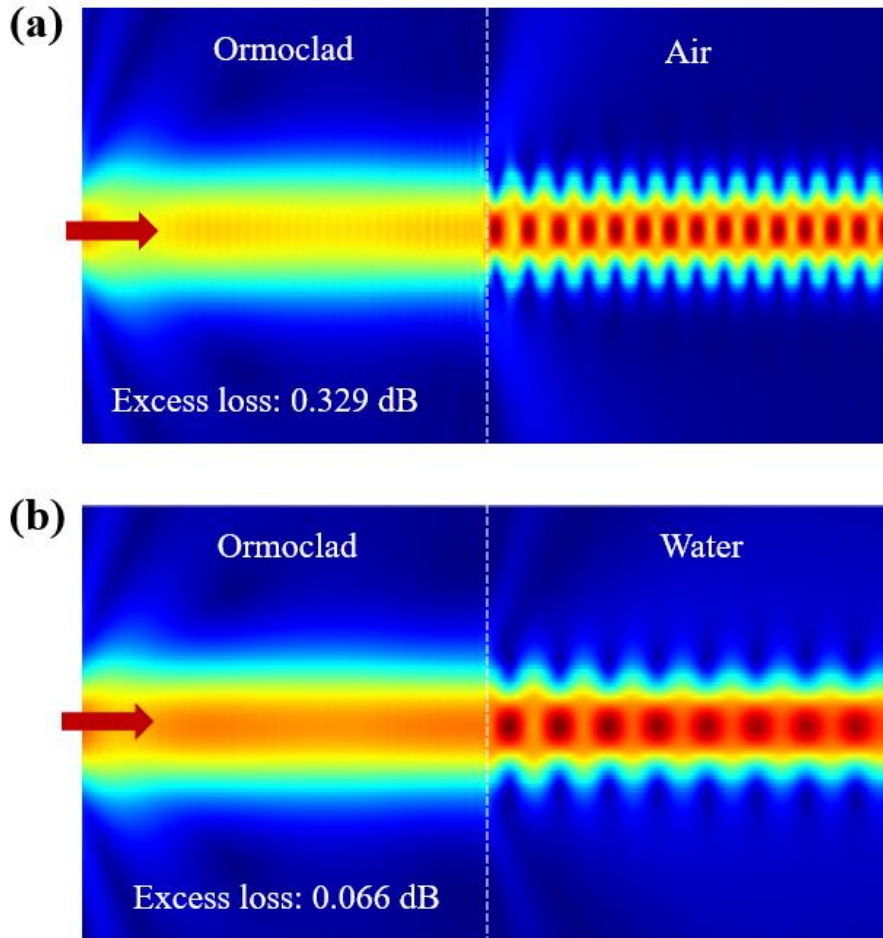


Figure 4.11 Simulated electrical field distribution of light transmission in (a) Ormoclad/air and (b) Ormoclad/water interface. The simulated excess loss for Ormoclad/air interface and Ormoclad/water interfaces are 0.329 dB and 0.066 dB respectively.

1) Elimination of excitation of higher-order modes: The utilization of Ormoclad cladding eliminates the excitation of higher-order modes in the SU-8 waveguide. Simulation results in Fig. 4.10 demonstrate that second-order optical modes, such as TE_{21} and TM_{12} modes, are occur only present in the SU-8 waveguide with air cladding (Fig. 4.10(a)), but disappear after switched the upper cladding from air to Ormoclad (Fig. 4.10(b)). The absence of these higher-order modes in the transmission spectrum leads to improved transmission efficiency and increased optical power levels.

2) When immersed in water, the optical waveguide modes at the interface surrounding the sensing window exhibit improved matching. This is due to the smaller refractive index difference between Ormoclad and water, in contrast to the refractive index difference between Ormoclad and air. This results in better mode matching at the interface, reducing optical losses. The simulation findings in Fig. 4.11 show that the excess loss falls from 0.329 dB to 0.066 dB as the waveguide external medium transitions from air to water.

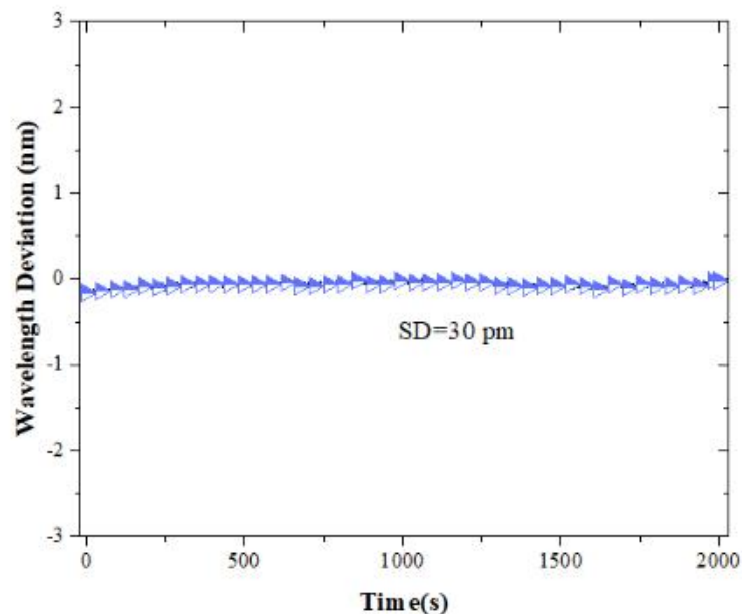


Figure 4.12 Long-time test of the peak wavelength stability of a fabricated polymer waveguide MZI sensor immersed in water. The standard deviation (SD) is 30 nm.

Fig. 4.12 shows the results of a long-term stability test conducted on the optofluidic chip, aimed at evaluating its performance over an extended period. In this test, the optofluidic chip with a packaged sensing window was filled with deionized

(DI) water. The objective was to measure the deviation of a peak wavelength in the transmission spectrum over a duration of 2000 seconds. The standard deviation (SD) of the measured peak wavelengths was determined to be 30 pm. This value quantifies the level of variation or fluctuation observed in the peak wavelength measurements during the stability test. A lower standard deviation indicates higher stability and greater consistency in the sensor's performance throughout the test period.

4.3.2 Measurement of the bulk sensitivity of the fabricated MZI sensors

The fabricated MZI sensors were subjected to tests using glucose solutions of varying concentrations to evaluate their bulk sensitivity. To introduce and remove the glucose solutions from the microfluidic channels, a motorized syringe pump was utilized. Fig. 4.13 (a) gives the measured wavelength shifts of the sensor during these tests. The graph clearly demonstrates that as the concentration of glucose increases, the interference peak wavelength has a red shift. This shift in wavelength indicates a change in the refractive index of the surrounding medium due to the presence of glucose. The shift is directly proportional to the concentration of glucose, allowing for quantitative measurements of glucose concentration using the MZI sensor. Fig. 4.13(b) further illustrates the relationship between the wavelength shift of the MZI sensor and the surrounding refractive indexes, which can be calculated based on the concentrations of the glucose solutions. This graph provides a calibration curve that enables the determination of unknown glucose concentrations by measuring the corresponding wavelength shifts in the MZI sensor [117]. The observed transmission spectra of the SU-8 waveguide MZI sensors in various glucose solutions are given in

the inset of Fig. 4.13 (b). It is evident from the results that the bulk sensitivity of the fabricated waveguide MZI sensor is approximately 1695.95 nm/RIU, which closely aligns with the estimated sensitivity of 1560 nm/RIU.

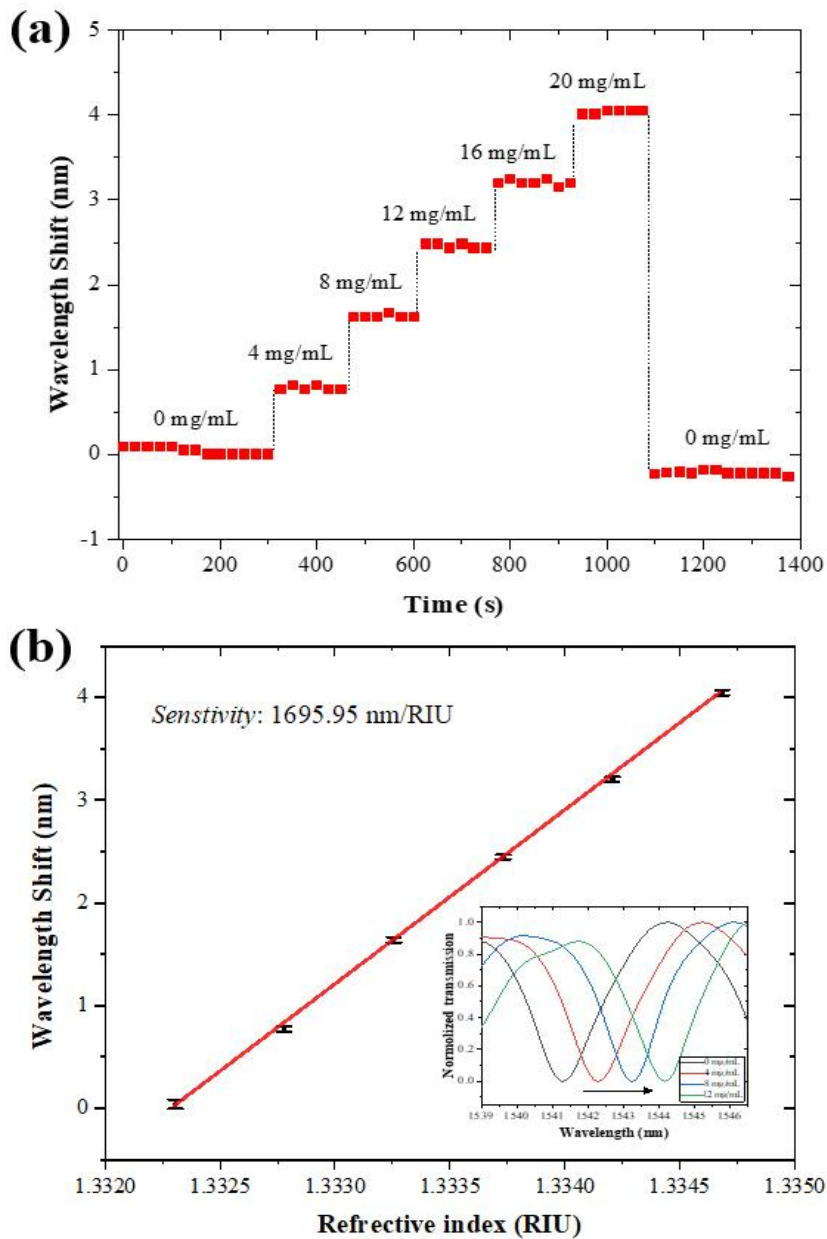


Figure 4.13. Test bulk sensitivity of the fabricated optofluidic chip. (a) The wavelength shift corresponding to the concentration of glucose in a water solution; (b) The wavelength shift corresponding to the change in refractive index. The inset shows the tested varying transmission spectra.

4.4 Testing of the fabricated optofluidic chip in the detection of human Immunoglobulin G

The fabricated optofluidic chip was utilized to measure and quantify the concentration levels of HIgG, a well-known antibody presenting in extracellular fluids and blood. The human body uses HIgG to fight off viral and bacterial infections. This experiment can show the optofluidic chip's capability in detecting disease biomarkers, specifically the concentration of HIgG [115]. The waveguide MZI sensors were functionalized using the approach shown in Fig. 4.14 (a). The SU-8 waveguide's hydrophilic surface was activated before being salinated with APTES. It was further modified with goat anti-human IgG. Fig. 4.14 (b) shows the MZI biosensor's dynamic response to a 1 ng/mL HIgG solution. The 90%-response time is approximately 4 minutes, and the total wavelength shift is around 0.33 nm. Figure 4.14 (c) depicts the measured wavelength shifts of the MZI biosensors in HIgG solutions at various concentrations ranging from 0 ng/mL to 1000 ng/mL. The corresponding transmission spectra are presented in the inset. By utilizing the triple of the standard deviation, the noise-estimated LOD is determined to be 267 pg/mL, equivalent to 1.78 pM. This LOD value is equivalent or exceeds the sensitivity of most similar sensors reported by other studies [109,112,115].

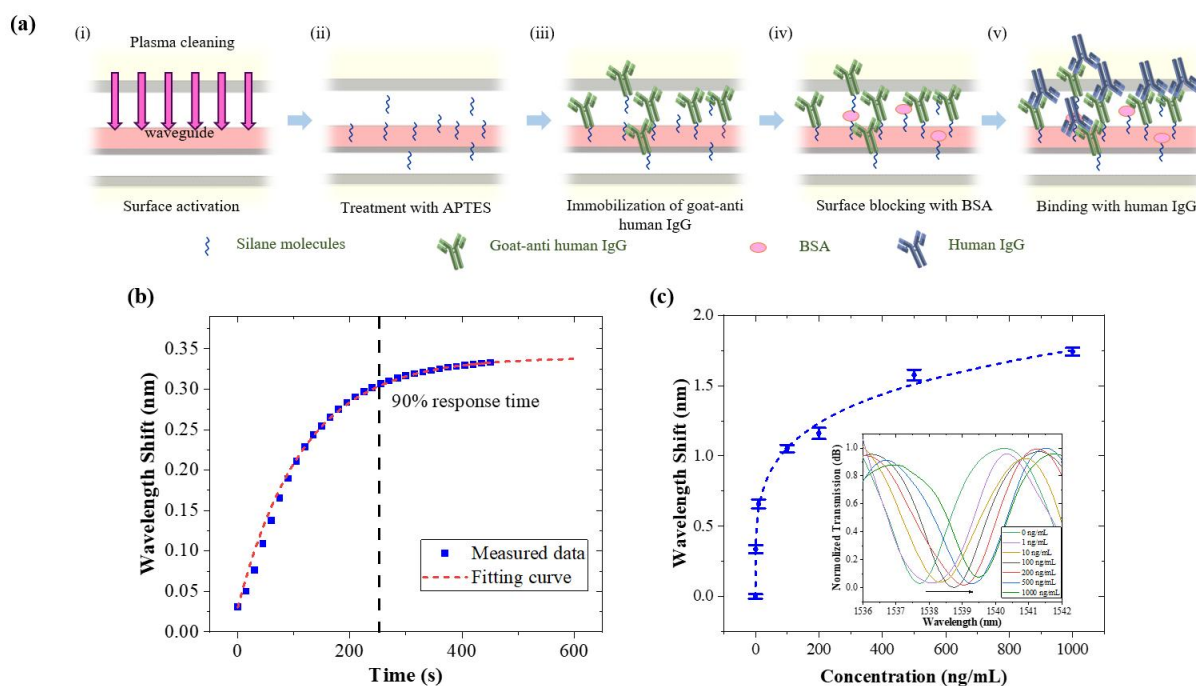


Figure 4.14 (a) A schematic representation of the surface functionalization process for the detection of HIgG. (b) The dynamic response of the biosensor when exposed to a 1 ng/mL target antibody solution. (c) The responses of the biosensor to various concentrations of the target antibody.

The responses of the MZI biosensor to the target analyte, HIgG, and a negative control, human serum albumin (HSA), were compared to evaluate the biosensor's specificity. The measured reactions of the biosensor to HSA at different concentrations, i.e., 1 ng/mL, 10 ng/mL, 100 ng/mL, and 1000 ng/mL, are shown in Fig. 4.15. These responses were found to be 0.029, 0.152, 0.19, and 0.143 times, respectively, compared to the similar responses to HIgG at the same concentrations. This observation indicates a high degree of selectivity of the MZI biosensor, as the biosensor exhibits significantly stronger responses to the target analyte (HIgG)

compared to the negative control (HSA) at all tested concentrations.

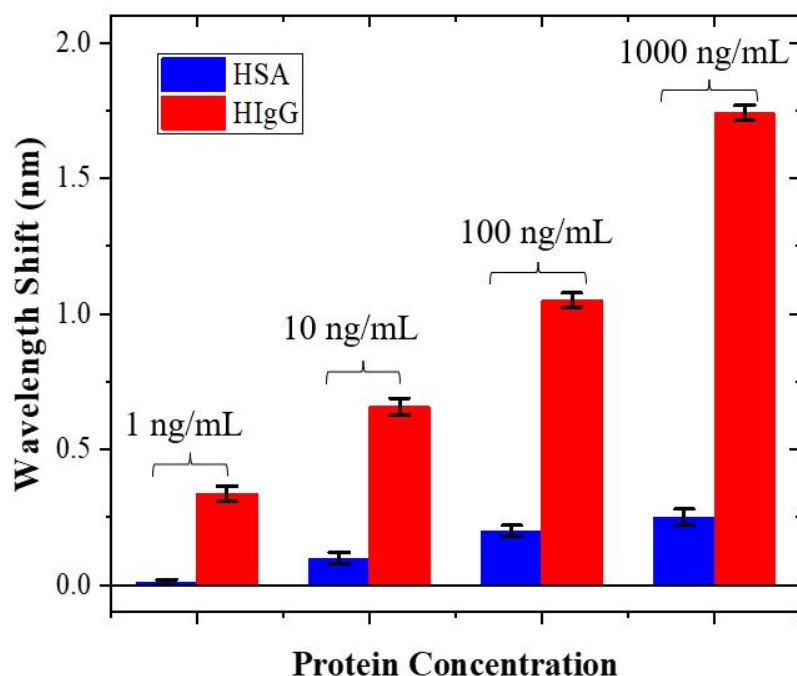


Figure 4.15 A comparison of the sensor's reactions to a control protein HSA and the target analyte HIgG.

4.5 Reusability Testing

The fabricated polymer optical waveguide MZI sensor-based optofluidic biochip serves as a versatile label-free biosensing platform capable of detecting various types of disease biomarkers. In this study, we focused on demonstrating its detection capability for HIgG, a commonly used disease biomarker. The rationale behind choosing HIgG was based on its characteristics as a relatively large molecule (with a molecular weight of 150 kDa) and the fact that the binding of smaller protein biomarkers on a surface often induces significant refractive index changes [118]. By

integrating the MZI sensor into the optofluidic chip, we enable the detection of a broad range of protein biomarkers. Moreover, we believe that comparable procedures can be used to other biological analyses, such as nucleic acid testing or virus detection [119]. This highlights the potential of our optofluidic chip as a versatile tool for various bioanalytical applications beyond the detection of HIgG alone.

The optofluidic chip developed in our work offers the advantage of being reusable for multiple measurements. By employing an antibody stripping solution, the HIgG layer can be effectively removed from the sensor surface after each detection. Fig. 4.16 illustrates the successful application of the MZI biosensor for five consecutive measurement cycles. Following each detection, the MZI sensor was subjected to a

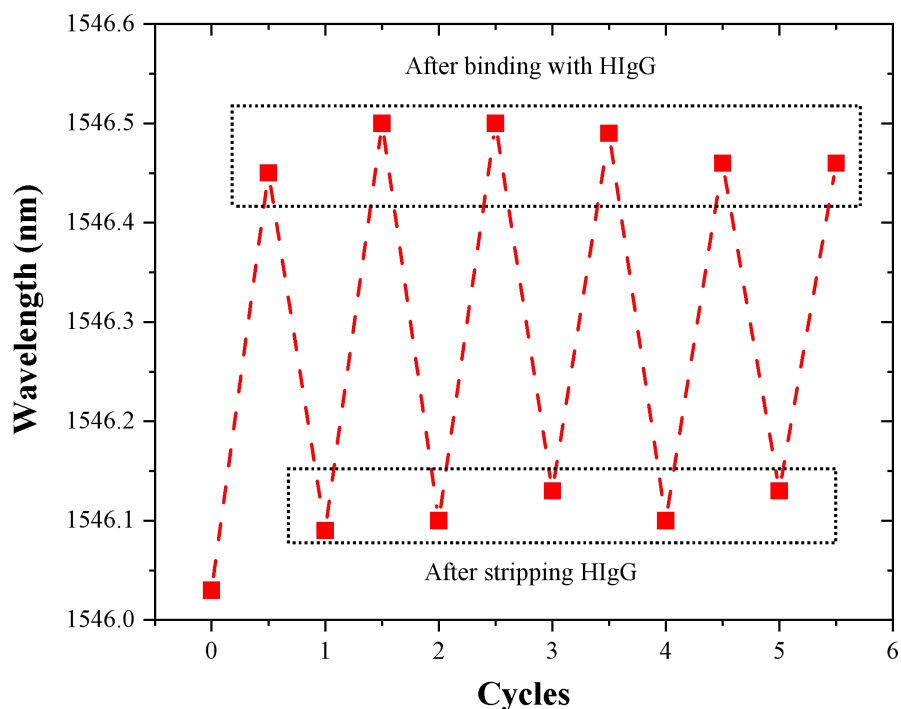


Figure 4.16 Measured interference peak wavelengths in five cycles of HIgG detection on a manufactured optical MZI biosensor.

30-minute incubation in an antibody stripping solution. This solution specifically disrupts non-covalent bonds, facilitating the removal of the HIgG layer while preserving the stable binding of the lower layer of goat anti-human IgG to the SU-8 surface through APTES. Consequently, the stripped MZI biosensor can be reused for subsequent HIgG detection without experiencing any significant loss in sensitivity over the course of the five testing cycles

4.6 Summary

In summary, an integrated optofluidic biochip with directly printed polymer optical waveguide MZI sensors have been presented. These MZI sensors are with asymmetric configurations and width-tailored waveguides and can offer high sensitivity for biosensing applications. They can be vertically integrated with a microfluidic layer to make integrated optofluidic biochips for on-chip label-free biodetection.

Experimental results have demonstrated that the on-chip integrated MZI sensors have impressive performance whose bulk sensitivity is as high as 1695.95 nm/RIU. The optofluidic chip has been demonstrated to detect HIgG at an extremely low concentration level, i.e., 1.78 pM. It is anticipated that such compact reusable optofluidic chip can be utilized to develop tiny point-of-care diagnostic tools and devices.

Chapter 5. Optofluidic chip with high-Q polymer waveguide microring resonator sensors

5.1 Introduction

In addition to MZI, MRR is another common waveguide sensor widely used in integrated optofluidic chips. Compared to MZI, MRR have a much smaller footprint, making them more suitable for integrated photonic applications. Besides, MRR possesses narrower line width, indicating high-sensitivity biological analysis.

Adam L. *et al.* demonstrated for the first time using silicon-on-insulator microring optical resonator arrays for clinical diseases biomarker detection [120]. An initial-slope-based quantitation method has been applied to estimate the unknown protein concentration level with better accuracy. A low limit of detection of 2 ng/mL is achieved in carcinoembryonic antigen (CEA) detection. L. Wang *et al.* developed a simple UV-based soft imprint technique that can be used to fabricate polymer photonics devices with only one step imprinting [121]. For the fabricated ring resonator, the Q value reach 5×10^4 and 2.7×10^4 in air and water respectively. The bulk sensitivity of the sensor is about 50 nm/RIU, and its specific detection in 5 $\mu\text{g/mL}$ human IgG has been demonstrated. T. Chalyan *et al.* develop biosensor devices by using silicon oxynitride (SiON) microring resonators to detect AflatoxinM1 (AFM1) [122]. Two functionalization strategies i.e., DNA-aptamers immobilization and antigen-binding fragments (fab') functionalization were tested to realize specific

detection. According to the result, a higher signal is observed on the Fab'-functionalized surface. As the AFM1 detection is more efficient on Fab'-functionalized surface, with more reproducible result. And the lowest detectable concentration is 5 nM.

In this chapter, we study a an optofluidic chip with directly printed polymer optical waveguide MRR sensors, as shown in Fig. 5.1. We design and fabricate an all-pass MRR sensor based on width-tailored waveguides using our own-built digital UV lithography processes. The optical spectral properties and biosensing abilities of the fabricated MRR sensor will be tested and characterized. By vertically integrating the MRR sensors with a microfluidic layer, an optofluidic chip will be fabricated for on-chip label-free biodetection.

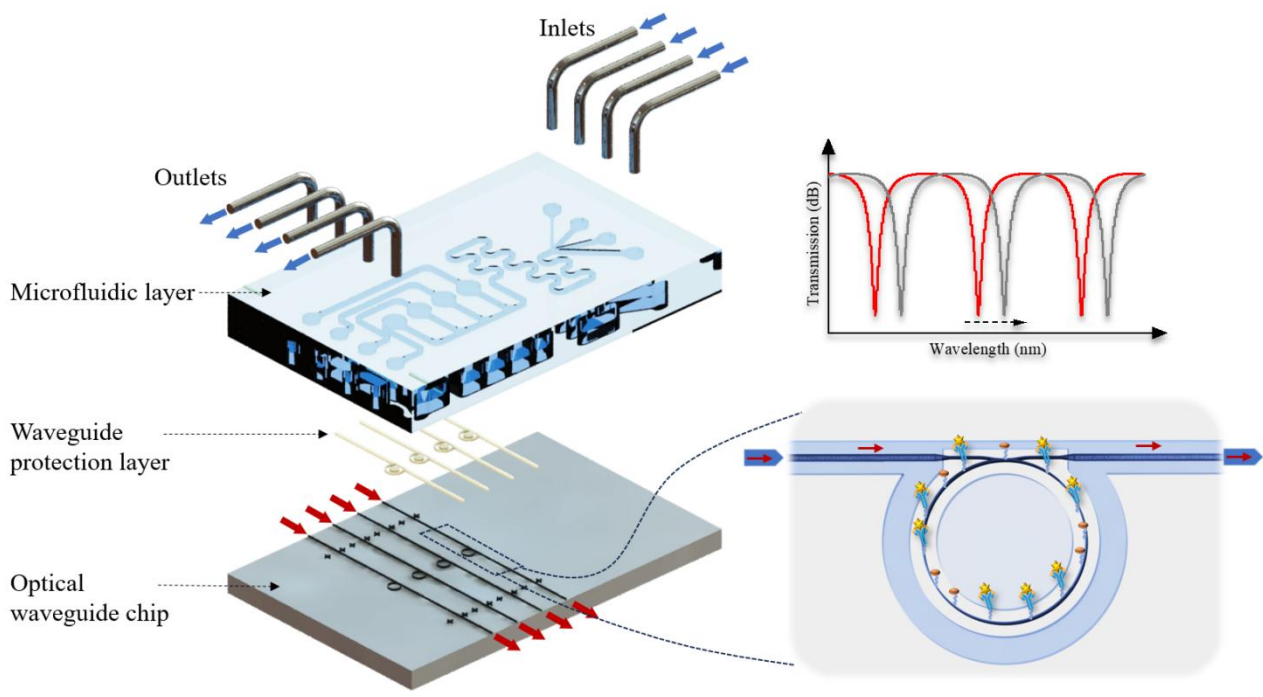


Figure 5.1 Optofluidic chip featuring multiple polymer optical waveguide MRR sensors that are directly printed onto the chip.

5.2 Design of high-Q ring sensors

Considering the materials system (SiO₂/SU-8/Ormoclad), to make the waveguide work under single mode condition, the waveguide size we choose is 2.7 μm in width and 2.0 μm in height. Inside the sensing window, the upper cladding is air or analyte liquid. To alleviate multimode interference, we can narrow the waveguide in sensing area. A smaller bending radius will contribute to smaller footprint. But at the same time, we must make sure the bending waveguide is able to confine the mode. Taken the waveguide materials system and waveguide size into consideration, we choose 300 μm as ring radius. As for the structure of MRR, the Q factor can be given:

$$Q = \frac{\pi n_g L \sqrt{ra}}{(1 - ra)\lambda}, \quad (5.1)$$

where n_g , L , refer to group index of ring waveguide and perimeter of MRR. And r , a , λ refer to self-coupling coefficients, cross-coupling coefficients as well as resonance wavelength respectively.

According to Eqn. (5.1), Q factor is related to the coupling ratio (r or κ) and the ring loss coefficient (a). Ideally, r equal to 1.0 if there's no loss. And Q factor will be infinity when $r \times a$ tends to be 1. In order to increase the Q factor, one need to reduce the ring loss, and increase the coupling coefficient as much as possible. However, a very high Q spectrum may have some penalty in ER.

To optimize the Q factor of MRR, we design the MRR in two dimensions, i.e., varying the ring loss coefficient and the coupling coefficient. The changing of ring

loss coefficient can be realized by set different ring width, including 2.7 μm , 2.4 μm and 2.1 μm .

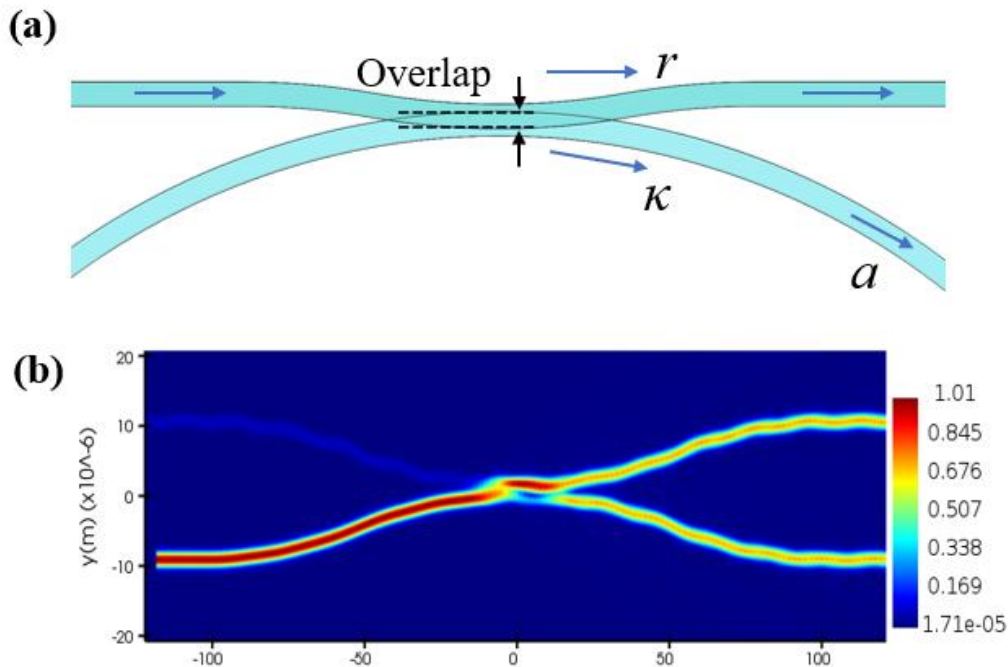


Figure 5.2 (a) Schematic of simulated structure of gapless coupler. (b) simulated electric field of gapless coupler when the overlap distance is 1200 nm.

As for the coupling issue, we applied a gapless coupler, as shown in Fig. 5.2 (a), in which we take 2.4- μm ring waveguide as example. It is easier to fabricate compared to the directional coupler. We can adjust the distance of overlap to easily vary the coupling coefficient. Fig. 5.2 (b) shows the simulated electric field of a gapless coupler with overlap of 1200 nm. And we define coupling coefficient is the ratio of light coupled into the ring to the total amount of the light.

Through numerical simulation, we have found the dependence of coupling coefficients on the overlap distance, as shown in Fig. 5.3. The overlap distance is zero when the ring waveguide just touch the bending waveguide. When the overlap

distance smaller than zero, it indicates a gap-based coupler, i.e., directional coupler. If the distance increases, the coupling ratio will decrease to zero exponentially. When the overlap distance greater than zero, it indicates an overlap-based coupling. As the overlap increases from 0 to 1300 nm, the coupling coefficient takes practically all the values between 0 and 1. Based on the simulation results, we may use the overlap-based coupling mechanism to achieve the requisite coupling coefficient. The MRR should operate at critical coupling, i.e., $a = r$. However, in practice, an ideally critical coupling is difficult to achieve due to the small estimation error and fabrication error. As a result, we choose two coupling coefficients near 0.5 for each width of MRR,

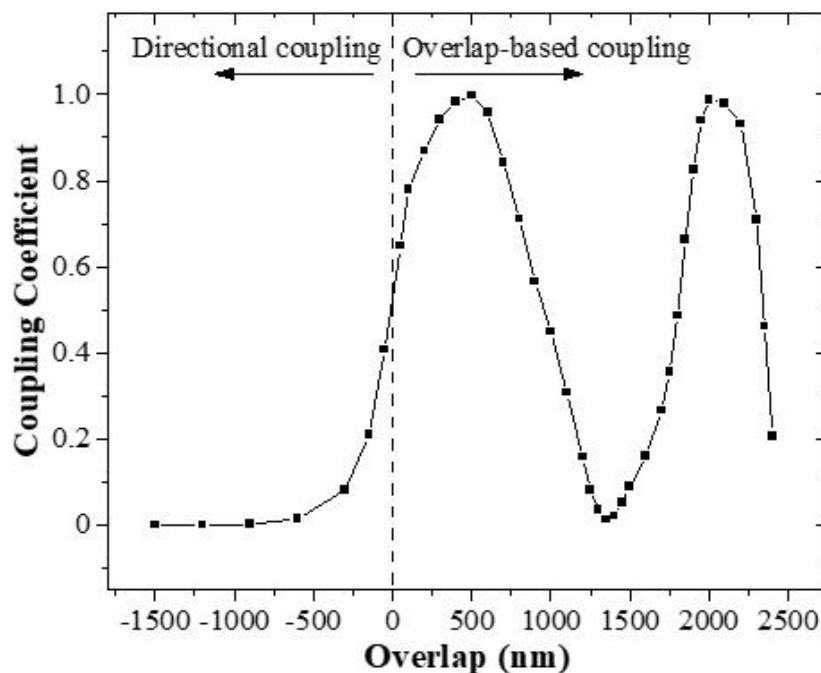


Figure 5.3 Calculated coupling coefficient as function of overlap distance.

which may satisfy most of all-pass MRR designs.

The sensitivity of an MRR sensor can be estimated as:

$$S = \frac{\lambda}{n_e} \cdot \frac{\partial n_e}{\partial n_{ext}}, \quad (5.2)$$

where λ_{res} , n_e and n_{ext} are the resonant wavelength, effective refractive index, and environmental refractive index, respectively. Using our waveguide structure and material, i.e., SiO₂, SU-8 and water-based liquid analyte, the n_e and $\partial n_e / \partial n_{ext}$ are numerically calculated to be 1.523 and 0.0302, respectively. As a result, an MMR sensor's estimated sensitivity around the wavelength of 1550 nm is 30.73 nm/RIU.

5.3 Fabrication of SU-8 waveguide MRR sensor and optofluidic chip

The MRR waveguide sensor based optofluidic chip was fabricated with the own-built digital ultraviolet lithography technology.

5.3.1 Fabrication of SU-8 waveguide MRR sensors

Firstly, SU-8 2005 was spun onto the wafer. Soft bake was conducted at 65°C for 5 mins and 95 °C for 10 mins, to fully remove solvent. Then DUL was applied to inscribe the waveguide pattern onto the wafer. A MRR pattern was equally divided into a serious of 600 × 600-pixel sub-patterns. The exposure time for one sub-pattern is 0.7 s. The exposure time was reduced more than halve compared to the MZI fabrication, which means the fabrication efficiency was improved. After exposure, the sample was post-baked at 65°C for 5 mins and 95°C for 25 mins. Finally, develop the sample with PGMEA for 2 mins. To make the SU-8 crosslink completely and release

internal residual stress, the sample was hard-baked at 120 °C for 60 mins, and then naturally cooling down to room temperature.

To protect the waveguide and open a sensing window, a waveguide protection layer was fabricated with another commercial photoresist, i.e., Ormoclad. Firstly, Ormoclad was spun onto the waveguide chip surface. Then baked the sample on a hotplate at 80 °C for 20 mins. Such a prebake process is optional for the solvent-free photoresist. It can improve the film homogeneity and adhesion to the substrate. Exposure was also conducted by the DUL system. An overlay assistant function was applied to align the protection layer pattern with the fabricated waveguide well. During exposure, the transition pixel was 300, and the nonlinear compensation coefficient was 0.25. It can address the liquid resist shrinkage issue. Afterwards, the sample was baked on a hotplate at 130 °C for 20 mins. Although the Ormoclad was cured immediately after exposure, this high-temperature post-bake process can further increase the adhesion to the substrate. Subsequently, the sample was developed by MIBK for 90 s. To increase the thermal and environmental stability of the Ormoclad layer, the sample was baked on a hotplate at 150 °C for 3 hours.

Fig. 5.4(a)-(d) shows SEM images of fabricated SU-8 waveguide MRR sensors. Fig 5.4(a) shows that the Ormoclad layer can be aligned well with the MRR waveguide. The width of straight waveguide that covered with Ormoclad is 2.7 μm , which shown in the Fig. 5.2(b). When light enter the ring, a gapless coupler is applied, for the advantages of higher fabrication tolerance compared to directional coupler. Fig. 5.2(d) shows a coupler with good geometry without any residual, which is owing to

the proximity effect compensation during exposure. To enhance the evanescent field for a stronger light-matter interaction the sensing ring waveguide is narrowed to be 2.4 μm , as shown in Fig. 5.4(c).

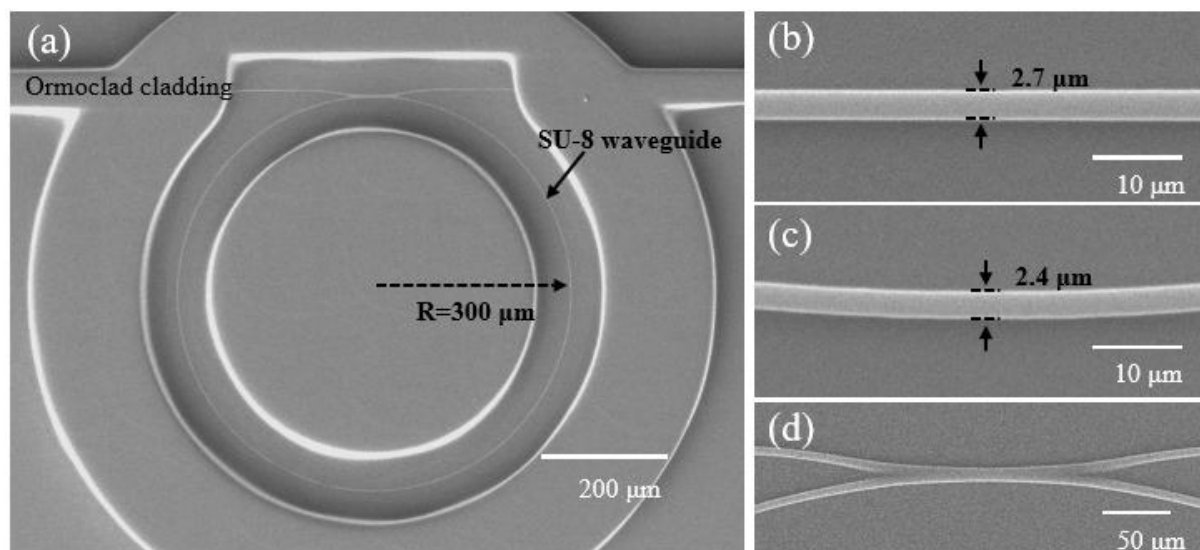


Figure 5.4 SEM images of MRR waveguide sensor. (b) 2.7- μm straight waveguide. (c) 2.4- μm ring waveguide. (d) gapless coupler.

5.3.2 Fabrication of the SU-8 MRR sensor integrated optofluidic chip

The microfluidic chip was prepared by casting method with PDMS. The microchannel mold was also fabricated with SU-8. Firstly, monomer and curing reagent was mixed with ratio of 10:1. Degas the mixture in a vacuum oven, and then pour onto the mold surface, cured the mixture at 90 °C for 2 hours. To avoid leakage from the gap, we smear some liquid PDMS around the Ormoclad. Before binding the microfluidic layer with waveguide chip, treat the two layers with oxygen plasma, which can activate the surface hydroxy. Then bind the two layers together and apply some pressure. High temperature and pressure will make the binding stronger. After an overnight baking,

the chip was packaging tightly. An optofluidic chip vertically integrated with a PDMS microfluidic layer on top of an optical waveguide chip is depicted in Fig. 5.5.

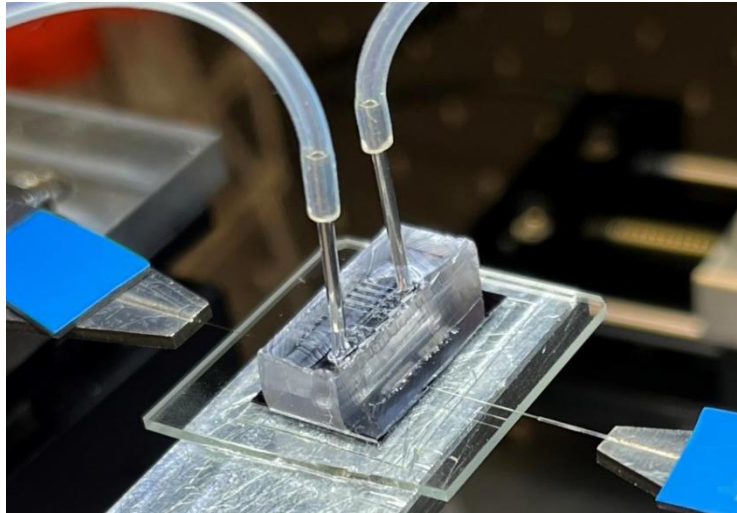


Figure 5.5 Photograph of an optical waveguide chip with a PDMS microfluidic layer vertically placed on top of an optofluidic chip

5.4 Testing and characterization of the fabricated SU-8 waveguide MRR sensor and optofluidic chip

Using an end-fire coupling setup, the spectrum responses of the polymer optical waveguide chip were measured. A lensed SMF was used to direct light from an ASE light source that was operating in the C-band wavelength range of 1530 to 1560 nm into the optical waveguide chip. Another lensed SMF was used to couple the transmitted light into an optical fibre, and an optical spectrum analyser (AQ6374, Yokogawa Company, Japan) was used to measure the light's spectrum.

5.4.1 Transmission spectra of the fabricated MRR sensors

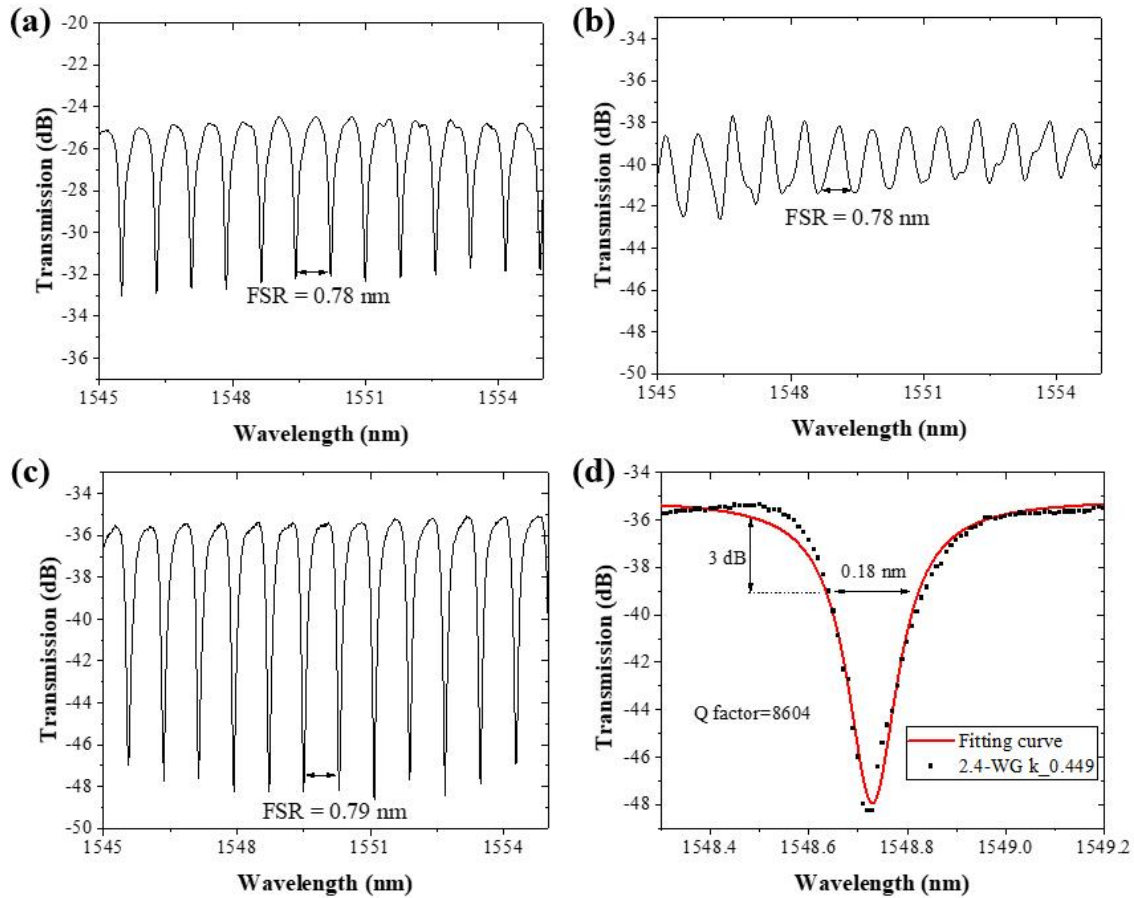


Figure 5.6 Measured transmission spectra of the fabricated polymer waveguide MRR sensor. (a) Spectrum of the MRR sensor with air cladding. (b) Spectrum of the MRR sensor after fabrication of Ormoclad cladding. (c) Spectrum of the MRR sensor in optofluidic chip after injecting with water. (d) Close-up spectrum of the MRR sensor in water near the wavelength of 1544 nm.

The transmission spectra of the fabricated SU-8 waveguide MRR sensors before and after packaging with microfluidic chip are shown in Fig. 5.6. Fig. 5.6(a) shows the spectrum of MRR before packaging. In the wavelength range from 1545 nm to 1545 nm, the flatness is not very well. It may be resulted from the excitation of higher-order mode in optical waveguide. As it is designed to operate at single mode under Ormoclad cladding. After making an Ormoclad cladding, the extinction ratio decrease

significantly, which indicates an inappropriate splitting ratio of the gapless coupler. As the coupler was designed to work in a water-based environment.

Fig. 5.6(c) shows the measured transmission spectrum of the MRR sensor after packaging with microfluidic chip and injecting water into the device. After immersing the sensing ring into water, the *FSR* increased from 0.78 nm to 0.79 nm. The *FSR* of MRR can be estimated:

$$FSR = \frac{\lambda^2}{n_g L}. \quad (5.3)$$

From Eqn. (5.3) and numerical simulation of group refractive indices, one can learn that the change of *FSR* resulted from a decrease of n_g of the 2.4- μm wide waveguide from 1.6112 to 1.6013. Also, the extinction ratio of the transmission spectrum increases from 8 dB to 14 dB. The enlarged image of the resonance peak at 1548.7 nm is shown in Fig. 5.6(d). The Q value can be calculated to be 8604, which is very promising for biological analysis applications.

5.4.2 Transmission spectra of the SU-8 waveguide MRRs with different loss and coupling coefficients

In the experiments, to obtain a spectrum with high Q factor for subsequent testing, we evaluated and compared the sensor performances of various designs. There are six designs with different ring waveguide widths and overlap distances as well as different resulted coupling coefficients, whose values are (2.1 μm , 650 nm, 0.442), (2.1 μm , 550nm, 0.592), (2.4 μm , 1000 nm, 0.449), (2.4 μm , 850 nm, 0.64), (2.7 μm , 1350 nm, 0.46), and (2.7 μm , 1100nm, 0.655). Fig.5.7(a)-(f) show the transmission spectra of the

fabricated MRRs after packaging with Ormoclad cladding and injected with water. As shown in Fig. 5.7(c), the MRR with 2.4- μm ring and 0.449 coupling ratio have the narrowest linewidth and the highest contrast ratio of 13 dB at 1550 nm. Therefore, the design of MRR sensor with 2.4- μm ring with overlap distance of 1000 nm will be used for further testing.

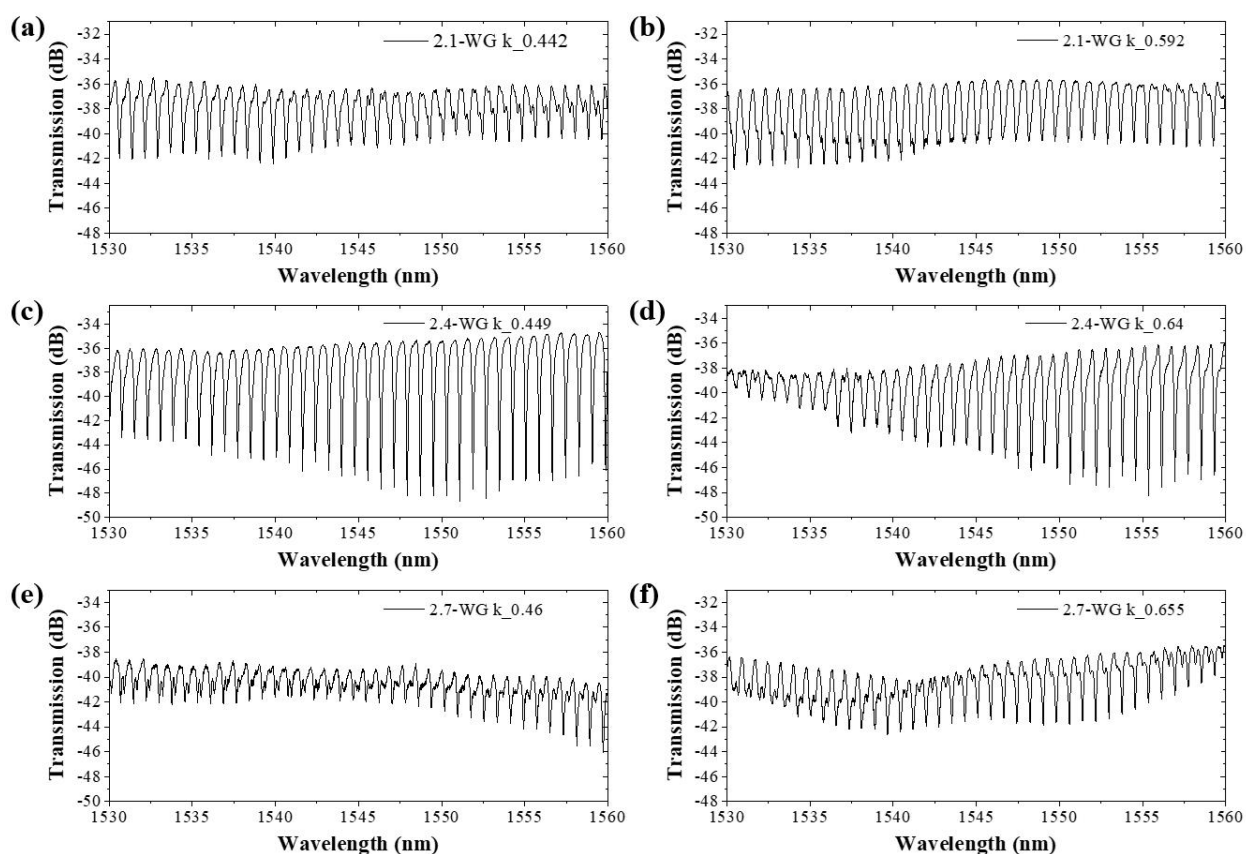


Figure 5.7 Transmission spectra of the fabricated MRR with different loss and coupling coefficients.

5.4.3 Testing of the bulky sensitivity of the fabricated SU-8 waveguide MRR sensors

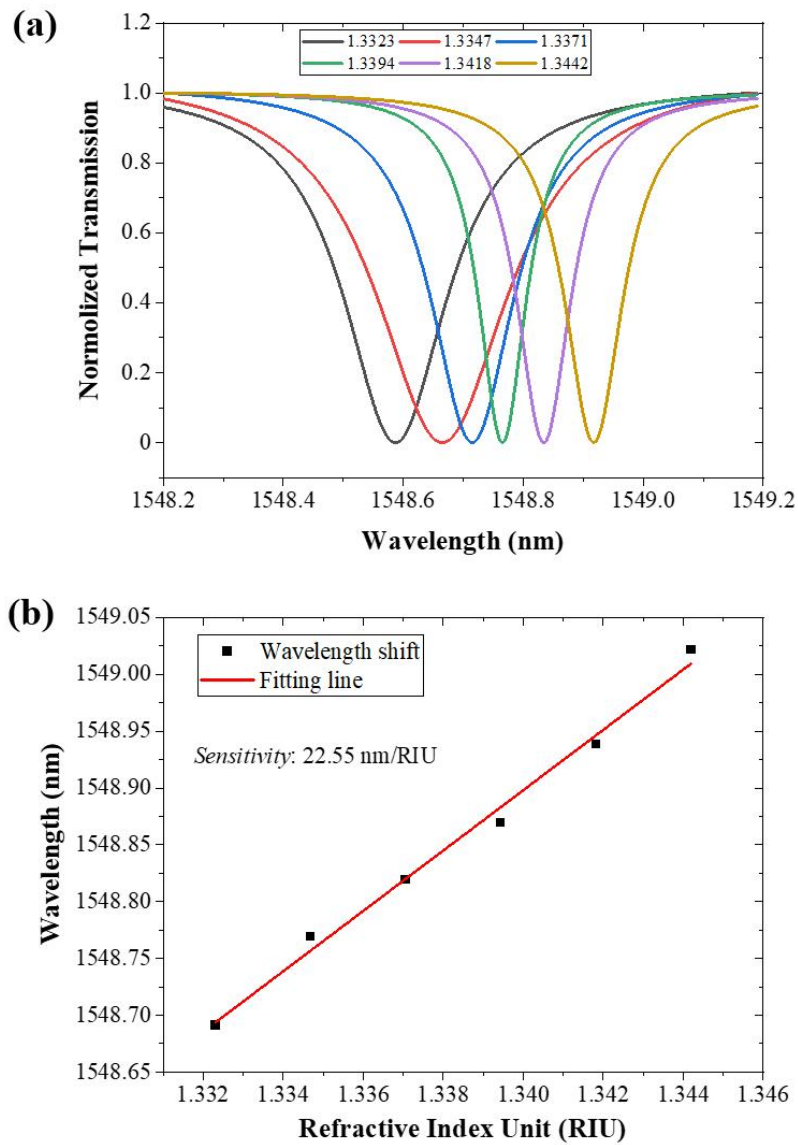


Figure 5.8 (a) Measured transmission spectra towards varying refractive index of solution. (b) Dependence of wavelength shift on the external refractive index change.

Glucose solutions of different concentrations were used to evaluate the bulk sensitivity of the manufactured MRR sensors. Injecting glucose solution into or out of the microfluidic channels is done with a motorized syringe pump. As the concentration of glucose increases, the observed wavelength moves to a longer wavelength, as seen in

Fig. 5.8(a). The MRR sensors' wavelength shift on the external refractive indices is presented in Fig. 5.8(b). It reveals that the refractive index of the fabricated waveguide MRR sensor is about 22.55 nm/RIU, which is close to the numerical simulation value, i.e., 30.73 nm/RIU.

5.5 Summery

To summarize, we have developed an optofluidic biochip with directly printed polymer optical waveguides MRR sensors. Using our own-built DUL, an all-pass MRR sensor based on a width-tailored waveguide has been designed and directly printed for biosensing applications. After vertical integration with a microfluidic layer, an optofluidic chip has been fabricated for on-chip label-free biodetection. Experimental results revealed that the on-chip integrated MZI sensors have a bulk sensitivity of 22.55 nm/RIU. Such a small-size high-performance optofluidic chip with directly printed MRR biosensors is promising in the development of compact point-of-care diagnostic devices and instruments.

Chapter 6. Summary and outlook for future works

6.1 Summary

This thesis explores the development and application of advanced optofluidic chip platforms enabled by polymer optical waveguide sensors. These include MZI and MRR sensor architectures, fabricated using an in-house DUL system.

The SU-8 waveguide fabrication processes were established by using DUL technology. Characterization demonstrates low propagation losses of 0.238 dB/mm and negligible bending losses, enabling the integration of complex waveguide-based devices such as MMI splitters. Compared to conventional lithography techniques, the DUL approach offers significant advantages in terms of cost, throughput, and flexibility. Some fabrication issues such as proximity effect and stitching error have been eliminated by numerical pre-estimation and dynamic exposure processes. This grayscale and dynamic optical exposure approach is thought to hold great promise for creating waveguides with 2.5D and even 3D features.

Building upon these robust waveguide fabrication capabilities, an optofluidic biochip platform integrating MZI sensors was developed. This approach simplifies the manufacturing process compared to traditional silicon-based photonic chips. The asymmetric MZI design, coupled with a specialized Y-splitter, achieving a remarkable extinction ratio of 13.48 dB. Vertical integration with a microfluidic layer further enhances the functionality. The MZI sensor was demonstrated an exceptionally high bulk refractive index sensitivity of 1695.95 nm/RIU. The optofluidic chips were

validated for label-free detection, outperforming commercial ELISA tests in detecting human IgG down to 1.78 pM concentrations. Such process can be extended to many other diseases' biomarker. This cost-effective and high-performance detection platform holds immense value for enhancing healthcare services, particularly in resource-limited settings, and could play a pivotal role in public health crises by enabling rapid and accurate biomarker detection, thereby facilitating timely medical interventions.

Additionally, a highly integrated optofluidic platform incorporating MRR sensors was developed, leveraging the DUL fabrication advantages. The all-pass MRR sensor design achieved a record-high quality factor of 8604, enabling narrow transmissive spectral features crucial for high-sensitivity biological analyses, such as nucleic acid or virus testing.

In summary, these optofluidic chip technologies based on polymer optical waveguide biosensors offer significant advantages in terms of miniaturization, cost-effectiveness, high sensitivity, and ease of functionalization. This paves the way for the development of compact, robust, and versatile point-of-care testing and diagnostic devices with transformative potential for various healthcare and environmental monitoring applications.

6.2 Future outlook

With the developed DUL technology, we have developed two kinds of waveguide sensors, i.e. MZI and MRR sensors, has been fabricated successfully and integrated into optofluidic chips. Several outlooks for future investigations are listed below:

1) Further integration of different components with other functions, such as light sources, photodetectors, and analyte pretreatment components, can make the optofluidic chip to be a highly versatile, multifunctional analytical platform. Such a monolithical integration of these diverse optoelectronic and microfluidic components will result in significant improvements in system functionality, compactness, and overall operational robustness.

2) Regarding sensor design, the exploration of diverse waveguide designs, such as slot waveguides, photonic crystal waveguides, and graded-index structures, may provide new schemes for tailoring the optical response and sensing ability of integrated optofluidic chips. The versatility in waveguide design can facilitate the realization of advanced optical sensing abilities, such as enhanced evanescent field and increased detection sensitivity.

3) Addition to polymer materials, a variety of materials including III-V materials, ceramic materials, rare-earth-elements-doped glass can be explored for developing compact high-performance photonic chips. For instance, silicon nitride (Si_3N_4), lithium niobate (LiNbO_3) and aluminium nitride (AlN) are promising to be explored for high-volume fabrication of integrated photonic chips with broader bandwidth and high efficiency. Ceramic materials, such as barium titanate (BaTiO_3) and yttrium

aluminium garnet ($\text{Y}_3\text{Al}_5\text{O}_{12}$), have advantages in harsh environmental conditions, i.e., high temperatures or chemically aggressive environments.

4) Various types of functional optofluidic chips can be explored in biomedical applications. In light of lab-on-a-chip conception, researchers have started to explore more complex optofluidic microsystems, such organ-on-chips (OoCs). In these OoCs devices, microfluidic delivery components, multiple cell types and on-chip detection devices are integrated to mimic the complexity of human organ systems. They may enable the study of disease and drug mechanisms with greater fidelity than traditional vitro models, making optofluidic chips a transformative tool for advancing our understanding of disease mechanisms and accelerating therapeutic development.

Reference

1. J. Wang, S. A. Maier, and A. Tittl, "Trends in Nanophotonics-Enabled Optofluidic Biosensors," *Advanced Optical Materials* **10**, 2102366 (2022).
2. R. Md. M. Hasan and X. Luo, "Promising Lithography Techniques for Next-Generation Logic Devices," *Nanomanuf Metrol* **1**, 67–81 (2018).
3. P. Steglich, D. G. Rabus, C. Sada, M. Paul, M. G. Weller, C. Mai, and A. Mai, "Silicon Photonic Micro-Ring Resonators for Chemical and Biological Sensing: A Tutorial," *IEEE Sensors J.* **22**, 10089–10105 (2022).
4. P. Chen, S. Chen, X. Guan, Y. Shi, and D. Dai, "High-order microring resonators with bent couplers for a box-like filter response," *Opt. Lett.* **39**, 6304 (2014).
5. Y. Xie, Y. Shi, L. Liu, J. Wang, R. Priti, G. Zhang, O. Liboiron-Ladouceur, and D. Dai, "Thermally-Reconfigurable Silicon Photonic Devices and Circuits," *IEEE J. Select. Topics Quantum Electron.* **26**, 1–20 (2020).
6. S. Mohammadi-Pouyan, M. Miri, and M. H. Sheikhi, "Efficient binary and QAM optical modulation in ultra-compact MZI structures utilizing indium-tin-oxide," *Sci Rep* **12**, 8129 (2022).
7. F. Xia and Y. Zhao, "RI sensing system with high sensitivity and large measurement range using a microfiber MZI and a photonic crystal fiber MZI," *Measurement* **156**, 107603 (2020).
8. Z. Ding, P. Liu, J. Chen, D. Dai, and Y. Shi, "On-chip simultaneous sensing of humidity and temperature with a dual-polarization silicon microring resonator," *Opt. Express* **27**, 28649 (2019).
9. D. Barshilia, L.-K. Chau, and G.-E. Chang, "Low-cost planar waveguide-based optofluidic sensor for real-time refractive index sensing," *Opt. Express* **28**, 27337 (2020).
10. X. Ma, J. Wu, L. Jiang, M. Wang, G. Deng, S. Qu, and K. Chen, "On-chip integration of a metal–organic framework nanomaterial on a SiO₂ waveguide for sensitive VOC sensing," *Lab Chip* **21**, 3298–3306 (2021).
11. L. Liu, X. Zhou, J. S. Wilkinson, P. Hua, B. Song, and H. Shi, "Integrated optical waveguide-based fluorescent immunosensor for fast and sensitive detection of microcystin-LR in lakes: Optimization and Analysis," *Sci Rep* **7**, 3655 (2017).
12. A. Densmore, M. Vachon, D.-X. Xu, S. Janz, R. Ma, Y.-H. Li, G. Lopinski, A. Delâge, J. Lapointe, C. C. Luebbert, Q. Y. Liu, P. Cheben, and J. H. Schmid, "Silicon photonic wire biosensor array for multiplexed real-time and label-free molecular detection," *Opt. Lett.* **34**, 3598 (2009).
13. Q. Liu, J. Nam, S. Kim, C. T. Lim, M. K. Park, and Y. Shin, "Two-stage sample-to-answer system based on nucleic acid amplification approach for detection of malaria parasites," *Biosensors and Bioelectronics* **82**, 1–8 (2016).
14. P. K. Drain, E. P. Hyle, F. Noubary, K. A. Freedberg, D. Wilson, W. R. Bishai, W. Rodriguez, and I. V. Bassett, "Diagnostic point-of-care tests in resource-limited settings," *The Lancet Infectious Diseases* **14**, 239–249 (2014).
15. L. A. Low and D. A. Tagle, "Tissue chips – innovative tools for drug development and disease modeling," *Lab on a Chip* **17**, 3026–3036 (2017).
16. "Overview of Optical Technologies for Point of Care Medical Devices," <https://starfishmedical.com/blog/optical-technologies-for-point-of-care/>.

17. C. Lei, H. Kobayashi, Y. Wu, M. Li, A. Isozaki, A. Yasumoto, H. Mikami, T. Ito, N. Nitta, T. Sugimura, M. Yamada, Y. Yatomi, D. Di Carlo, Y. Ozeki, and K. Goda, "High-throughput imaging flow cytometry by optofluidic time-stretch microscopy," *Nat Protoc* **13**, 1603–1631 (2018).
18. M. Beyza Avci, S. Deniz Yasar, and A. E. Cetin, "An optofluidic platform for cell-counting applications," *Analytical Methods* **15**, 2244–2252 (2023).
19. F. Wang, J. Zhu, L. Chen, Y. Zuo, X. Hu, and Y. Yang, "Autonomous and In Situ Ocean Environmental Monitoring on Optofluidic Platform," *Micromachines* **11**, 69 (2020).
20. J. Wang, M. Yao, C. Hu, A. P. Zhang, Y. Shen, H. Tam, and P. K. A. Wai, "Optofluidic tunable mode-locked fiber laser using a long-period grating integrated microfluidic chip," *Opt. Lett.*, OL **42**, 1117–1120 (2017).
21. D. Măriuța, S. Colin, C. Barrot-Lattes, S. Le Calvé, J. G. Korvink, L. Baldas, and J. J. Brandner, "Miniaturization of fluorescence sensing in optofluidic devices," *Microfluid Nanofluid* **24**, 65 (2020).
22. J. W. Parks, H. Cai, L. Zempoaltecatl, T. D. Yuzvinsky, K. Leake, A. R. Hawkins, and H. Schmidt, "Hybrid optofluidic integration," *Lab Chip* **13**, 4118 (2013).
23. S. Chakravarty, W.-C. Lai, Y. Zou, H. A. Drabkin, R. M. Gemmill, G. R. Simon, S. H. Chin, and R. T. Chen, "Multiplexed specific label-free detection of NCI-H358 lung cancer cell line lysates with silicon based photonic crystal microcavity biosensors," *Biosensors and Bioelectronics* **43**, 50–55 (2013).
24. M. A. Butt, G. S. Voronkov, E. P. Grakhova, R. V. Kutluyarov, N. L. Kazanskiy, and S. N. Khonina, "Environmental Monitoring: A Comprehensive Review on Optical Waveguide and Fiber-Based Sensors," *Biosensors* **12**, 1038 (2022).
25. A. Crespi, Y. Gu, B. Ngamsom, H. J. W. M. Hoekstra, C. Dongre, M. Pollnau, R. Ramponi, H. H. van den Vlekkert, P. Watts, G. Cerullo, and R. Osellame, "Three-dimensional Mach-Zehnder interferometer in a microfluidic chip for spatially-resolved label-free detection," *Lab Chip* **10**, 1167 (2010).
26. Q. Liu, Y. Shin, J. S. Kee, K. W. Kim, S. R. Mohamed Rafei, A. P. Perera, X. Tu, G.-Q. Lo, E. Ricci, M. Colombel, E. Chiong, J. P. Thiery, and M. K. Park, "Mach–Zehnder interferometer (MZI) point-of-care system for rapid multiplexed detection of microRNAs in human urine specimens," *Biosensors and Bioelectronics* **71**, 365–372 (2015).
27. S. Wu, Y. Guo, W. Wang, J. Zhou, and Q. Zhang, "Label-free biosensing using a microring resonator integrated with poly-(dimethylsiloxane) microfluidic channels," *Review of Scientific Instruments* **90**, 035004 (2019).
28. U. Levy, K. Campbell, A. Groisman, S. Mookherjea, and Y. Fainman, "On-chip microfluidic tuning of an optical microring resonator," *Applied physics letters* **88**, 111107 (2006).
29. C. F. Carlborg, K. B. Gylfason, A. Kaźmierczak, F. Dortu, M. J. Bañuls Polo, A. Maquieira Catala, G. M. Kresbach, H. Sohlström, T. Moh, L. Vivien, J. Popplewell, G. Ronan, C. A. Barrios, G. Stemme, and W. van der Wijngaart, "A packaged optical slot-waveguide ring resonator sensor array for multiplex label-free assays in labs-on-chips," *Lab Chip* **10**, 281–290 (2010).
30. Q. Liu, K. W. Kim, Z. Gu, J. S. Kee, and M. K. Park, "Single-channel Mach-Zehnder interferometric biochemical sensor based on two-lateral-mode spiral waveguide," *Opt. Express* **22**, 27910 (2014).
31. M. Wang, J. Hiltunen, C. Liedert, S. Pearce, M. Charlton, L. Hakalahti, P. Karioja, and R. Myllylä, "Highly sensitive biosensor based on UV-imprinted layered polymeric – inorganic composite waveguides," *Opt. Express*, OE **20**, 20309–20317 (2012).
32. X. D. Hoa, A. G. Kirk, and M. Tabrizian, "Towards integrated and sensitive surface plasmon resonance biosensors: A review of recent progress," *Biosensors and bioelectronics* **23**, 151–160 (2007).

33. F.-C. Chien, C.-Y. Lin, J.-N. Yih, K.-L. Lee, C.-W. Chang, P.-K. Wei, C.-C. Sun, and S.-J. Chen, "Coupled waveguide – surface plasmon resonance biosensor with subwavelength grating," *Biosensors and Bioelectronics* **22**, 2737–2742 (2007).
34. M. La Notte and V. M. N. Passaro, "Ultra high sensitivity chemical photonic sensing by Mach–Zehnder interferometer enhanced Vernier-effect," *Sensors and Actuators B: Chemical* **176**, 994–1007 (2013).
35. C. Peng, C. Yang, H. Zhao, L. Liang, C. Zheng, C. Chen, L. Qin, and H. Tang, "Optical Waveguide Refractive Index Sensor for Biochemical Sensing," *Applied Sciences* **13**, 3829 (2023).
36. L. Jin, X. Fu, B. Yang, Y. Shi, and D. Dai, "Optical bistability in a high-Q racetrack resonator based on small SU-8 ridge waveguides," *Opt. Lett.*, **OL 38**, 2134–2136 (2013).
37. D. X. Xu, A. Densmore, A. Delâge, P. Waldron, R. McKinnon, S. Janz, J. Lapointe, G. Lopinski, T. Mischki, E. Post, P. Cheben, and J. H. Schmid, "Folded cavity SOI microring sensors for high sensitivity and real time measurement of biomolecular binding," *Opt. Express* **16**, 15137 (2008).
38. W. Bogaerts, P. De Heyn, T. Van Vaerenbergh, K. De Vos, S. Kumar Selvaraja, T. Claes, P. Dumon, P. Bienstman, D. Van Thourhout, and R. Baets, "Silicon microring resonators," *Laser & Photonics Reviews* **6**, 47–73 (2012).
39. Y. Zhu, Q. Chen, L. Shao, Y. Jia, and X. Zhang, "Microfluidic immobilized enzyme reactors for continuous biocatalysis," *Reaction Chemistry & Engineering* **5**, 9–32 (2020).
40. Y. Su, Y. Zhang, C. Qiu, X. Guo, and L. Sun, "Silicon Photonic Platform for Passive Waveguide Devices: Materials, Fabrication, and Applications," *Advanced Materials Technologies* **5**, 1901153 (2020).
41. H. Ni, G. Yuan, L. Sun, N. Chang, D. Zhang, R. Chen, L. Jiang, H. Chen, Z. Gu, and X. Zhao, "Large-scale high-numerical-aperture super-oscillatory lens fabricated by direct laser writing lithography," *RSC Advances* **8**, 20117–20123 (2018).
42. "Drawing Structures in Nano-Scale," <https://semiconductor.samsung.com/us/support/tools-resources/fabrication-process/eight-essential-semiconductor-fabrication-processes-part-4-photolithography-laying-the-blueprint>.
43. P. Petric, C. Bevis, M. McCord, A. Carroll, A. Brodie, U. Ummethala, L. Grella, A. Cheung, and R. Freed, "Reflective electron beam lithography: A maskless ebeam direct write lithography approach using the reflective electron beam lithography concept," *Journal of Vacuum Science & Technology B* **28**, C6C6-C6C13 (2010).
44. M. Rothschild, T. M. Bloomstein, T. H. Fedynyshyn, R. R. Kunz, V. Liberman, M. Switkes, N. N. Efremow, S. T. Palmacci, J. H. C. Sedlacek, D. E. Hardy, and A. Grenville, "Recent Trends in Optical Lithography," **14**, (2003).
45. K. Ronse, "Optical lithography—a historical perspective," *Comptes Rendus Physique* **7**, 844–857 (2006).
46. J. Eldredge, "Evidence-based librarianship: the EBL process," *Library Hi Tech* **24**, 341–354 (2006).
47. B. Shahzad, M. Tanveer, Z. Che, A. Rehman, S. A. Cheema, A. Sharma, H. Song, S. ur Rehman, and D. Zhaorong, "Role of 24-epibrassinolide (EBL) in mediating heavy metal and pesticide induced oxidative stress in plants: A review," *Ecotoxicology and Environmental Safety* **147**, 935–944 (2018).
48. F. Aharonian, A. G. Akhperjanian, U. Barres de Almeida, A. R. Bazer-Bachi, B. Behera, M. Beilicke, W. Benbow, K. Bernlöhr, C. Boisson, O. Bolz, V. Borrel, I. Braun, E. Brion, A. M. Brown, R. Bühler, T. Bulik, I. Büsching, T. Boutelier, S. Carrigan, P. M. Chadwick, L.-M. Chounet, A. C. Clapson, G. Coignet, R. Cornils, L. Costamante, M. Dalton, B. Degrange, H. J. Dickinson, A. Djannati-Ataï, W. Domainko, L. O. Drury, F. Dubois, G. Dubus, J. Dyks, K. Egberts, D. Emmanoulopoulos, P. Espigat, C. Farnier, F. Feinstein, A. Fiasson, A. Förster, G. Fontaine, Seb. Funk, M. Füßling, Y. A. Gallant, B. Giebels, J. F. Glicenstein, B. Glück, P. Goret, C. Hadjichristidis, D. Hauser, M. Hauser, G. Heinzlmann, G. Henri, G. Hermann, J. A.

- Hinton, A. Hoffmann, W. Hofmann, M. Holleran, S. Hoppe, D. Horns, A. Jacholkowska, O. C. de Jager, I. Jung, K. Katarzyński, E. Kendziorra, M. Kerschhaggl, B. Khélifi, D. Keogh, Nu. Komin, K. Kosack, G. Lamanna, I. J. Latham, A. Lemièrre, M. Lemoine-Goumard, J.-P. Lenain, T. Lohse, J. M. Martin, O. Martineau-Huynh, A. Marcowith, C. Masterson, D. Maurin, G. Maurin, T. J. L. McComb, R. Moderski, E. Moulin, M. de Naurois, D. Nedbal, S. J. Nolan, S. Ohm, J.-P. Olive, E. de Oña Wilhelmi, K. J. Orford, J. L. Osborne, M. Ostrowski, M. Panter, G. Pedalletti, G. Pelletier, P.-O. Petrucci, S. Pita, G. Pühlhofer, M. Punch, S. Ranchon, B. C. Raubenheimer, M. Raue, S. M. Rayner, M. Renaud, J. Ripken, L. Rob, L. Rolland, S. Rosier-Lees, G. Rowell, B. Rudak, J. Ruppel, V. Sahakian, A. Santangelo, R. Schlickeiser, F. Schöck, R. Schröder, U. Schwanke, S. Schwarzburg, S. Schwemmer, A. Shalchi, H. Sol, D. Spangler, Ł. Stawarz, R. Steenkamp, C. Stegmann, G. Superina, P. H. Tam, J.-P. Tavernet, R. Terrier, C. van Eldik, G. Vasileiadis, C. Venter, J. P. Vialle, P. Vincent, M. Vivier, H. J. Völk, F. Volpe, S. J. Wagner, M. Ward, A. A. Zdziarski, and A. Zech, "New constraints on the mid-IR EBL from the HESS discovery of VHE γ -rays from IES 0229+200," *A&A* **475**, L9–L13 (2007).
49. N. Anscombe, "Direct laser writing," *Nature Photon* **4**, 22–23 (2010).
 50. A. Selimis, V. Mironov, and M. Farsari, "Direct laser writing: Principles and materials for scaffold 3D printing," *Microelectronic Engineering* **132**, 83–89 (2015).
 51. Z.-L. Wu, Y.-N. Qi, X.-J. Yin, X. Yang, C.-M. Chen, J.-Y. Yu, J.-C. Yu, Y.-M. Lin, F. Hui, P.-L. Liu, Y.-X. Liang, Y. Zhang, and M.-S. Zhao, "Polymer-Based Device Fabrication and Applications Using Direct Laser Writing Technology," *Polymers* **11**, 553 (2019).
 52. A. Travinskya, D. Vorobiev, Z. Ninkov, A. Raisanen, M. A. Quijada, S. A. Smee, J. A. Pellish, T. Schwartz, M. Robberto, S. Heap, D. Conley, C. Benavides, N. Garcia, Z. Bredl, and S. Yllanes, "Evaluation of Digital Micromirror Devices for use in space-based Multi-Object Spectrometer application," *J. Astron. Telesc. Instrum. Syst* **3**, 1 (2017).
 53. A. P. Zhang, X. Qu, P. Soman, K. C. Hribar, J. W. Lee, S. Chen, and S. He, "Rapid Fabrication of Complex 3D Extracellular Microenvironments by Dynamic Optical Projection Stereolithography," *Advanced Materials* **24**, 4266–4270 (2012).
 54. M. Yin, M. Yao, S. Gao, A. P. Zhang, H. Tam, and P. A. Wai, "Rapid 3D Patterning of Poly(acrylic acid) Ionic Hydrogel for Miniature pH Sensors," *Advanced Materials* **28**, 1394–1399 (2016).
 55. B. Huang, M. Yin, A. P. Zhang, and X. Ye, "On-chip microfabrication of thermally controllable PNIPAAm microvalves by using optical maskless stereolithography," *Sensors and Actuators A: Physical* **247**, 397–402 (2016).
 56. M. Yin, Y. Zhang, Z. Yin, Q. Zheng, and A. P. Zhang, "Micropatterned Elastic Gold - Nanowire/Polyacrylamide Composite Hydrogels for Wearable Pressure Sensors," *Adv Materials Technologies* **3**, 1800051 (2018).
 57. J. Wu, M. Yao, F. Xiong, A. P. Zhang, H.-Y. Tam, and P. K. A. Wai, "Optical Fiber-Tip Fabry–Pérot Interferometric Pressure Sensor Based on an In Situ μ -Printed Air Cavity," *J. Lightwave Technol., JLT* **36**, 3618–3623 (2018).
 58. J. Wu, M. Yin, K. Seefeldt, A. Dani, R. Guterman, J. Yuan, A. P. Zhang, and H.-Y. Tam, "In situ μ -printed optical fiber-tip CO₂ sensor using a photocrosslinkable poly(ionic liquid)," *Sensors and Actuators B: Chemical* **259**, 833–839 (2018).
 59. M. Yao, X. Ouyang, J. Wu, A. P. Zhang, H.-Y. Tam, and P. K. A. Wai, "Optical Fiber-Tip Sensors Based on In-Situ μ -Printed Polymer Suspended-Microbeams," *Sensors* **18**, 1825 (2018).
 60. M. Yao, J. Wu, A. P. Zhang, H.-Y. Tam, and P. K. A. Wai, "Optically 3-D μ -Printed Ferrule-Top Polymer Suspended-Mirror Devices," *IEEE Sensors Journal* **17**, 7257–7261 (2017).

61. M. Yao, Y. Zhang, X. Ouyang, A. P. Zhang, H.-Y. Tam, and P. K. A. Wai, "Ultracompact optical fiber acoustic sensors based on a fiber-top spirally-suspended optomechanical microresonator," *Opt. Lett.*, OL **45**, 3516–3519 (2020).
62. P. Zhao, K. V. Krishnaiah, L. Guo, T. Li, H. L. Ho, A. P. Zhang, and W. Jin, "Ultraminiature Optical Fiber-Tip 3D - Microprinted Photothermal Interferometric Gas Sensors," *Laser & Photonics Reviews* 2301285 (2024).
63. J. Wu, X. Guo, A. P. Zhang, and H.-Y. Tam, "Rapid 3D μ -printing of polymer optical whispering-gallery mode resonators," *Opt. Express* **23**, 29708 (2015).
64. S. Gao, W.-T. Tung, D. S.-H. Wong, L. Bian, and A. P. Zhang, "Direct optical micropatterning of poly(dimethylsiloxane) for microfluidic devices," *J. Micromech. Microeng.* **28**, 095011 (2018).
65. M. Yin, B. Huang, S. Gao, A. P. Zhang, and X. Ye, "Optical fiber LPG biosensor integrated microfluidic chip for ultrasensitive glucose detection," *Biomed. Opt. Express* **7**, 2067 (2016).
66. X. Ouyang, T. Liu, Y. Zhang, J. He, Z. He, A. P. Zhang, and H.-Y. Tam, "Ultrasensitive optofluidic enzyme-linked immunosorbent assay by on-chip integrated polymer whispering-gallery-mode microlaser sensors," *Lab Chip* **20**, 2438–2446 (2020).
67. G. Lazarev, A. Hermerschmidt, S. Krüger, and S. Osten, "LCOS Spatial Light Modulators: Trends and Applications," in *Optical Imaging and Metrology*, W. Osten and N. Reingand, eds., 1st ed. (Wiley, 2012), pp. 1–29.
68. X.-H. Xu, B.-Q. Li, Y. Feng, and J.-R. Chu, "Design, fabrication and characterization of a bulk-PZT-actuated MEMS deformable mirror," *J. Micromech. Microeng.* **17**, 2439–2446 (2007).
69. T. Yoon, C.-S. Kim, K. Kim, and J. Choi, "Emerging applications of digital micromirror devices in biophotonic fields," *Optics & Laser Technology* **104**, 17–25 (2018).
70. B. Yang, Y. Zhu, Y. Jiao, L. Yang, Z. Sheng, S. He, and D. Dai, "Compact Arrayed Waveguide Grating Devices Based on Small SU-8 Strip Waveguides," *J. Lightwave Technol.* **29**, 2009–2014 (2011).
71. L. Yang, B. Yang, Z. Sheng, J. Wang, D. Dai, and S. He, "Compact 2×2 tapered multimode interference couplers based on SU-8 polymer rectangular waveguides," *Applied Physics Letters* **93**, 203304 (2008).
72. X. Wang, W. Jin, Z. Chang, and K. S. Chiang, "Buried graphene electrode heater for a polymer waveguide thermo-optic device," *Opt. Lett.*, OL **44**, 1480–1483 (2019).
73. Q. Huang, Y. Wu, W. Jin, and K. S. Chiang, "Mode Multiplexer With Cascaded Vertical Asymmetric Waveguide Directional Couplers," *J. Lightwave Technol.* **36**, 2903–2911 (2018).
74. Q. Huang and K. S. Chiang, "High-Order-Mode-Pass Mode (De)Multiplexer With a Hybrid-Core Vertical Directional Coupler," *Journal of Lightwave Technology* **37**, 3932–3938 (2019).
75. S. Li, Y. Zhou, J. Dong, X. Zhang, E. Cassan, J. Hou, C. Yang, S. Chen, D. Gao, and H. Chen, "Universal multimode waveguide crossing based on transformation optics," *Optica*, OPTICA **5**, 1549–1556 (2018).
76. X. Zhang, A. Hosseini, X. Lin, H. Subbaraman, and R. T. Chen, "Polymer-Based Hybrid-Integrated Photonic Devices for Silicon On-Chip Modulation and Board-Level Optical Interconnects," *IEEE Journal of Selected Topics in Quantum Electronics* **19**, 196–210 (2013).
77. Y. Enami, C. T. Derose, D. Mathine, C. Loychik, C. Greenlee, R. A. Norwood, T. D. Kim, J. Luo, Y. Tian, A. K.-Y. Jen, and N. Peyghambarian, "Hybrid polymer/sol-gel waveguide modulators with exceptionally large electro-optic coefficients," *Nature Photon* **1**, 180–185 (2007).
78. Q. Liu, X. Tu, K. W. Kim, J. S. Kee, Y. Shin, K. Han, Y.-J. Yoon, G.-Q. Lo, and M. K. Park, "Highly sensitive Mach-Zehnder interferometer biosensor based on silicon nitride slot waveguide," *Sensors and Actuators B: Chemical* **188**, 681–688 (2013).

79. E.-S. Lee, K.-W. Chun, J. Jin, and M.-C. Oh, "Frequency Response of Thermo-Optic Phase Modulators Based on Fluorinated Polyimide Polymer Waveguide," *Polymers* **14**, 2186 (2022).
80. C. Wang, D. Zhang, X. Zhang, S. Ding, J. Wang, R. Cheng, F. Wang, Z. Cui, and C. Chen, "Bottom-metal-printed thermo-optic waveguide switches based on low-loss fluorinated polycarbonate materials," *Opt. Express* **28**, 20773 (2020).
81. A. del Campo and C. Greiner, "SU-8: a photoresist for high-aspect-ratio and 3D submicron lithography," *J. Micromech. Microeng.* **17**, R81–R95 (2007).
82. Jiangli Dong, Kin Seng Chiang, and Wei Jin, "Compact Three-Dimensional Polymer Waveguide Mode Multiplexer," *J. Lightwave Technol.* **33**, 4580–4588 (2015).
83. A. Landowski, D. Zepp, S. Wingerter, G. von Freymann, and A. Widera, "Direct laser written polymer waveguides with out of plane couplers for optical chips," *APL Photonics* **2**, 106102 (2017).
84. Y. Xin, G. Pandraud, Y. Zhang, and P. French, "Single-Mode Tapered Vertical SU-8 Waveguide Fabricated by E-Beam Lithography for Analyte Sensing," *Sensors* **19**, 3383 (2019).
85. X. Ouyang, K. Zhang, J. Wu, D. S.-H. Wong, Q. Feng, L. Bian, and A. P. Zhang, "Optical μ -Printing of Cellular-Scale Microscaffold Arrays for 3D Cell Culture," *Sci Rep* **7**, 8880 (2017).
86. D.-H. Lee, "Optical System with 4 μm Resolution for Maskless Lithography Using Digital Micromirror Device," *Journal of the Optical Society of Korea* **14**, 266–276 (2010).
87. T. L. Laidig and H. J. Jeong, "Resolution enhanced digital lithography with anti-blazed DMD," United States patent US10983441B2 (April 20, 2021).
88. K. Kim, S. Han, J. Yoon, S. Kwon, H.-K. Park, and W. Park, "Lithographic resolution enhancement of a maskless lithography system based on a wobulation technique for flow lithography," *Applied Physics Letters* **109**, 234101 (2016).
89. L. B. Soldano and E. C. M. Pennings, "Optical multi-mode interference devices based on self-imaging: principles and applications," *Journal of Lightwave Technology* **13**, 615–627 (1995).
90. P. Liu and Y. Shi, "Simultaneous measurement of refractive index and temperature using a dual polarization ring," *Appl. Opt.*, *AO* **55**, 3537–3541 (2016).
91. X. Ouyang, Z. Yin, J. Wu, C. Zhou, and A. P. Zhang, "Rapid optical μ -printing of polymer top-lensed microlens array," *Opt. Express*, *OE* **27**, 18376–18382 (2019).
92. X. Wang, X. Quan, M. Liu, and X. Cheng, "Silicon-Nitride-Assisted Edge Coupler Interfacing With High Numerical Aperture Fiber," *IEEE Photonics Technology Letters* **31**, 349–352 (2019).
93. Bo Yang, Liu Yang, Rui Hu, Zhen Sheng, Daoxin Dai, Qingkun Liu, and Sailing He, "Fabrication and Characterization of Small Optical Ridge Waveguides Based on SU-8 Polymer," *J. Lightwave Technol.* **27**, 4091–4096 (2009).
94. Y. Jiao, Y. Zhu, X. Hong, Y. Shi, L. Xu, and S. He, "An Integrated Optical Mixer Based on SU8 Polymer for PDM-QPSK Demodulation," *IEEE Photonics Technology Letters* **23**, 1490–1492 (2011).
95. S. Madden, Z. Jin, D. Choi, S. Debbarma, D. Bulla, and B. Luther-Davies, "Low loss coupling to sub-micron thick rib and nanowire waveguides by vertical tapering," *Opt. Express*, *OE* **21**, 3582–3594 (2013).
96. B. Gil Rosa, O. E. Akingbade, X. Guo, L. Gonzalez-Macia, M. A. Crone, L. P. Cameron, P. Freemont, K.-L. Choy, F. Güder, E. Yeatman, D. J. Sharp, and B. Li, "Multiplexed immunosensors for point-of-care diagnostic applications," *Biosensors and Bioelectronics* **203**, 114050 (2022).

97. T. Chalyan, R. Guider, L. Pasquardini, M. Zanetti, F. Falke, E. Schreuder, R. Heideman, C. Pederzolini, and L. Pavesi, "Asymmetric Mach–Zehnder Interferometer Based Biosensors for Aflatoxin M1 Detection," *Biosensors* **6**, 1 (2016).
98. E. Stern, A. Vacic, N. K. Rajan, J. M. Criscione, J. Park, B. R. Ilic, D. J. Mooney, M. A. Reed, and T. M. Fahmy, "Label-free biomarker detection from whole blood," *Nature Nanotech* **5**, 138–142 (2010).
99. Z. Wang, J. Zhao, X. Xu, L. Guo, L. Xu, M. Sun, S. Hu, H. Kuang, C. Xu, and A. Li, "An Overview for the Nanoparticles-Based Quantitative Lateral Flow Assay," *Small Methods* **6**, 2101143 (2022).
100. G. A. Posthuma-Trumpie, J. Korf, and A. van Amerongen, "Lateral flow (immuno)assay: its strengths, weaknesses, opportunities and threats. A literature survey," *Anal Bioanal Chem* **393**, 569–582 (2009).
101. C. Parolo, A. Sena-Torralba, J. F. Bergua, E. Calucho, C. Fuentes-Chust, L. Hu, L. Rivas, R. Álvarez-Diduk, E. P. Nguyen, S. Cinti, D. Quesada-González, and A. Merkoçi, "Tutorial: design and fabrication of nanoparticle-based lateral-flow immunoassays," *Nat Protoc* **15**, 3788–3816 (2020).
102. C. Huang, T. Wen, F.-J. Shi, X.-Y. Zeng, and Y.-J. Jiao, "Rapid detection of IgM antibodies against the SARS-CoV-2 virus via colloidal gold nanoparticle-based lateral-flow assay," *ACS omega* **5**, 12550–12556 (2020).
103. G. G. Meena, A. Jain, J. W. Parks, A. Stambaugh, J. L. Patterson, A. R. Hawkins, and H. Schmidt, "Integration of sample preparation and analysis into an optofluidic chip for multi-target disease detection," *Lab Chip* **18**, 3678–3686 (2018).
104. D. Yin, E. J. Lunt, M. I. Rudenko, D. W. Deamer, A. R. Hawkins, and H. Schmidt, "Planar optofluidic chip for single particle detection, manipulation, and analysis," *Lab Chip* **7**, 1171 (2007).
105. S. Yun, S. Park, B. Park, Y. Kim, S. K. Park, S. Nam, and K. Kyung, "Polymer-Waveguide-Based Flexible Tactile Sensor Array for Dynamic Response," *Advanced Materials* **26**, 4474–4480 (2014).
106. P. Kozma, F. Kehl, E. Ehrentreich-Förster, C. Stamm, and F. F. Bier, "Integrated planar optical waveguide interferometer biosensors: A comparative review," *Biosensors and Bioelectronics* **58**, 287–307 (2014).
107. A. Gaston, I. Lozano, F. Perez, F. Auza, and J. Sevilla, "Evanescent wave optical-fiber sensing (temperature, relative humidity, and pH sensors)," *IEEE Sensors J.* **3**, 806–811 (2003).
108. N. Zhong, Q. Liao, X. Zhu, M. Zhao, Y. Huang, and R. Chen, "Temperature-independent polymer optical fiber evanescent wave sensor," *Sci Rep* **5**, 11508 (2015).
109. P. Ramirez-Priego, D. Martens, A. A. Elamin, P. Soetaert, W. Van Roy, R. Vos, B. Anton, R. Bockstaele, H. Becker, M. Singh, P. Bienstman, and L. M. Lechuga, "Label-Free and Real-Time Detection of Tuberculosis in Human Urine Samples Using a Nanophotonic Point-of-Care Platform," *ACS Sens.* **3**, 2079–2086 (2018).
110. M. Angelopoulou, P. S. Petrou, E. Makarona, W. Haasnoot, I. Moser, G. Jobst, D. Goustouridis, M. Lees, K. Kalatzi, I. Raptis, K. Misiakos, and S. E. Kakabakos, "Ultrafast Multiplexed-Allergen Detection through Advanced Fluidic Design and Monolithic Interferometric Silicon Chips," *Anal. Chem.* **90**, 9559–9567 (2018).
111. R. Bruck, E. Melnik, P. Muellner, R. Hainberger, and M. Lämmerhofer, "Integrated polymer-based Mach-Zehnder interferometer label-free streptavidin biosensor compatible with injection molding," *Biosensors and Bioelectronics* **26**, 3832–3837 (2011).
112. P. Azuelos, P. Girault, N. Lorrain, L. Poffo, M. Guendouz, M. Thual, J. Lemaître, P. Pirasteh, I. Hardy, and J. Charrier, "High sensitivity optical biosensor based on polymer materials and using the Vernier effect," *Opt. Express* **25**, 30799 (2017).
113. Z. Ding, H. Wang, T. Li, X. Ouyang, Y. Shi, and A. P. Zhang, "Fabrication of Polymer Optical Waveguides by Digital Ultraviolet Lithography," *J. Lightwave Technol.* **40**, 163–169 (2022).

114. Daoxin Dai, Bo Yang, Liu Yang, Zhen Sheng, and Sailing He, "Compact Microracetrack Resonator Devices Based on Small SU-8 Polymer Strip Waveguides," *IEEE Photon. Technol. Lett.* **21**, 254–256 (2009).
115. E. Melnik, R. Bruck, P. Müellner, T. Schleder, R. Hainberger, and M. Lämmerhofer, "Human IgG detection in serum on polymer based Mach-Zehnder interferometric biosensors," *J. Biophoton* **9**, 218–223 (2016).
116. M. Kitsara, K. Misiakos, I. Raptis, and E. Makarona, "Integrated optical frequency-resolved Mach-Zehnder interferometers for label-free affinity sensing," *Opt. Express* **18**, 8193 (2010).
117. Y.-L. Yeh, "Real-time measurement of glucose concentration and average refractive index using a laser interferometer," *Optics and Lasers in Engineering* **46**, 666–670 (2008).
118. J. Vörös, "The Density and Refractive Index of Adsorbing Protein Layers," *Biophysical Journal* **87**, 553–561 (2004).
119. P. Damborský, J. Švitel, and J. Katrlík, "Optical biosensors," *Essays in biochemistry* **60**, 91–100 (2016).
120. A. L. Washburn, L. C. Gunn, and R. C. Bailey, "Label-Free Quantitation of a Cancer Biomarker in Complex Media Using Silicon Photonic Microring Resonators," *Anal. Chem.* **81**, 9499–9506 (2009).
121. Linghua Wang, J. Ren, Xiuyou Han, T. Claes, Xigao Jian, P. Bienstman, R. Baets, Mingshan Zhao, and G. Morthier, "A Label-Free Optical Biosensor Built on a Low-Cost Polymer Platform," *IEEE Photonics J.* **4**, 920–930 (2012).
122. T. Chalyan, L. Pasquardini, D. Gandolfi, R. Guider, A. Samusenko, M. Zanetti, G. Pucker, C. Pederzoli, and L. Pavesi, "Aptamer- and Fab'- Functionalized Microring Resonators for Aflatoxin M1 Detection," *IEEE J. Select. Topics Quantum Electron.* **23**, 350–357 (2017).